LUND UNIVERSITY

On the Use of Laser-Induced Incandescence for Soot Diagnostics: From Theoretical Aspects to Applications in Engines

Bladh, Henrik

2007

Citation for published version (APA):
Bladh, H. (2007). *On the Use of Laser-Induced Incandescence for Soot Diagnostics: From Theoretical Aspects to Applications in Engines*. [Doctoral Thesis (compilation), Combustion Physics]. Avdelningen för Förbränningsfysik, Fysiska Institutionen, Lunds Tekniska Högskola.

Total number of authors:
1

On the Use of
Laser-Induced Incandescence
for Soot Diagnostics

From Theoretical Aspects
to Applications in Engines

Doctoral Dissertation

Henrik Bladh

Division of Combustion Physics
Department of Physics

LUND UNIVERSITY

Henrik Bladh
Division of Combustion Physics
P.O. Box 118
SE-221 00 Lund, Sweden

To Ulrica

Abstract

The laser-induced incandescence technique (LII) is a laser-based diagnostic technique for measurements of soot volume fraction and particle size. The technique relies on detection of incandescent light from soot particles heated to around 4000 K using nanosecond laser pulses.

A theoretical model for LII has been implemented and improved in order to provide a tool for predicting the signal response from soot particles when exposed to the laser pulse for various experimental conditions. Specifically, the model is capable of predicting the signal response from arbitrarily shaped measurement volumes defined by non-uniform spatial distribution of laser energy, and also from primary particle size distributions. The model has been applied in order to investigate the influence of various physical and experimental parameters on evaluated primary particle size, the uncertainties introduced when measuring quantitative soot volume fractions in high-pressure environments using atmospheric calibration flames and on the relationship between the LII signal and the soot volume fraction. The model has also been applied in order to predict the appearance of experimentally obtained spatially resolved LII signals in a methane diffusion flame. The spatial distribution of laser energy, which has a profound influence on the LII signal behaviour, was measured using a beam profile CCD camera, the data being input to the model. A generally good agreement between theoretical and experimental data was found, but the results indicated that the theoretical model overpredicted the signal response at high fluence.

Two experimental investigations using laser diagnostics for in-cylinder measurements of internal combustion engines have been undertaken. In one of the studies the laser-induced fluorescence (LIF) technique was applied to measure the flame propagation inside a spark-ignition engine by detection of fluorescence from intermediate species in the end gas. Two Nd:YAG lasers operating at 355 nm and two ICCD detectors were used in order to provide two independent images of the unburnt gas region within single engine cycles. An image evaluation scheme was developed in order to evaluate the velocity field of the flame propagating inside the engine. In a second study the laser-induced incandescence technique was applied to measure quantitative soot volume fractions inside a high-speed direct-injection passenger car Diesel engine. The quantitative information was attained by relating the signals obtained in the engine to those obtained in a calibration flame.

List of papers

I.   Bladh, H. and Bengtsson, P.-E., *Characteristics of laser-induced incandescence from soot in studies of a time-dependent heat- and mass-transfer model.* Applied Physics B, **78**:241-248, 2004

II.   Bladh, H., Bengtsson, P.-E., Delhay, J., Bouvier, Y., Therssen, E., and Desgroux, P., *Experimental and theoretical comparison of spatially resolved laser-induced incandescence (LII) signals of soot in backward and right-angle configuration.* Applied Physics B, **83**:423-433, 2006

III.   Bladh, H., Hildingsson, L., Gross, V., Hultqvist, A., and Bengtsson, P.-E., *Quantitative soot measurements in an HSDI Diesel engine.* in *Proceedings of the 13th International Symposium on Applications of Laser Techniques to Fluid Mechanics*, Lisbon, Portugal, 26-29 June, 2006

IV.   Bladh, H., Johnsson, J. and Bengtsson, P.-E., *On the dependence of the laser-induced incandescence (LII) signal on soot volume fraction for variations in particle size*, Submitted to Applied Physics B

V.   Bladh, H., Brackmann, C., Dahlander, P., Denbratt, I., and Bengtsson, P.-E., *Flame propagation visualization in a spark-ignition engine using laser-induced fluorescence of cool-flame species.* Measurement Science & Technology, **16**:1083-1091, 2005

Related work

A. Walewski, J., Rupinski, M., Bladh, H., Li, Z.S., Bengtsson, P.-E., and Aldén, M., *Soot visualisation by use of laser-induced soot vapourisation in combination with polarisation spectroscopy.* Applied Physics B, 77:447-454, 2003

B. Brackmann, C., Nygren, J., Bai, X., Li, Z.S., Bladh, H., Axelsson, B., Denbratt, I., Koopmans, L., Bengtsson, P.-E., and Aldén, M., *Laser-induced fluorescence of formaldehyde in combustion using third harmonic Nd:YAG laser excitation.* Spectrochimica Acta Part A, **59**:3347-3356, 2003

C. Bladh, H., Delhay, J., Bouvier, Y., Therssen, E., Bengtsson, P.-E., and Desgroux, P., *Experimental and theoretical comparison of spatially resolved laser-induced incandescence signals in a sooting flame.* in *Proceedings of the European Combustion Meeting*, Louvain la Neuve, Belgium, 2005

D. Michelsen, H.A., Liu, F., Kock, B.F., Bladh, H., Boiarciuc, A., Charwath, M., Dreier, T., Hadef, R., Hofmann, M., Reimann, J., Will, S., Bengtsson, P.-E., Bockhorn, H., Foucher, F., Geigle, K.-P., Mounaïm-Rousselle, C., Schulz, C., Stirn, R., Tribalet, B., and Suntz, R., *Modeling Laser-Induced Incandescence of Soot: A summary and comparison of LII models.* Accepted for publication in Applied Physics B

Contents

Chapter 1

Introduction

Combustion as a phenomenon has been around long before planet Earth was inhabited by mankind. People both feared and were attracted to the beauty and strength of fire and indeed Aristotle included fire as one of the four elements from which all other substances were believed to originate. Though his description of the world is no longer in use, it still highlights the importance of fire and combustion for human kind. Since the dawn of the industrial era in the middle of the 19th century, combustion of fossil fuels has been, and still is, our main energy source. This is depicted in Fig. 1.1 in which the total primary energy supply of the world is shown as function of fuel type for the last three decades [1]. Ongoing research on new energy sources has not yet been able to present a cheap enough alternative to fossil fuels and they are generally believed to be dominating also during the upcoming three decades [2].
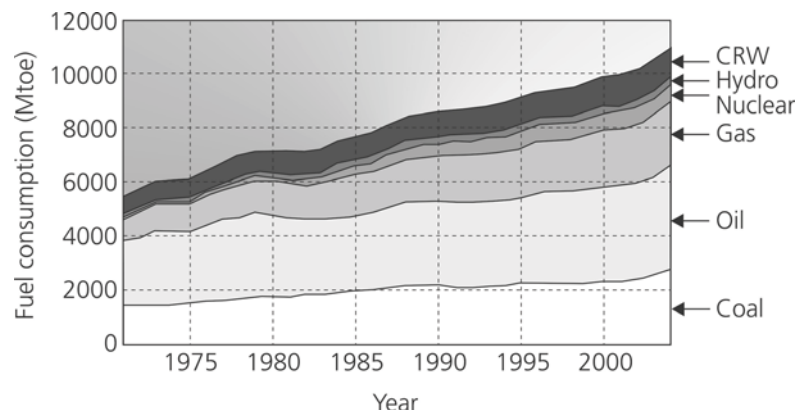
Figure 1.1 *The total primary energy supply in the world shown as function of fuel based on the statistics given by the International Energy Agency, IEA [1]. The data exclude international marine bunkers and electricity trade. CRW denotes combustible renewables and waste. Other energy sources (geothermal, solar, wind, heat etc.) constitute only fractions of a per cent and have not been included in the figure. Mtoe = megatonne of oil equivalent (equal to ~4.2 × 10^{16} J).*

1

The extensive use of combustion of fossil fuels has created many environmental problems. Its impact on the world climate has been discussed and investigated for many years, and lately the issue gained a lot of attention among the general public not least by the documentary 'An inconvenient truth' from the year 2006, featuring former vice president Al Gore [3]. Recently the Intergovernmental Panel on Climate Change (IPCC) issued the summary for policymakers [4] preceding the complete Fourth Assessment Report currently undergoing finalization. The potential impact of a certain factor on climate change is measured as its contribution to radiative forcing, defined as the change in the balance between radiation coming into the atmosphere and radiation going out. Positive forcing tends to warm the Earth's surface while negative forcing tends to cool it. Carbon dioxide, which is one of the end products from combustion of fossil fuels, is regarded as the major contributor to positive radiative forcing (the greenhouse effect). According to the Fourth Assessment Report from IPCC [4] the CO_2 concentration in the atmosphere has increased from 280 ppm before the start of the industrial era to 379 ppm in 2005, an increase with 35%. Carbon dioxide is not the only greenhouse gas. Other species with positive forcing are methane and nitrous oxide. Both gases are to some extent naturally formed but are also produced by anthropogenic activities like combustion and agriculture [4,5]. According to the Fourth assessment report from IPCC most of the observed increase in globally averaged temperatures since the mid-20th century is *very likely* due to the observed increase in anthropogenic greenhouse gas concentrations. A reduction of the use of fossil fuels as our major energy source seems to be the only reasonable solution to this problem, and in the meantime, combustion systems within the transport and energy sectors must be constantly improved for fuel efficiency.

There are also substances believed to contribute to negative forcing. These include aerosols, of which soot particles from combustion is one of the constituents. The impact of soot on the climate is believed to be due to several effects, as discussed by Highwood and Kinnersley [6]. A direct effect will occur due to the absorption and scattering characteristics of the particles in the atmosphere effectively reducing the solar radiation at the Earth's surface. An indirect effect may occur as particles become mixed with condensing matter potentially affecting cloud microphysics. A semi-direct effect that is believed to occur involves heating of the atmosphere in regions with high levels of soot particles, potentially affecting the cloud formation. The indirect surface albedo effect may also contribute to ice melting as soot particles deposited on ice and snow exert a heating effect. The net influence of these different potential effects on the climate is relatively uncertain, and results from research do not show agreement to the same extent as for carbon dioxide [6], something acknowledged also by IPCC [4].

In addition to the climate effects, pollutants originating from combustion are damaging for plants, animals and humans, and pose a threat to our cultural heritage, evident for instance in many of the cities of Europe. Major pollutants from combustion processes are NO and NO_2, often grouped together as NO_x, and

CO and polycyclic hydrocarbons, PAH, which will be further discussed in Chapter 2. These compounds may, when irradiated by sunlight, give rise to photochemical smog, leading to eye and respiratory problems for humans, reduced visibility and damage to plant life [5]. Coal combustion has traditionally been the main contributor to sulphur dioxide, SO_2, emissions, leading to acid rain destroying forests and lakes and effectively causing erosion of buildings, especially those made of carbonate stone [5].

As will be discussed in Chapter 2, soot particles are produced in incomplete combustion processes, where the excess fuel can not be fully transformed into carbon dioxide and water. An extensive review on the toxicology of soot and the molecular species condensed at the soot surface is given by Barfknecht [7] and a recent review of the health effects of atmospheric black carbon is given by Highwood and Kinnersley [6]. Soot particles occur in size ranges between a few nanometres up to several microns, and especially newly formed 'young' soot has a reactive surface on which often PAH molecules are condensed. These molecular species have been found to be both carcinogenic and mutagenic to mammalian cells. The most dangerous particles are the ones small enough to be readily transported through the human respiratory system into the lungs where they can be deposited. Lung diseases like chronic bronchitis and cancer of the lung lining have been found excessive among workers in mines and within the carbon black industry in the past [6]. The smallest particles may also move away from the primary deposit region by penetrating the lung lining entering the blood, eventually accumulated in other organs like the liver. Soot particles are also believed to have a direct effect on the autonomic nervous system, increasing the risk of premature death via fatal dysrhythmias.

In view of these adverse effects of the large-scale use of combustion, fossil-fuel combustion in particular, research within the area of combustion is necessary in order to achieve higher fuel efficiency of combustion devices like engines and gas turbines, less pollutant formation during these processes, and finally improved exhaust aftertreatment. The gradual transition from the use of fossil fuels towards biofuels also requires fundamental knowledge on the principles of combustion. Ultimately, combustion studies will be of importance also in a possible future world where combustion no longer dominates the world energy supply. Natural fires and fires within buildings are likely to be as common as today, and the principles of combustion and the characterisation of emissions like for instance soot particulates will be highly important.

The reasons mentioned above highly motivate development of diagnostic tools in order to measure various properties of combustion processes. The measured properties may be used as input to various combustion models for validation purposes, and they may also provide direct input for manufacturers of combustion devices in order to improve the design leading to increased fuel efficiency and decreased emission levels. Measurements in combustion require techniques capable of providing spatially and temporally resolved data on concentration, temperature,

and flow characteristics and, for soot particles, size distributions and data on morphology. Laser-induced incandescence (LII) has been recognised as one of the most promising techniques for *in situ* quantitative measurements of soot volume fraction and particle size. The technique is relatively straightforward to implement and has been used extensively during the last two decades, this being the possible reason why some may regard the technique as already fully developed. The fundamental mechanisms governing the signal generation are, however, complex and for this reason both theoretical and experimental studies are needed to improve the accuracy of the technique.

The main aim of this thesis has been to improve the theoretical model for the laser-induced incandescence (LII) technique for measurements on soot in combustion environments and apply the technique for measurements in various systems. Theoretical results have been compared to measurements in a laboratory flame, and the technique has been applied for in-cylinder engine measurements in a Diesel engine. In addition to this, in-cylinder measurements in a spark-ignition engine using the laser-induced fluorescence (LIF) technique have been carried out.

The outline of the thesis will be as follows. Some fundamentals of combustion processes and the formation of soot particles will be given in Chapter 2 and in Chapter 3 an overview of diagnostic techniques for combustion studies with focus on the LII technique will be given. Chapter 4 provides the reader with a short description of the experimental equipment used, and measurement objects investigated within the work presented in the thesis. The details of the theoretical model for LII extended for real measurement systems will be described in Chapter 5 followed by a review of some of the results presented in the papers (Chapter 6). A summary and outlook (Chapter 7) ends the thesis.

Chapter 2

Combustion and soot formation

In this chapter some fundamentals of combustion will be given. Special focus will be on soot, and how it is formed. The treatment follows what is outlined by Glassman [8], Griffiths and Barnard [5] and Heywood [9].

The combustion phenomenon has its origin in chemistry, with a self-supported exothermic reaction, i.e. a reaction which transforms a number of molecular species (reactants) with relatively high level of chemically bound energy into a number of product species with lower energy and where the excess energy leaves as heat. For the process to be self-supported, a number of criteria have to be fulfilled. Molecular diffusion and the bulk gas flow characteristics affect the rate at which the chemical species can travel to and from the reaction zone. The heat conduction properties of the gas mixture affect the efficiency of energy transport from the reaction zone to the surroundings. These physical conditions affect the overall combustion process. On the other hand, the characteristics of the physical processes are governed by the temperature and concentration gradients near the reaction zone set up by the exothermic reaction itself. This two-way interaction between the chemical reactions and the physical transport processes makes it necessary to take all processes into account to fully describe the combustion process.

The reactants can be divided into two categories: The fuel and the oxidizer (often air). The fuel contains the energy chemically bound within its structure, and the oxidizer can free this energy by oxidation, which essentially involves removal of electrons from the oxidized species, the fuel [10]. The details regarding the transformation of reactants into product species are complex. Even for the relative simple mechanisms like methane-oxygen oxidation, there are hundreds of elementary reactions describing different pathways for the transformation from reactants to products [8]. The transformation proceeds via a large number of intermediate species, often radicals, which are consumed later on in the process. One such intermediate is the formaldehyde molecule, H_2CO, which was used to visualise the flame front inside the combustion chamber of an SI engine in the work presented in paper V. The overall combustion process can be described using a global representation of the chemistry, in which only the reactants and products

are considered. The global reaction for the ethylene-oxygen mechanism can be written as

$$C_2H_4 + 3O_2 \rightarrow 2H_2O + 2CO_2 \,. \tag{2.1}$$

These global reactions define the conditions for complete combustion, i.e. combustion where all fuel and oxidizer are consumed and transformed into the products water, H_2O, and for hydrocarbon fuels also carbon dioxide, CO_2. These conditions are referred to as stochiometric.

One usually categorizes combustion in two major groups: Premixed flames and diffusion flames. The difference between the two types has to do with the transport process of the reactants to the reaction zone. In premixed combustion the fuel and oxidizer are mixed prior to combustion and the reaction zone will propagate with respect to the gas mixture. In a stationary premixed flame the gas flow out of the burner nozzle counteracts the burning velocity of the reaction zone thus essentially producing a flame standing still. In a spark-ignition engine, like the one investigated in the work presented in Paper V, the flame burning velocity is responsible for the flame front propagating towards the cylinder walls, but also here the bulk gas flow affects the flame front propagation.

Premixed combustion may occur within a quite large range of mixtures including, of course, the stochiometric conditions. To characterise the mixture composition, the equivalence ratio is used. This quantity is defined as

$$\phi = \frac{\left(n_\text{fuel}/n_\text{oxidizer}\right)_\text{gas mixture}}{\left(n_\text{fuel}/n_\text{oxidizer}\right)_\text{stochiometric}} \,. \tag{2.2}$$

where the ratio within brackets denotes the number of moles between the fuel and oxidizer in a mixture. For $\phi > 1$ there is excess of fuel and the combustion is referred to as rich. For $\phi < 1$ there is excess of oxidizer and the combustion is called lean. In the internal combustion engine literature one often uses the relative air-fuel ratio λ, which is the inverse of the equivalence ratio. Another quantity often used when discussing soot formation is the C/O ratio. This quantity is defined as the ratio between the number of carbon atoms to oxygen atoms in a mixture. In the ethylene-oxygen example given in Eq. 2.1 the C/O ratio will be 1/3. In a diffusion flame the fuel and oxidizer are kept separate and forms the reaction zone at their interface. The combustion process becomes highly dependent on the mixing phenomena, i.e. the diffusion of fuel towards oxidizer and vice versa. In these kinds of flames fuel-rich and fuel-lean regions may exist quite close to each other. Typical examples of diffusion flames are a candle flame and most often the combustion process inside a Diesel engine (See section 4.4.2).

In rich combustion of hydrocarbon fuels, there will be an excess of carbon atoms which leads to incomplete combustion, i.e. formation of other carbon-containing products than carbon dioxide. At moderately increased equivalence ratios, the carbon will not only end up as carbon dioxide, but also as carbon

monoxide, CO. At even higher equivalence ratios soot particles will form. A simplified treatment of the process would give that soot formation should occur for C/O>1, but in real systems it is usually less (0.5 – 0.8) [9]. Soot is larger fragments of primarily carbon but also hydrogen (~1% by weight). These fragments are formed from gas-phase combustion processes predominately in fuel-rich high-temperature regions. Soot is generally believed to have its origin in larger polycyclic aromatic hydrocarbon (PAH) molecules. These are present in fuel-rich sooting hydrocarbon flames and are often referred to as soot *precursors*. The soot formation process is schematically visualised in Fig. 2.1. Unburnt fuel in high-temperature regions is pyrolysed into smaller molecules, among them acetylene, which is regarded as one of the earliest precursors to soot. Different mechanisms have been suggested that may explain the formation of the first aromatic ring structure (benzene), and from these larger PAH molecules such as for instance naphthalene and pyrene. The transition from molecular species to solid particulates is believed to occur as the two-dimensional PAH molecules add to each other building three-dimensional structures. This process is referred to as the nucleation process. Some experimental data suggest these first particles to be around 2 nm [11].
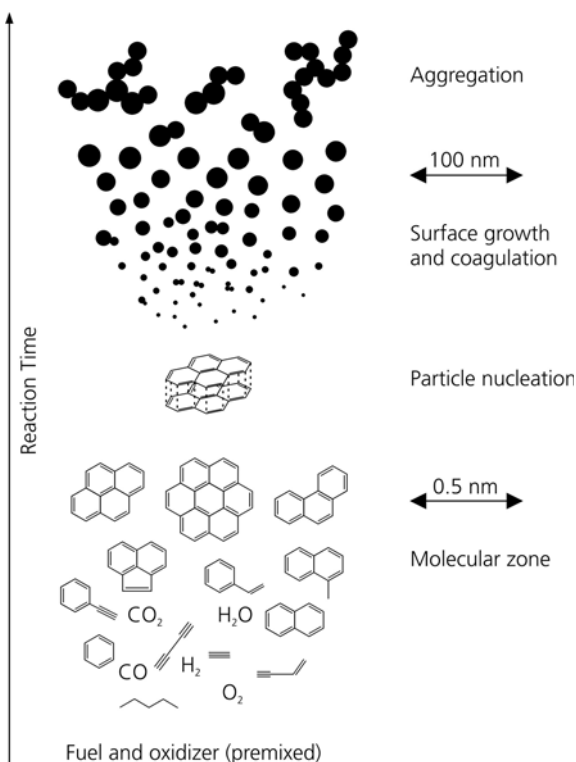

Figure 2.1 A schematic representation of the soot formation process inspired from [12].

X-ray diffraction investigations on soot particles have showed a large number of crystallites within the structure, each consisting of 5-10 sheets of carbon atoms, where every sheet consists of about 100 atoms [11]. Typical for the young soot particles, apart from their small size, is that they contain large fractions of hydrogen. In the high-temperature combustion regions of a flame, the hydrogen fraction of the particles decreases as the particles age. After being formed, the particle nuclei are constantly exposed to different gaseous hydrocarbon species like acetylene, which reacts with the soot particle surface to form larger structures. This mechanism is referred to as *surface growth*. Another growth mechanism is *coagulation* which means that two or more small soot nuclei collide and stick together thus forming one larger particle. Both these mechanisms occur parallel to each other but affect the soot formation process in quite different ways. Coagulation effectively reduces particle number density without affecting the volume fraction, whereas the surface growth does the opposite. Coagulation results in highly non-spherical particles whereas surface growth has the opposite effect and effectively reduces irregularities resulting in nearly spherical particles at the end of the process. As surface growth ceases in the later part of the formation process, the particles will add to each other in different ways in a process called *aggregation* forming larger structures of sizes of several hundreds of nanometres. The near-spherical particles within the aggregate are referred to as primary particles and they have generally sizes in the range 5-50 nm.

Oxidation by gaseous species like O_2 and OH surrounding the soot particles constantly compete with the soot formation process. In some combustion processes soot is never emitted at all in spite of the fact that levels were quite high in some regions. One example is the candle flame where essentially all soot is oxidized leaving no particles emitted to the surroundings. Diesel combustion is another example where oxidation plays a fundamental role. In such engines a liquid fuel spray is injected into the combustion chamber at high pressure. The spray droplets are gradually vaporised, and combustion starts in regions where gaseous fuel and air are partially premixed. However, in some regions diffusion flame like combustion will occur due to insufficient mixing and vaporisation resulting in high levels of soot. However, due to the large amount of air in the combustion chamber, most of the soot is oxidized before leaving the engine. Finally, the process of condensation and adsorption of hydrocarbons on the soot surface can be mentioned. This process occurs at lower temperatures and is typical for Diesel soot diluted with air in the engine exhausts [9].

Soot can be characterised using different quantities, the most common being the soot volume fraction, f_v, the primary particle size, D, and the particle number density N. If the primary particles are assumed spherical the soot volume fraction may be written as

$$f_v = N \frac{\pi D^3}{6} \, .$$

(2.3)

8

Typical flame soot aggregates are shown if Fig. 2.2, which shows transmission electron microscopy images of soot collected using thermophoretic sampling, techniques that will be further discussed in chapter 3.2.
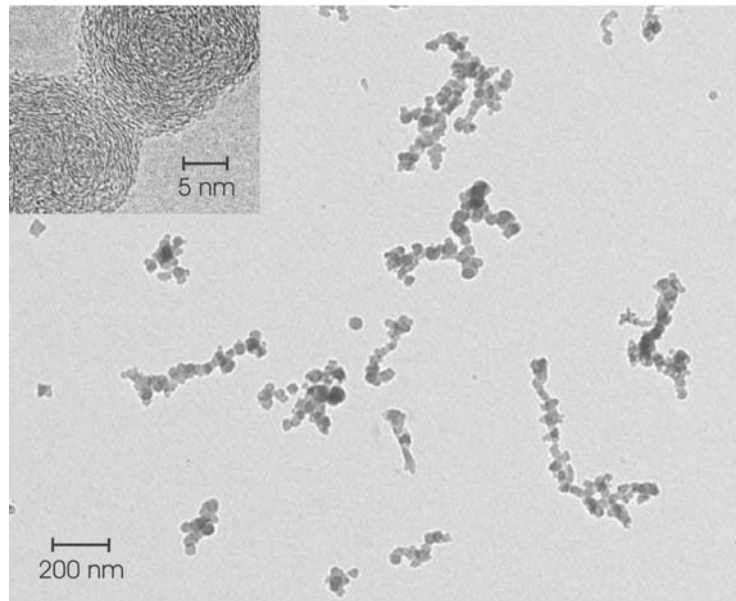
Figure 2.2 *Transmission electron microscopy (TEM) images of flame soot. The main picture shows soot aggregates sampled at the centreline and at 42 mm above the burner nozzle in a laminar ethylene-air diffusion flame (Tian et al. [13]), whereas the inserted image shows high-resolution TEM images (HREM) of soot particles sampled at the centreline and at 210 mm above the burner nozzle in a laminar ethylene flame with forced co-annular air flow (Shaddix et al. [14]).*

Chapter 3

Diagnostic techniques

Combustion is probably one of the oldest phenomena on earth and was here long before human beings started to master its energy. The mystic and suggestive feeling of a camp fire or even a candle has probably aroused a lot of curiosity among the inhabitants during the years. With the start of the industrial era the incitement for gaining knowledge on the phenomenon grew as people realised its importance as an energy source not least for the transportation sector. With this in mind it might not be too surprising to find that diagnostic techniques for combustion studies have been developed and used for many hundreds of years. In this chapter some fundamental aspects of diagnostics for combustion studies will be given, with special focus on measurements on soot.

3.1   Comparison of diagnostic tools

Diagnostic techniques for combustion studies involve both probe techniques and optical techniques, of which laser diagnostics is one. Probe techniques involve for instance thermocouples for temperature measurements and sample probes for major species concentration measurements [15]. The drawback of these techniques is that they tend to disturb the processes they are intended to investigate: they are intrusive. They are also generally limited in their spatial resolution and temporal response [16].

Optical diagnostics offer a non-intrusive alternative to the probe techniques. Optical techniques involving absorption and natural emission of radiation were applied for measurements in flames already during early years (See [17] and references therein), building a large knowledge base not only with respect to combustion processes. Spectroscopic flame studies of natural emission played an important part in the early days of development of atomic and molecular spectroscopy. For instance the strong bands of emission (these are especially prominent in the blue-green region) typically observed in Bunsen flames were investigated already in 1857 by the Scottish physicist William Swan. However, it was to take more than 70 years of development in the area of molecular

spectroscopy and numerous detailed experimental investigations before this emission could be proved to originate from the C_2 radical [17].

Natural emission and absorption measurements are, though non-intrusive, limited in several aspects. They are line-of-sight measurements, i.e. the collected signal has no spatial resolution along the signal propagation direction. Another drawback is that many species of interest in combustion are hard or impossible to detect using these techniques since they do not emit light in large enough quantities to be detected. With the invention of the laser in the 60's many of these limitations could be overcome leading to the start of a new era within combustion diagnostics. With lasers it is possible to induce signals from species in the flame in ways not possible using conventional light sources. The coherent light from a laser can be focused into small regions ensuring high spatial resolution. Pulsed lasers with typical pulse durations of tens of nanoseconds are fast enough to probe flame properties also for turbulent flames by essentially "freezing the flow", i.e. detect the signal during time gates much shorter than the fastest velocities in the flow. Lasers are narrowband light sources meaning that they essentially emit radiation at a specific wavelength. This makes it possible to choose wavelength in order to probe certain species only responding to that particular wavelength; laser measurements can be species specific. Another advantage of the laser compared to traditional light sources is the high peak power density in the beam. This opens up possibilities of utilizing non-linear effects in interaction between laser radiation and molecules, effectively increasing the capability of optical diagnostics [16].

There are, however, also a number of disadvantages with using optical techniques and laser techniques for combustion studies. One of the most crucial is the requirement of optical access to the process studied. Especially for internal combustion engines and other high-pressure devices, optical access requires substantial reconstruction that can not be made without altering the fundamental characteristics of the device to some degree. This is further discussed in Chapter 4.4.3. There are also a number of drawbacks specifically with respect to laser diagnostics. It is not possible to detect all molecular species at once, and for multi-species measurements, usually complex combinations of techniques using multiple lasers and detection systems are needed. The ability of the techniques to be species-specific is reduced for larger molecules due to their spectroscopic features being less distinct. It is also extremely difficult to attain the high resolution in three dimensions required for accurate measurements of micro-scale flow characteristics in turbulent combustion. Lasers are also quite expensive and complex equipment requiring skilled operators.

3.2   Soot diagnostics

Measurements on soot in combustion processes involve both optical and probe techniques. In this chapter the most important of these will be summarized with

special focus on the laser-induced incandescence technique used in the work presented in this thesis.

3.2.1 Probe techniques

Soot and aerosol particles are often characterised and quantified using probe techniques and here a few of these will be briefly discussed. A thorough review of these and many other techniques is given by McMurry [18]. One of the most common techniques for particle mass measurements is *gravimetric sampling*, which involves sampling of particles on a filter through which a measured volume of gas is drawn. The filter is weighed before and after sampling under controlled temperature and relative humidity conditions, and the mass fraction can be calculated by the increase in filter mass and the volume of gas drawn through the filter. The sampling procedure and weighing is time-consuming and no online measurement data can be achieved. Several comparisons between gravimetric sampling and optical diagnostics on soot have been presented [19-22].

Particle number concentration can be measured using so called *condensation particle counters (CPC)*. The particles are directed through a region supersaturated with a vapour, most often water or an alcohol. The vapour condenses on the particles and increases their size. The particles are then directed into another part of the instrument in which the number concentration is measured either by using direct measurements of individual droplets (low concentrations only) or indirect measurements by using optical methods such as absorption or scattering. Condensation particle counters may detect particle sizes as low as 3 nm [18].

Another commonly applied probe technique is the *differential mobility particle sizer (DMPS)*, which is used to select and quantify particles of a certain size. The apparatus consists of two parts, one that selects particles of a certain size, and one that detects them. The size selection is made using a *differential mobility analyzer (DMA)*, which separates the particles according to their mobility in an externally applied electric field. The particles are sampled from the measurement volume using a sample probe and are then electrically charged using a radioactive source. In this way the particles acquire a charge q with a well-defined probability. The probability of particles acquiring multiple charges increases with particle size, which must be compensated for. The gas containing the charged particles is then directed into a cylinder of specified length. Concentrically positioned within this cylinder is a rod, and an electrical field is applied between the rod and the cylinder wall. The charged particles will get attracted to the rod and deviate from its path. At the end of the rod a slit is positioned through which only the particles with a certain mobility diameter will be allowed to pass. The selected particles are then transported to a second device for quantification. Such a device could for instance be a condensation particle counter. The externally applied field between the rod and the cylinder determines which particle sizes are allowed to pass through the slit. By scanning the field strength over some measurement interval, the particle

size distribution may be obtained. This instrument is referred to as a *scanning mobility particle spectrometer (SMPS)* and typical measurement times mapping the mobility size distribution are around 2 minutes. Particle sizes obtained with this technique can be compared with sizes inferred from laser-induced incandescence measurements. However, it is important to keep in mind the difference between the mobility diameter as measured by SMPS and the primary particle size obtained from the LII technique, especially in regions with large numbers of aggregated particles. This has been discussed by Smallwood et al. [23] who compared LII and SMPS data obtained from Diesel exhausts, and more recently by Krüger et al. [24] using the same techniques in a premixed laminar sooting flame.

The last technique discussed here is *transmission electron microscopy (TEM)* of sampled particles. This technique has been widely used to characterise particle size distributions and morphology (See for instance [13,25-27]). The particles are sampled using a technique called *thermophoretic sampling*, which involves inserting a fine grid in the region of interest during a short time. Typical sampling times are tens of milliseconds [13,27]. As the name implies, the soot particles are exposed to a positive force with respect to the grid due to a process called thermophoresis, i.e. the positive force exerted on the particles by the temperature gradient set up between the room-temperature grid and the hot flame [28]. The grid with the sampled soot is imaged using a transmission electron microscope and advanced image evaluation software utilizing contour recognition algorithms may be used to collect statistics on particle size distributions and morphology. Since TEM measurements may be used to evaluate the primary particle size distribution, it has become a very popular technique for validating size distributions measured with the laser-induced incandescence technique [29-31].

3.2.2 Optical techniques

Optical diagnostics on soot have been discussed for instance in [32-34] and for engine diagnostics in [35]. Soot particles are strong absorbers and emitters of electromagnetic radiation. This can be seen in sooting combustion processes as emission of strong radiation both in the visible, giving such processes its characteristic yellow colour, and in the infrared region making soot an efficient heat transfer agent. Apart from these processes the particles scatter photons. The theory of absorption and scattering of light by particles is given in [36,37] and here only a brief summary will be given. Soot particles are often assumed to be spherical and isotropic and for such particles the Mie theory applies. This theory is relatively complex and substantial simplification is achieved by assuming that the particle size is much smaller than the wavelength of the incoming light, usually referred to as the Rayleigh limit assumption. Explicitly the Rayleigh theory applies for [37,38]

$$\frac{\pi D |m|}{\lambda} << 1.$$

(3.1)

in which λ represents the wavelength, D is the particle diameter and m the complex refractive index of the particle. For aggregated particles the so called Rayleigh-Debye-Gans (RDG) theory is often used. The principle of the RDG approximation is to divide a particle of arbitrary shape in small enough subunits, each within the Rayleigh limit, in order to create a system in which the phase differences between the scattering from various subunits are small. Additionally, multiple scattering and self-interaction between the subunits are assumed negligible [39]. The RDG theory may be combined with a theory for aggregate formation based on fractal geometry. Such theories have been used and tested quite extensively (See for instance [39-41]) and is further discussed in Chapter 5.2.1.2.

The refractive index m determines the optical properties of the particle and is therefore a crucial parameter when discussing interaction with electromagnetic radiation. Unfortunately, this quantity is believed to vary with chemical composition, temperature and wavelength, and especially the first factor introduces large uncertainties since it is difficult to know the chemical composition of the soot in a certain system. It may depend on the type of fuel and oxidizer, the equivalence ratio, the pressure and so on. Literature data on the refractive index of soot also suffer from limitations in the experimental approaches used to measure this value. This has been discussed for instance by Krishnan et al. [42]. The refractive index affects the interaction processes via the refractive index functions [32]

$$E(m) = -\mathrm{Im}\left(\frac{m^2-1}{m^2+2}\right), \quad F(m) = \left|\frac{m^2-1}{m^2+2}\right|^2, \tag{3.2}$$

where $E(m)$, often referred to as the absorption function, turns up in the expressions for absorption and emission, whereas $F(m)$ enters in the expression for scattering. Figure 3.1 shows a comparison made by Krishnan et al. [42] showing
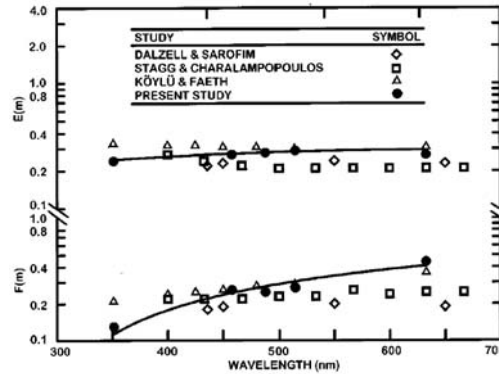

Figure 3.1 *Comparison of the value of E(m) and F(m) as function of wavelength by Krishnan et al. [42] (marked as "present study"). The other studies are Dalzell and Sarofim [43], Stagg and Charalampopoulos [44] and Köylü and Faeth [45].*

values for the two functions evaluated using their own measurements of the refractive index and some other measurements from literature.

Keeping these fundamental issues in mind, a number of optical techniques for soot diagnostics will be discussed. Focus will be on the laser-induced incandescence technique which has been used in much of the work presented in this thesis. *Natural flame emission* studies can be used to give estimates of the amounts of soot in combustion systems. The emission from hot soot particles can be described by the Planck radiation law weighted by the emissivity of the soot particles. In the Rayleigh limit the emitted intensity can be written as

$$I(T,\lambda) \propto \frac{4\pi D E(m)}{\lambda} \frac{2\pi h c^2}{\lambda^5 (e^{hc/\lambda k_B T} - 1)} .$$ (3.3)

Here λ represents the detection wavelength and D the primary particle diameter. The strong temperature dependence of the emission introduces large uncertainties when estimating the amounts of soot from emission measurements. The flame temperature may, however, be estimated by detecting the soot emission at two or multiple wavelengths, a technique referred to as *pyrometry*. Comparison of measurement data with Eq. 3.3 essentially yields the average soot particle temperature. The technique was first presented by Hottel and Broughton in 1932 [46] and is relatively straightforward to implement. It has been applied quite extensively for measurements of the average flame temperature in different systems [47-50]. A drawback of these techniques is that they rely on detection of the natural emission making them line-of-sight techniques. The techniques also suffer from uncertainties in the refractive index of soot. A novel improvement of the pyrometry technique circumventing this problem has been presented by Jenkins and Hanson [51].

A quite successful approach for soot measurements has turned out to be combined *extinction* and *scattering*. Combining the two techniques makes it possible to extract both soot volume fraction and particle size [32,52,53]. The typical experimental setup consists of a pulsed or continuous wave (CW) laser which is directed into the measurement region. Soot particles in the flame will both absorb and scatter laser photons. By detecting both the incoming and transmitted laser intensity the total extinction may be calculated. The scattering is usually detected at 90-degree angle with a separate detector. By applying theoretical expressions for the processes the volume fraction and size may be retrieved. In the case of isotropic spherical particles in the Rayleigh limit, the volumetric scattering cross section is given as [32,37,54]

$$Q_{vv} = \frac{\pi^4}{4\lambda^4} \left| \frac{m^2 - 1}{m^2 + 2} \right|^2 ND^6 = \frac{\pi^4 F(m)}{4\lambda^4} ND^6 ,$$ (3.4)

whereas the absorption coefficient is given as

16

$$K_{abs} = -\frac{\pi^2}{\lambda}\,\mathrm{Im}\!\left(\frac{m^2-1}{m^2+2}\right)ND^3 = \frac{\pi^2 E(m)}{\lambda}ND^3 ,\qquad (3.5)$$

in which N denotes the particle number density and D the particle diameter. The extinction coefficient may be experimentally obtained using the expression

$$K_{ext} = \frac{1}{L}\ln\!\left(\frac{I_0}{I_T}\right),\qquad (3.6)$$

where L is the absorption path length in the soot, I_0 and I_T the incident and transmitted radiation intensity respectively. For particles in the Rayleigh limit the scattering is negligible compared to the total extinction which means that $K_{ext} \approx K_{abs}$. This relation combined with (3.5) and (3.6) and the expression for soot volume fraction given in Eq. 2.3 yields

$$f_v \approx \frac{\lambda}{6\pi E(m)}K_{ext} = \frac{\lambda}{6\pi L E(m)}\ln\!\left(\frac{I_0}{I_T}\right).\qquad (3.7)$$

Combining (3.4) with (3.6) and the fact that $K_{ext} \approx K_{abs}$ gives

$$D \approx \lambda\left(\frac{4}{\pi^2}\frac{E(m)}{F(m)}\frac{Q_{vv}}{K_{ext}}\right)^{1/3}.\qquad (3.8)$$

The theory given here is quite simplified. It assumes monodisperse particle size distributions and non-aggregated particles. More extensive theoretical treatments have been presented taking these factors into account [32,55,56]. One important limitation of the technique is that it relies on knowledge of the refractive index of soot. Another limitation is that extinction measurements are line-of-sight meaning that no spatial information along the laser beam propagation direction is available. In circular-symmetric flames like diffusion flames inversion procedures can be used to calculate the soot volume fraction distribution also along the beam direction [32,57,58].

The relatively large uncertainties in the refractive index of soot affect all scattering measurements relying on the absolute radiation intensity, so called static light scattering. In an alternative scattering technique called *dynamic light scattering (DLS)*, the soot particle size may be retrieved by monitoring the temporal fluctuations in the scattered signal from the particles when exposed to a continuous wave laser. These fluctuations relates to the diffusional motion of the particles which depends on their size. A detailed review of this and other light scattering techniques for studies on soot is given by Charalampopoulos [59]. Recommended is also the work by Lamprecht et al. [60] who made extensive investigations of the DLS technique in a number of premixed flames.

During the 90's the *laser-induced incandescence (LII)* technique became popular within the combustion research community. The technique relies on detection of the increased emission (incandescence) from soot particles when heated by a pulsed laser. The first publication discussing this process has been attributed to Weeks and Duley in 1974 [61] who proposed to use heating of aerosol particles with a pulsed laser in order to estimate their size. Three years later Eckbreth [62] discussed the process due to its interference on the Raman scattering signals in sooting combustion environments. In 1984 Melton [63] proposed to use the signal obtained by laser heating as a diagnostic technique to measure soot volume fractions. A nice review of the laser induced incandescence technique is given in [33] and its current status has been described in [64].

The setup of the LII technique applied for imaging the soot volume fraction in a laboratory flame is shown in Fig. 3.2. The laser beam from a Nd:YAG laser at the fundamental wavelength of 1064 nm or its second harmonic at 532 nm is shaped into a laser sheet by a combination of lenses. A typical sheet width is around 200 microns. The soot particles in the measurement volume are rapidly heated by the ~10 ns laser pulses from flame temperatures up to ~4000 K resulting in substantial increase in emitted incandescence. For measurements of soot volume fractions, the prompt signal is detected, in this case by an ICCD camera with typical gate durations of tens of nanoseconds. Some characteristics of the experimental equipment are discussed in Chapter 4. The signal is spectrally filtered mainly to avoid interference from the soot not heated by the laser and to avoid molecular interference from C_2 and PAH, which may be excited when utilizing a wavelength of 532 nm or lower [57,64-66]. The choice of detection wavelength also has an
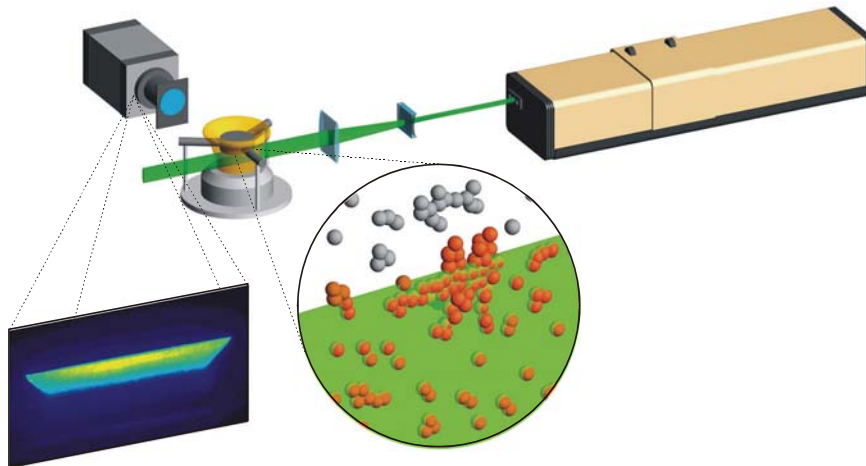

Figure 3.2 *A typical experimental setup of the laser-induced incandescence (LII) technique for imaging measurements of soot volume fraction in a flat flame burner.*

influence on the relationship between the LII signal and the soot volume fraction as discussed later in this chapter. Apart from flame studies, soot volume fraction measurements have been carried out for internal combustion engines both for in-cylinder measurements [35,67-73] and in the exhausts [20,23,74-80]. In Paper III quantitative in-cylinder measurements of soot volume fraction obtained in a Diesel engine are presented.

Soot volume fraction measurements using the LII technique rely on the approximate linearity that is believed to exist between the prompt LII signal and the volume fraction. The assumption of linearity is based upon both experimental and theoretical investigations. Experimental studies involve comparisons between LII and other techniques such as extinction [81-86]. Theoretical investigations are few, the most noteworthy being the original work by Melton [63]. Using a theoretical model for the heat-up process, he showed that the LII signal was dependent on the particle size via a power law according to

$$S_{\text{LII}} \propto ND^{3+0.154/\lambda_{\text{det}}} \,, \tag{3.9}$$

where the detection wavelength λ_{det} is given in microns. Obviously linearity between signal and soot volume fraction would require the exponent to be 3, but in reality the exponent has been found to be larger. In addition to Melton's work, some theoretical investigations were also carried out by Mewes et al. [87,88]. In Paper IV an extensive theoretical investigation of the signal dependence on soot volume fraction is presented.

Assuming a linear relationship, the LII technique provides relative soot volume fraction data. For quantitative measurements the technique has to be calibrated. Most often this has been carried out using measurements in calibration burners where the soot volume fractions has been determined using other techniques like for instance extinction [83,84,89]. This approach inevitably transfers uncertainties of the calibration technique to the quantitative data obtained using LII. As an example, if the calibration flame is characterised using extinction, the uncertainties in the refractive index affect also the LII data. Other uncertainties are introduced when comparing data obtained using LII in different systems with different ambient temperature and pressure. One example of this is presented in Paper III, which describes the work where the LII technique was applied inside the combustion chamber of a Diesel engine to obtain quantitative data on soot volume fraction via calibration using an atmospheric flame. The uncertainties were discussed and some of them estimated using the theoretical model for LII presented in Chapter 5. The sensitivity of extinction calibration is relatively low in systems with low volume fraction, and here the cavity-ring-down technique can be used to increase sensitivity [66,90,91]. Non-optical techniques like gravimetric sampling has also been investigated as a calibration source [19]. A novel calibration approach outlined by Snelling et al. [92,93] is to use a calibration lamp combined with detection of the LII signal at two different wavelengths.

One inherent feature of the LII signal, when measured using gated detection, is its nonlinear relationship with laser fluence, i.e. the pulse energy per cross section area of the beam. This behaviour was early recognized experimentally (See for instance [57,81,84,85,94-96]) and has to do with the different physical processes that occur during the heat-up of the particles and during their subsequent cooling phase. The details of these processes are given in Chapter 5 and only a brief description is given here. For a single soot particle at low laser fluences (approximately for $F < 0.1$ J/cm^2 for 532 nm excitation) the LII signal is strongly dependent on the laser fluence. As the particle temperature is raised to about 4000 K the sublimation temperature is reached, and the increase of particle temperature with increasing laser fluence is predicted to be small: instead of heating the particle, the excess energy is used to sublime matter effectively reducing the particle size and hence the LII signal. The net effect is predicted to give decreasing LII signal with increasing laser fluence. This behaviour holds for one single particle, but in real systems many particles coexist in the measurement volume, all contributing to the detected signal. If it is ensured that all particles in this volume are exposed to exactly the same laser fluence, i.e. the spatial profile of the laser energy is top-hat, the shape of the fluence curve is expected to be similar to the one discussed above for one particle. A schematic fluence curve for such a system is shown in Fig. 3.3a.
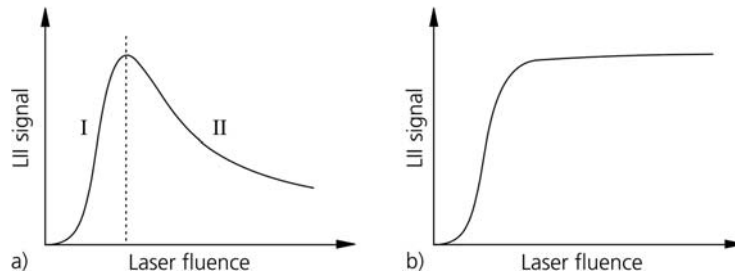
Figure 3.3 *Typical appearance of fluence curves when the LII signal is detected using a prompt gate for (a) a uniform spatial profile (top-hat profile) and (b) a non-uniform spatial profile.*

For spatially non-uniform laser profiles, different fluence regimes coexist within the measurement volume giving an averaging effect on the total signal response. For a specific choice of spatial profile, a sufficient number of soot particles are exposed to fluences in the high-fluence region with the negative fluence-dependence (region II shown Fig. 3.3a) to be able to balance the signal contribution from the soot particles exposed to fluences in the low-fluence region with the positive fluence-dependence. For such an experimental setup, the signal is essentially independent of the laser fluence in a certain fluence regime. This regime is often referred to as the plateau region and is schematically represented in Fig. 3.3b. From an experimental point of view, plateau regions offer the possibility of making measurements unaffected by shot-to-shot fluctuations in laser pulse energy and nearly no influence of absorption along the laser beam propagation direction,

avoiding sometimes complex aftertreatment of the data. It is important to note that the appearance of the fluence curve also depends strongly on the gate and delay timing of the detection system. Theoretical investigations of the fluence dependence of the LII signal are presented in Paper I and are further discussed in Chapter 6.1.2.

The sublimation process responsible for the mass loss has also been investigated as a diagnostic tool. By deliberately subliming (in the literature this process is often referred to as vaporisation) part of the soot, molecular species may be probed and correlated to the soot volume fraction. Laser-vaporised C_2 has been investigated in several studies. Coherent anti-Stokes Raman spectroscopy (CARS) was early investigated [97,98] and laser-induced fluorescence on C_2 from laser-vaporised soot, LIF(C_2)LVS, was suggested as a possible technique by Bengtsson and Aldén [84]. Other techniques like degenerate four-wave mixing [99,100] and polarisation spectroscopy [101] has also been used. All these approaches rely on the assumption of an approximate linear relationship between the soot volume fraction and the produced C_2 concentrations, which has support in theoretical investigations [63].

The LII signal is isotropic and detection must not be perpendicular to the laser beam propagation direction. In attempts to simplify optical access and the experimental equipment, backward detection has been utilized both for measurements inside a carbon black production reactor [102] and for gas turbine exhaust measurements [103-105]. The experimental setup requires a dichroic mirror transmitting the laser beam and reflecting the LII signal to the detector. The backward direction enables direct studies of the influence of the spatial laser profile on the resulting LII signal [106], and in Paper II a detailed comparison between experimental and modelled LII signals is presented using the backward configuration.

If the LII technique is combined with scattering, both particle size and volume fraction may be inferred. Based on these principles the RAYLIX technique was presented by Geitlinger et al. [107,108] where it was applied in turbulent diffusion flames. It has later been applied also for high-pressure applications [109]. However, the LII technique may also be used for particle sizing. Particles of different size have different cooling rates, and thus give rise to different LII signal decays. Although suggested already by Weeks and Duley [61], the feature was first investigated for flame soot measurements by Will et al. [110] who used two imaging systems to detect both the prompt and the delayed LII signal, inferring particle sizes from the ratio pixel by pixel, thus attaining an image of the particle size distribution. When used for particle sizing, the technique is usually referred to as time-resolved LII (TIRE-LII). The trend during the last decade has been towards point measurements using completely time-resolved data from photo-multipliers in order to develop methodologies of extracting not only the particle size, but also the size distribution [111-113]. This has recently become popular also for in-cylinder measurements [114-117]. The distribution affects the shape of the signal decay due to the averaging effect of particles of different sizes having

different cooling rates. However, the approach relies on assuming a particle size distribution function, and even then, as pointed out in [64], the problem is ill-posed, leading to relatively large uncertainties.

No simple relationship exists between the primary particle sizes and the signal decay, and evaluation of particle sizes from time-resolved LII signals requires the use of a theoretical model for the LII process, like the one presented in Chapter 5. The underlying uncertainties in the model and in the choice of values for $E(m)$ and the thermal accommodation coefficient etc. thus also contribute to the uncertainties in the results. Theoretical models have been developed and used since the early days of the technique. Most current models including the one presented in this thesis are based on the one presented by Melton [63]. The primary purpose of the models has been a tool to infer particle size information, but theoretical investigations both with regards to the soot volume fraction and particle size has also been conducted [63,87,88,118-122] together with detailed analysis of some of the sub-mechanisms [123-126]. A major extension and, to some degree, reformulation of the theoretical framework for the interaction between laser radiation and soot particles has been carried out by Michelsen [38], who added a number of new mechanisms to the model, including one for thermal annealing, which is a structural reorganisation of the material within the soot particles when heated to high temperatures. The drawback of the Michelsen model is its complexity and the fact that the nature of some of the mechanisms are uncertain and also, to different degree, hard to investigate experimentally. Still the model by Michelsen can be seen as a milestone within the field of LII model research.

Relatively large uncertainties exist for all LII models at high fluence, and measurements of particle sizes are usually conducted in the low-fluence regime. Non-uniform heating of the particles introduces additional problems since particles reach different maximum temperatures resulting in the signal decay shape being dependent on an ensemble average. For this reason top-hat profiles are generally recommended [64], and a lot of work has recently been directed towards creation of near top-hat profiles by relay imaging the cut centre region of the beam into the measurement region [127-130]. This approach, though proven successful, is limiting the measurement volume length to the depth-of-field of the relay imaging system. For long measurement volumes like those obtained in the exhaust from gas turbines using the backward LII technique, the spatial profile is likely to vary within the measurement volume as function of position along the beam propagation direction. Another approach is to theoretically model the resulting decay shape using an experimentally obtained spatial profile of the laser energy. Such an investigation is presented in Paper II.

The relatively large uncertainty in the value of the absorption function $E(m)$ unfortunately also affects model predictions used to infer particle sizes using LII. During the last years, the LII community has gradually shifted to measuring the time-resolved LII signals at two wavelengths using two detectors, enabling calculations of the average temperature of the soot particles during the process as

outlined by Snelling et al. [92,93]. The technique is usually referred to as two-colour laser-induced incandescence (2C-LII) and has been carried out both at atmospheric conditions [128,129,131,132] and for in-cylinder measurements [31,117,133].

The laser-induced incandescence technique has certain advantages with respect to other optical techniques presented in this chapter. Foremost, it provides measurements with high spatial and temporal resolution enabling studies of complex combustion flow fields. Secondly, it has been shown to be highly sensitive. Soot volume fraction measurement data down to ~5 ppt has been reported [134]. Also, the technique does not require complex laser systems, and standard wavelengths of commercially available lasers may be utilized. However, improvements of the technique are still needed. The theoretical description of the laser pulse and particle interaction is improved by constant improvements of the models. Experimentally, much attention has been given the characteristics of the experimental setup, where focus has been on the spatial and temporal profile of the laser and, for time-resolved LII, the temporal response of the detector system [64,135].

3.3   Flame front visualization

Visualisation of flame fronts in combustion systems is important for many reasons. The flame front is the thin region in which the exothermic chemical reactions between fuel and oxidizer take place. These regions therefore possess strong local heat release rate and the total flame front area indicate the total heat release. Measurements on flame fronts may, especially combined with additional measurements of the flow structures using for instance particle image velocimetry (PIV), serve as validation data for turbulent combustion models.

A useful technique for flame front visualisation is the laser-induced fluorescence (LIF) technique. The fundamentals of LIF applied for combustion studies has been outlined by Eckbreth [16], Kohse-Höinghaus [136] and Daily [137]. It involves excitation of an atom or molecule to a higher electronic energy state using laser radiation matching the energy gap between the states. Moments later the atom or molecule will return to its initial state following different possible routes of energy loss. This is visualized in Fig. 3.4. The fluorescence signal is proportional to the rate constant A_{21} and the population in the upper state, N_2, which in turn is dependent on the relative rates of the other processes. However, energy loss by predissociation requires the upper state to be dissociative, and this is seldom the case. Energy loss by photo-ionization requires high laser intensity, and may thus be avoided by using lower pulse energies. It turns out to be much more difficult to avoid the collisional quenching. In the so called linear regime for LIF, the quenching rate has to be known to attain quantitative data on concentrations [16,138]. Other imaging techniques for visualising flame fronts include Schlieren
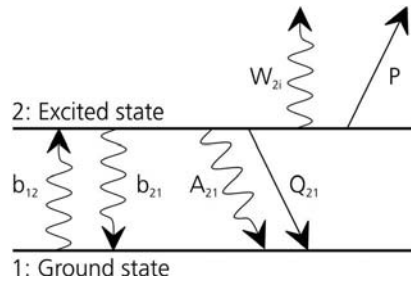
Figure 3.4 *Simplified energy level diagram of laser-induced fluorescence (LIF) with two levels. The rate constants for the different energy transfer processes are absorption b_{12}, stimulated emission b_{21}, spontaneous emission A_{21}, collisional quenching Q_{21}, predissociation P and photoionization W_{2i}.*

and shadowgraph techniques which are sensitive to density variations in the gas [9], and laser Rayleigh scattering that may be used to image the fuel distribution [139] in absence of large particles like droplets.

The flame front is usually visualised by imaging the fluorescence from species present in the vicinity of, or within the reaction zone. These species are referred to as flame-front markers. One natural flame front marker is the OH radical, formed in the flame front in combustion processes with oxygen as oxidizing species. In premixed flames, visualisation of OH will show a sharp edge between the unburned gas and the flame front while the LIF signal from OH stays high on the product gas side as long as the temperature is high because of equilibrium considerations. Another natural flame front marker is the CH radical, which is produced during the initial reaction of hydrocarbon and air. Contrary to the OH radical, CH is rapidly consumed by the next step of reactions. The CH profile is relatively thin and marks the fuel-rich side of the reactions zone [140]. Both experimental and theoretical studies suggest that the HCO radical closely matches the local distribution of heat release making this radical interesting as a flame front marker [141].

Another approach often used to visualize flame kernels propagating in premixed systems is to measure the fuel distribution. The flame front will consume the fuel as it propagates through the fuel-oxidiser mixture, enabling the contour of the flame front to be estimated from the contour of the fuel distribution. In internal combustion engines liquid fuels are used. Commercial fuels like gasoline consist of a number of different hydrocarbons, the exact fractions of which may differ from batch to batch. Even if these kinds of fuel generally can be excited by UV radiation enabling measurements using the laser-induced fluorescence (LIF) technique, it is not recommended. As the exact fuel composition is unknown, so is the pressure and temperature dependence of the fluorescence signal, introducing large uncertainties in the data. An approach circumventing this problem is to use a so called reference fuel, in the case of spark-ignition engines typically n-heptane or

24

iso-octane, or a mixture of these. These fuels are not easily excited by lasers, and in order to measure the fuel distribution, an added tracer species is usually used. Examples of such tracer species are acetone, 3-pentanone and toluene. A recent review on tracer species for laser-induced fluorescence measurements has been given by Sick and Schulz [142]. Tracer species should comply with certain requirements. From a diagnostic point of view, the tracer species should be possible to excite using readily available laser wavelengths and have a fluorescence spectrum separated from the absorption spectrum to avoid signal trapping (fluorescence signal absorbed in other tracer molecules on its way to the detector inevitably reducing the measured signal). The fluorescence signal dependence on temperature and pressure should be well-characterised and as weak as possible. In order to successfully represent the fuel distribution, the tracer has to be soluble in the liquid fuel mixture and should have essentially the same evaporation and diffusion characteristics as the fuel mixture in the gas phase. Additionally, tracer species should not affect the characteristics of the combustion process, such as for instance the auto-ignition temperature.

An alternative approach to adding a fuel tracer is to measure the distribution of a naturally formed species within the fuel, thus acting as a natural fuel tracer. This is practically possible for fuels which during the combustion process feature prominent low-temperature chemistry prior to ignition [143,144]. In spark-ignition engines, as the increasing pressure forces the temperature to rise, intermediate species like aldehydes are formed at a relatively slow rate. As ignition takes place, the high-temperature chemistry takes over resulting in fast oxidation of the intermediates. Formaldehyde, CH_2O, has been found to be one of the most abundant intermediates, making it a suitable natural tracer species. The molecule is possible to excite using the Nd:YAG laser operating at 355 nm, an alternative that offers a convenient way of ensuring high pulse energies and good signal-to-noise ratio [145]. Several groups have used formaldehyde to detect so called hot spots in spark-ignition engines [144,146-148]. These hot spots are regions in the unburnt mixture that are hot enough to self-ignite before they are reached by the main combustion initiated by the spark plug. The presence of such self-ignition regions results in what is referred to as engine knock, a phenomenon resulting in audible noise and risk of damage to the mechanical parts [9]. Formaldehyde visualisation has also been used to characterise combustion processes in so called homogeneous charge compression ignition (HCCI) engines [149-151].

Chapter 4

Experimental equipment and objects

The purpose of this chapter is to give brief descriptions of the main experimental equipment and measurement objects used within this work. Laser-diagnostic measurements usually involve complex setups with lots of additional equipment not discussed here. For instance complex triggering systems using pulse generators are frequently utilized in order to control the timing of the detector exposure time with respect to the laser pulse. When conducting crank-angle resolved measurements in internal combustion engines the triggering has to be initiated by the position of the piston, meaning that both the laser and detector systems have to be triggered externally. Other experimental equipment frequently used involve power meters measuring the laser pulse energy, photo diodes detecting the temporal distribution of the laser pulse energy, oscilloscopes measuring the output from diodes and photomultipliers and of course different kinds of optics.

4.1   The Nd:YAG laser

The techniques used in this work have been based on the use of Nd:YAG lasers (Paper II, III and V). Some characteristics of laser radiation were previously discussed in chapter 3.1, and for a more extensive description of the fundamentals of lasers the reader is referred to the text books by Svelto [152] and Siegman [153]. Nd:YAG lasers are solid-state lasers where the active medium consists of neodymium ions, Nd^{3+}, which are doped inside an yttrium-aluminium-garnet, $Y_3Al_5O_{12}$, (YAG) crystal [152]. Laser action arises through so called stimulated emission, a process schematically illustrated in Fig. 4.1a within the dotted square. An incoming photon with a frequency that matches the energy between two energy levels (corresponding to level 3 and 4 in Fig. 4.1a) may induce emission of a second photon with the same frequency, phase and propagation direction as the incoming. This process, which essentially involves a cloning process of incoming photons into new identical ones, is the source of the light generation used in lasers. For stimulated emission to occur in real media, a high number of the atoms or ions making up the active medium have to be in an excited state. One usually refers to a
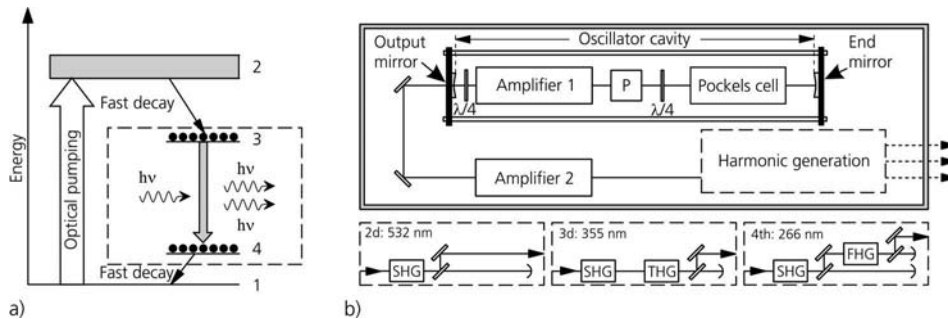
Figure 4.1 *The principle of the Nd:YAG laser. In a) a simplified four-level energy diagram for the Nd³⁺ ions is shown. The typical arrangements inside a Nd:YAG laser together with the frequency generation schemes are depicted in b). SHG = Second harmonic generation, THG = Third harmonic generation, FHG = Fourth harmonic generation, P = Polarizer, λ/4 = quarter wave plate.*

population inversion between two involved energy levels. For the Nd:YAG laser this is achieved using a four-level pumping scheme as depicted in Fig. 4.1a [154].

All neodymium ions are initially in the ground state (1) where they are excited into higher-order states (2) using strong flash-lamps or other light sources. Rapidly non-radiative transitions will occur to a storage level (3) which is metastable, i.e. the lifetime of neodymium ions existing in this state is relatively long. If level 4 is relatively fast depopulated, i.e. has a short life-time, and pumping is efficient enough, a population inversion may be built between level 3 and 4 enabling stimulated emission.

The formation of a strong beam of laser radiation from the photons created inside the active medium is controlled using a positive feedback system, an oscillator cavity. This is illustrated in Fig. 4.1b. The cavity is defined by one end mirror with almost perfect reflectance and one output mirror with partial transmittance. The purpose of the cavity is to create a long path length of selected parts of the radiation within the cavity by sending it back and forth. As the photons pass through the Nd:YAG crystal (located inside Amplifier 1) they will be amplified and eventually a very high photon density will be built inside the cavity. A fraction of this radiation will constantly slip through the output mirror thus forming the laser beam. The Nd:YAG lasers used in this work are pulsed high-power lasers. The pulsed mode operation is achieved by first preventing free passage inside the cavity as the amplification in the active medium is built up. At a specified time the radiation is made free to pass, creating a burst of laser light from the output mirror, called a laser pulse. This process is referred to as Q-switching. Typically the very fast switching is realized using polarisation changes. A combination of quarter wave plates, a polarizer and a Pockels cell consisting of a crystal with the ability to change the polarisation of the transmitted light when subjected to an external voltage, is used as an electronic shutter mechanism. As no

voltage is applied no light will be able to pass the Pockels cell, and the gain is built inside the active medium. As the voltage is applied to the cell, the radiation will be able to pass creating a laser pulse. The voltage is synced in time to the flash lamps pumping the Nd:YAG crystals ensuring optimal pulse stability and power. Typical repetition rates are tens of Hz. Q-switching can be made very fast using very short high-voltage pulses to the Pockels cell, and the typical pulse duration used for the work presented here is 8 ns. The output beam from the oscillator is further amplified by a factor of ~4 in an external amplifier (Amplifier 2).

The fundamental wavelength from a Nd:YAG laser is in the near infrared at 1064 nm, and by utilizing frequency-doubling and frequency-mixing crystals, part of the output power at this wavelength may be transformed into the second harmonic at 532 nm, the third harmonic at 355 nm and the fourth harmonic at 266 nm. Special dichroic mirrors reflecting only specified wavelengths are used to separate one wavelength from another. The different schemes used to create these wavelengths are depicted in Fig 4.1b.

4.2   Detectors

There exist a number of detector types for studies of fluorescence, incandescence and scattering processes in combustion. As previously mentioned, detectors are also used to characterise the laser pulses used to induce the signals. Here will be given a brief description of some of the detectors used within this work.

4.2.1   The ICCD camera

Incandescence and fluorescence imaging measurements presented in Paper II, III and V have all been performed using ICCD (Intensified Charged-Coupled Device) cameras, which principle operation is depicted in Fig. 4.2a. Light is collected onto a photocathode which converts the incoming photons to electrons. These are amplified in a microchannel plate (MCP), which consists of numerous narrow channels (Fig. 4.2b). As an external voltage is applied to the MCP, electrons are forced through the channels constantly impinging on its walls. These are covered with a material which easily gives rise to secondary electrons and thus an avalanche of electrons is created and accelerated onto a phosphorescent screen reconverting the information into photons. These are transferred by either a fibre-optic coupling or a lens system onto the CCD chip, which consists of a large number of light-sensitive elements structured as a matrix. The intensities detected by the chip are read out to a computer. The nice feature with this construction is that a high amplification is achieved while maintaining the spatial resolution of the signal throughout the system. The microchannel plate also works as an electronic shutter enabling very short exposure times in the nanosecond range to be used. This may efficiently discriminate from background luminescence when performing
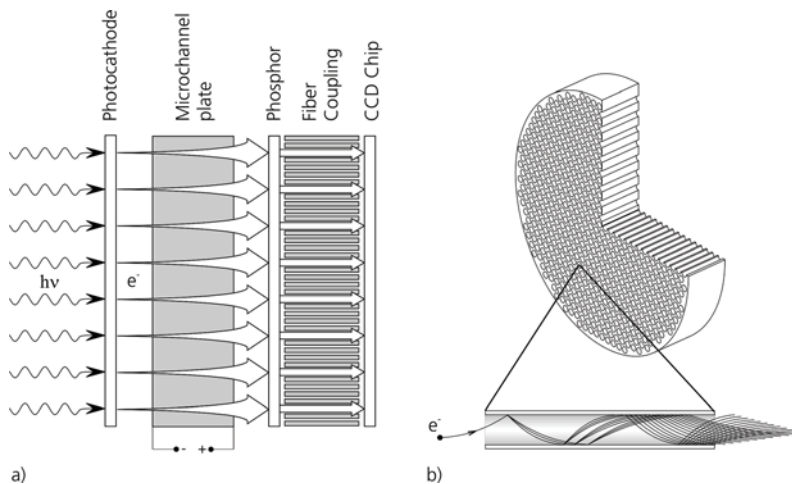
Figure 4.2 *In a) the principle operation of an ICCD camera is shown, and b) shows the electron amplification process inside a microchannel plate (MCP).*

measurements in combustion environments. Another nice feature is that the instrument response is approximately linear with signal intensity. The spectral sensitivity is non-uniform, however, and must be measured and corrected for if detailed investigations of spectra or comparison between signal yields at different wavelengths are to be conducted.

4.2.2 The photomultiplier tube

Photomultiplier tubes are used for point measurements and provide time-resolved data. Such a device has been used within the work presented in Paper II. The principle operation is depicted in Fig. 4.3. Light incident on the photocathode initiate a release of electrons from the material by the photoelectric effect [154]. These electrons are accelerated and focused onto the first in a chain of dynodes, covered with a material which easily emits secondary electrons – similar to what occurs in the narrow channels of the MCP discussed in chapter 4.2.1. The process
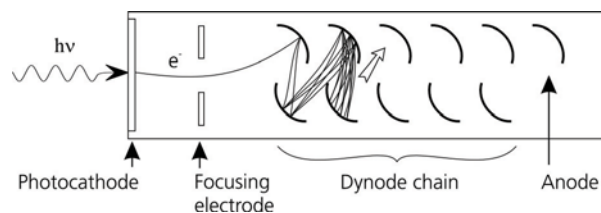
Figure 4.3 *The principle operation of the photomultiplier tube (PMT).*

is repeated until the heavily amplified electron shower reaches the anode which connects to a load resistor measuring the resulting voltage. Photomultipliers can be made extremely sensitive and are capable of detecting single photons. Typical temporal responses of PMT's are around 1 ns, but faster responses are readily available. Different photocathode materials must be used dependent on the spectral characteristics of the signal it is intended to measure.

4.2.3   The beam profiler CCD camera

The spatial distribution of laser energy within a laser beam has turned out to be very important for correct interpretation of the signals generated from the laser-induced incandescence technique. Traditionally the spatial distribution was estimated using for instance the razor blade method, where a sharp razor blade is gradually inserted in the beam perpendicular to its propagation direction, and the total transmitted laser power is measured after the razor blade as function of blade position. The derivative of the transmitted signal with respect to the spatial position of the razor blade yields the profile. This technique, however, will only measure the beam profile in one dimension, meaning that the information will be spatially averaged in the other.

Nowadays detectors equipped with CCD chips are readily available for direct imaging of the beam profile. These are sometimes referred to as beam profilers. The drawback of these devices is that they can not endure the high laser intensities typical for the LII and LIF techniques, and the original beam therefore has to be highly attenuated before contact with the CCD chip. It is very important that optics used for attenuation do not influence the spatial profile in any way and since the profile is likely to change its appearance along the propagation direction of the laser beam, care must be taken to ensure that the profile corresponding to the correct position is detected. This may be carried out using a combination of a series of secondary reflections from wedged glass plates and neutral density (ND) filters as depicted in Fig. 4.4. The total path length from the first wedged plate to the profiler CCD chip must be equal to the path length from the first wedged plate to the measurement region. In the work presented in Paper II a beam profiler from
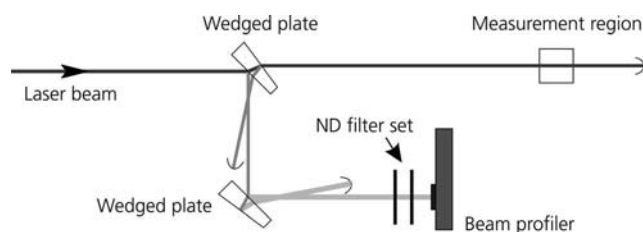
Figure 4.4 An example of an experimental setup for online monitoring of the spatial profile of the laser energy. The use of wedges plates avoids interferences from secondary reflexes.

31

Dataray Inc. [155] was used to measure the beam profile online. The profiler is equipped with a 1360×1024 pixels CCD chip with square pixel sizes of 4.65 μm and is thus able to resolve relatively small spatial frequencies in the profile.

4.3 Laboratory burners

Experimental work has been performed in flames of two different kinds: Premixed flat flames and diffusion flames. The burners and the typical characteristics of the flames they create will be discussed in this chapter.

4.3.1 The porous plug burner

Premixed flat flames are well suited as calibration sources since they are essentially one-dimensional, i.e. only show varying properties as function of height above burner. The nearly uniform properties as function of radial position enables extinction measurement to be carried out without complicated inversion schemes like those usually applied for measurements in diffusion flames. Flat flames are created using so called porous plug burners, often referred to as McKenna burners after the main manufacturer formerly known as McKenna products (nowadays called Holthuis & Associates [156]). Figure 4.5 shows the construction of this kind of burner. The premixed flow of fuel and air enters from the bottom and is pushed through the centre plug made of sintered metal, typically steel or bronze. A secondary plug, concentrically positioned around the main, makes it possible to use
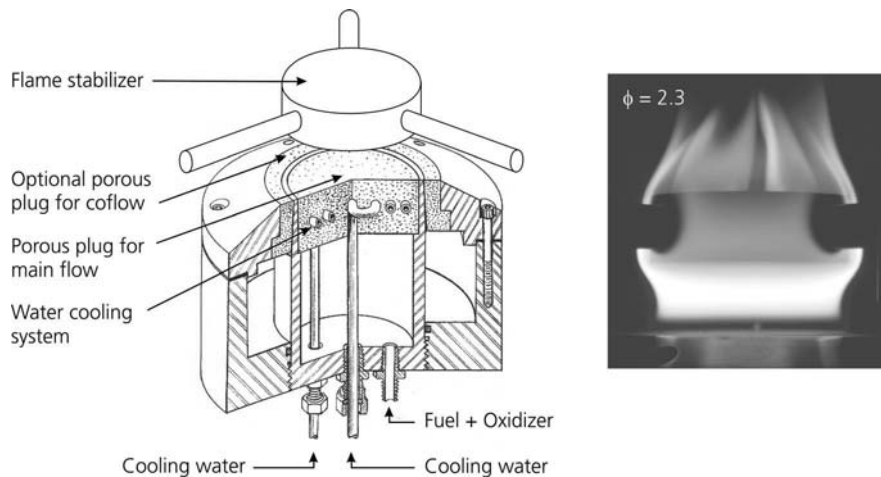
Figure 4.5 *The construction of the McKenna burner. The flame stabilizer with its three mounting rods is located 21 mm above the top of the burner. The photograph shows an ethylene-air flame with the equivalence ratio of 2.3 on the McKenna burner.*

a co-flow, usually of nitrogen to act as a shielding layer to the inner flow protecting it from air movement in the laboratory. The flame is stabilized by a steel cylinder with the same diameter as the inner plug (6 cm), mounted 21 mm above the top of the burner. With a specified gas flow rate (~10 l/min) this ensures laminar conditions in the region between the burner and the steel plate, making it suitable for averaging measurements. The reaction zone in these flat flames are located approximately 1 mm above the plug surface and has the appearance of a thin blue disc. The fact that the hot flame front is located so close to the plug requires water cooling to prevent the sintered metal to melt. For equivalence ratios high enough, soot formation will occur. A photograph of a sooting ethylene-air flame is shown in Fig. 4.5. Due to the laminar gas flow and the reaction zone being located at the bottom of the volume between the burner and the stabilizer, the soot formation process discussed in Chapter 2 will develop as function of height above the burner. This means that the spatial scale (the height above burner) corresponds to a time scale for the soot formation process. The flame depicted in Fig. 4.5 was used to calibrate the LII measurements carried out in a Diesel engine in the work presented in Paper III.

4.3.2 The hybrid porous plug burner with central injector

One drawback of the flat flames discussed in Chapter 4.3.1 when conducting soot measurements with optical techniques is that the large size of the flame results in long path lengths leading to relatively high level of attenuation. Additionally, the soot volume fraction is increasing as function of height above burner. In the work presented in Paper II these effects would create large problems with signal interpretation, and a much smaller flame with nearly constant volume fraction as function of height over some millimetres was needed. The solution was to use a diffusion flame. For this purpose the hybrid burner from the group of Pascale Desgroux in Lille was used. The burner is schematically shown in Fig. 4.6. The
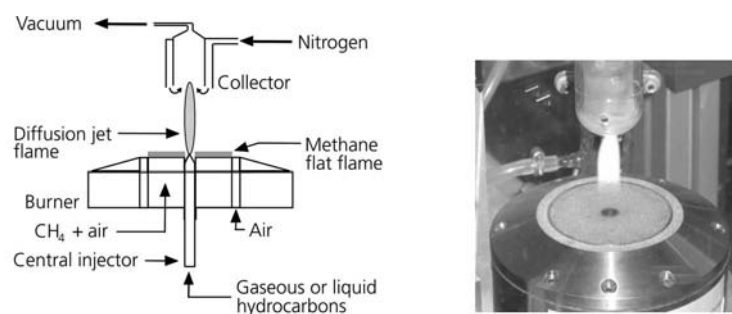
Figure 4.6 *The schematics of the hybrid porous plug burner equipped with a central injector, together with a photograph showing the laminar methane diffusion flame investigated in Paper II.*

burner consists of a modified McKenna burner where a stainless-steel injector has been inserted in the centre of the porous plug. The fuel enters the pipe from the bottom and reacts with the surrounding air forming a jet diffusion flame. A premixed flame mounted on the inner porous plug serves to stabilise the diffusion flame. Further stabilisation is achieved by using a quartz collector mounted 50 mm above the burner. This collector is usually used to sample exhaust from the flame. A shielding co-flow of air in the secondary porous plug also promotes flame stability. In the work presented in Paper II a methane diffusion flame was created using this burner, and a photograph of the flame is shown in Fig. 4.6.

4.4   Internal combustion engines

The work presented in Paper III and V involves measurements inside the combustion chamber of two different types of internal combustion engines. In this chapter brief descriptions of the two engine types will be given together with a description of the approach used to obtain optical access to the combustion chamber. A thorough description of the fundamentals of internal combustion engines is given by Heywood [9].

4.4.1   The spark-ignition engine

In Paper V measurement series carried out inside the combustion chamber of a spark-ignition (SI) engine is described. These kinds of engines operate with premixed fuel and air ignited using an electric discharge. The most common types of SI engines used within the transportation sector are four-stroke, often referred to as Otto engines after Nicolaus A. Otto, who constructed the first prototype based on this scheme in 1876 [9]. The typical four-stroke cycle of an Otto engine is shown in Fig. 4.7.

During the intake stroke the inlet valves are open and the downward motion of

Figure 4.7 *The principle operation of a 4-stroke Otto engine with pent-roof design.*

the piston draws fresh mixture into the combustion chamber. Before entering the compression stroke, the inlet valves are closed, whereby the gas mixture is compressed by the upward motion of the piston. Spark-ignition engines run on high-octane fuels like gasoline and are nowadays typically port-injected. This means that the liquid fuel is injected into the intake ports, usually prior to the opening of the inlet valves, and vaporisation will be initiated. As the inlet valves open,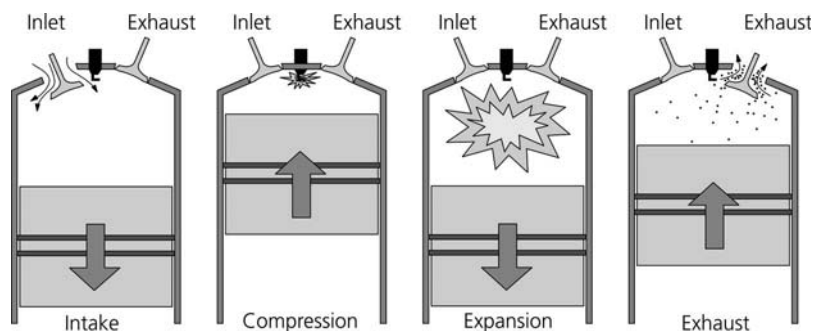 the fuel is already partially vaporised, and vaporisation will continue inside the cylinder and are to be completed during the compression stroke in order to create a homogeneous fuel-air mixture. An electric discharge from a spark plug initiates combustion and the piston is forced downwards as a result of the heavy expansion of the gases due to the exothermic reactions. Finally the cycle is finalised by the exhaust stroke during which the upward motion of the piston pushes the exhaust gases out through the open exhaust valves.

Since a premixed gas mixture is used, the compression ratio of SI engines must be kept low enough to avoid auto-ignition in the fresh charge prior to the spark-induced combustion, a fact that limits the efficiency of these engines. Auto-ignition in SI engines may also lead to the phenomenon known as engine knock. This phenomenon has its origin in the strong pressure rise rates induced by the rapid combustion, leading to oscillating pressure waves within the combustion chamber, creating an audible noise. A more serious problem than the noise is that engine knock may damage the internal parts of the engine. The main advantages of the SI engine are its high power density and low emission levels, provided that a three-way catalyst is used.

4.4.2   The Diesel engine

Instead of actively igniting the fuel using a discharge, the mere compression of a flammable gas mixture may in itself initiate ignition. This was indeed the process responsible for the engine knock phenomenon of SI engines discussed in Chapter 4.4.1. By injecting the liquid fuel directly inside the combustion chamber during the compression stroke for a specified position of the piston, the process may be controlled and thereby be of practical use. The idea was described by Rudolph Diesel in a patent from 1892, and five years later a practical engine based on these principles had been developed. Diesel engines also exist both in two- and four-stroke versions, the former design often used for large-scale engines for instance in ships. The principle operation of a four-stroke Diesel engine is shown in Fig. 4.8.

During the intake stroke, air is drawn into the combustion chamber. Diesel engines are often operated supercharged enabling larger volumes of air to be used than if only naturally aspirated. The air is compressed during the compression stroke and at a specific position of the piston, fuel is injected and vaporised by the high temperature environment resulting from the compression. Often a bowl-in-piston design is used, which combined with a swirling air flow set up by the design of the intake manifold system, promotes efficient mixing during the vaporisation
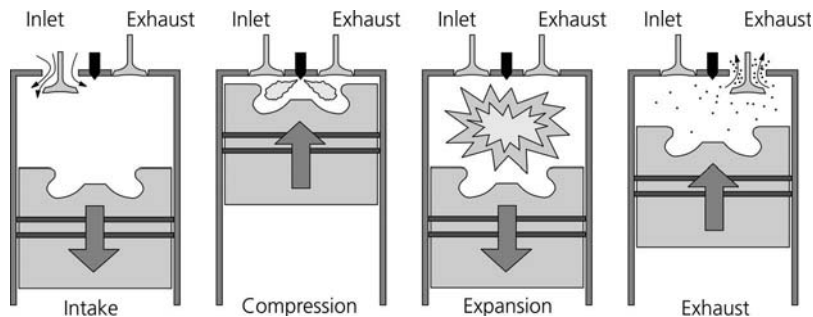
Figure 4.8 *The principle operation of a 4-stroke Diesel engine.*

phase. As the mixture ignites, the piston is forced downwards, and finally the exhausts are pushed out of the combustion chamber during the exhaust stroke.

Since no premixed charge is used in Diesel engines, engine knock is not a problem and much higher compression ratios may be used, which increases the efficiency of the engine. Soot emissions are a problem with Diesel engines and result from strong soot formation occurring in regions of the charge where full vaporisation and mixing have not yet been achieved. Even if Diesels are run at overall lean conditions minimizing the particulate formation, locally fuel-rich regions still occur especially at high load. Soot oxidation within the cylinder is quite strong, and most of the soot formed will be oxidized before the exhaust stroke. To prevent emissions of the remaining part, particulate filters are becoming more readily available for exhaust aftertreatment. In an attempt to reduce soot formation as well as increasing fuel efficiency, the trend towards higher injection pressures has been ongoing for some time. With higher injection pressures, smaller fuel droplets are created, which leads to more efficient vaporisation. The high-velocity fuel jets also promote air entrainment and thus the mixing process. One drawback of this development is that soot emissions, though reduced in total volume fraction, tend to consist of ultra-small particles which are especially harmful for humans as previously described in Chapter 1. Diesel engines have a lower power density than SI engines due to the higher peak pressures requiring the structure to be more robust. The overall lean combustion process needed to decrease soot emissions has led to a frequent use of supercharging. The main advantage of Diesel engines compared to SI engines is the higher efficiency especially when run at part load.

4.4.3   Optical access

Optical measurements inside the combustion chamber of internal combustion engines have been carried out for many decades. Methods for optical access include glass or quartz windows inserted as replacement for one of the valves as well as

endoscopic imaging systems. The work presented in this thesis has utilized a scheme based upon an elongated piston design, often referred to as the Bowditch design after its inventor [157]. The principle is visualised in Fig. 4.9.

The ordinary steel piston is extended with a hollow cylinder on top of which a quartz window is mounted giving optical access to the combustion chamber from below. Two oblong openings on opposite sides of the extension enable both mounting of a mirror on the engine block, and optical access from outside to the interior of the piston extension. The cylinder liner also has to be extended, and equipped with an opening for optical access. The Bowditch design enables optical access from below and is mostly used for signal detection. One drawback of the hollow cylinder construction is that the view is limited near the cylinder wall, which has been discussed in Paper V when conducting flame propagation imaging. Optical access from the sides can be achieved using quartz parts inserted as part of the cylinder liner. In the work presented in Paper III and V a quartz ring was used, enabling access from all directions not obstructed by the four support beams (See Fig. 4.9). For laser-based measurements this ring is most frequently used for enabling the laser beam to propagate through the engine. The optical parts have a substantial impact on the heat transfer characteristics of the engine and, due to the fragility of the material, also on the compression ratio and load for which the engine can be operated. For this reason a number of engine parameters like inlet gas temperature, start of injection and spark timing are adjusted in order to simulate the conditions in real engines.
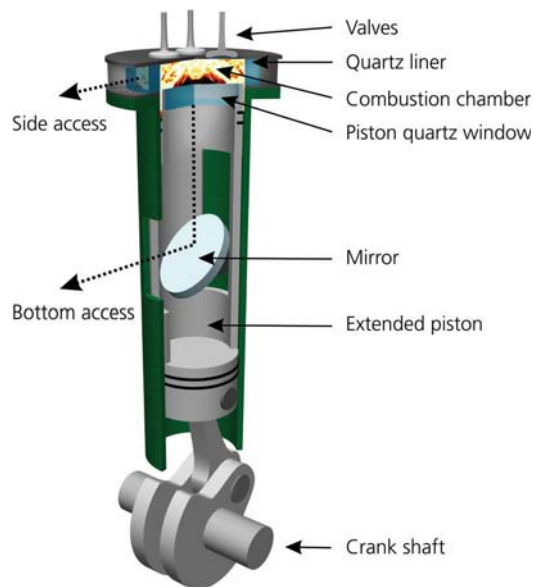
Figure 4.9 *Three-dimensional view of a research engine equipped with optical access from below via an elongated piston (the Bowditch design) and from the sides via a cylinder quartz ring inserted as part of the cylinder liner.*

Chapter 5

The model for laser-induced incandescence

In this chapter the theoretical model for predicting the physical processes occurring during laser-induced heat-up of soot particles will be presented. The laser-induced incandescence (LII) technique was described in Chapter 3 and the current chapter will solely focus on the theoretical framework. The description given in this chapter will be based on the current version of the model which means that there may be some differences when comparing to older versions used within some of the papers in the thesis.

5.1   Overview of the model structure

The aim of this chapter is to give an overview of the complete model package developed within the framework of the thesis in order to demonstrate the applicability of the model for predicting realistic experimental conditions. The complete model package is based on a heat and mass transfer (HMT) model, which physically describes the interaction between laser light and soot particles. Given a set of input parameters defining the physical conditions, the HMT model will output a time-resolved LII signal. Results from this model will not be directly comparable to results obtained from experiments since soot particles within a measurement volume are of different size and will be exposed to different laser fluences due to the non-uniform spatial distribution of laser energy present in most laser beams. The purpose of the complete model package is its direct applicability to a real experimental setup, and for this reason these effects have been incorporated into an overall structure. The details of the HMT model are given in chapter 5.2.

   The basic flow scheme is shown in Fig. 5.1. The non-uniform distribution of laser energy within the measurement volume can be defined both radially (cross section profile) and along a laser beam propagation direction (propagation profile) by defining distribution functions that together with the total laser pulse energy is used to define a range of laser fluence values for which the heat and mass balance is solved. The temporal distribution of the laser pulse (temporal profile) and the laser

Laser pulse	Soot properties	Gas properties	Detection

Pulse energy
Temporal profile
Spatial distributions:
  Cross section profile
  Propagation profile
Wavelength
	Absorption function
	Size distribution
	Morphology
	Heat of vaporization
	Vapor pressure
	Molecular weight
	Specific heat
	Density
		Temperature
		Pressure
		Thermal accomodation
		Heat conduction coeff.
		Heat capacity
			Spectral sensitivity
			Gate
			Delay

The model for LII

Time-resolved signal	Images of gated signal	Fluence curve

Figure 5.1 *Overview of the model for laser-induced incandescence.*

wavelength are also needed. The properties of soot are used to predict the response of the soot particles to the laser radiation and include the possibility of using arbitrarily defined primary particle size distributions and accounting for aggregation. The model may be applied for both atmospheric and high pressure conditions. The spectral sensitivity of the detection system (defined by the characteristics of the filter, collection optics and detector sensitivity) may be defined arbitrarily facilitating direct comparison with measurements when using broadband detection. The gate and delay time is used for creating predictions of time-integrated signals. Given this set of input parameters, the HMT model is used to calculate the LII signal response. There are three output options, where the first is the pure time-resolved modelled LII signal. The program may also output images of time-integrated signals which correspond to experimentally obtained soot volume fraction data using an ICCD camera. The last output option gives the total integrated signal as function of laser fluence, i.e. the fluence curve of the system. The program assumes a homogeneous distribution of soot properties within the measurement volume, i.e. the optical properties as well as the size distribution, morphology and other physical properties are constant. This means that any variation in signal strength within an image is solely due to the fluence dependence of the system.

5.2   The heat and mass transfer model

The core of the complete model package is the heat and mass transfer (HMT) model. This consists of a set of differential equations in the time-domain, modelling the internal energy and mass of soot particles when exposed to a nanosecond laser pulse. The model used in this thesis is based on the one outlined by Eckbreth [62] and Melton [63] and later refined by Hofeldt [158] and Snelling et al. [118]. It consists of two differential equations, where the first contains an energy balance and the second a mass balance. Before discussing these equations and how they are used to derive an LII signal, the different physical mechanisms that makes up the equations will be discussed. These are illustrated in Fig. 5.2.
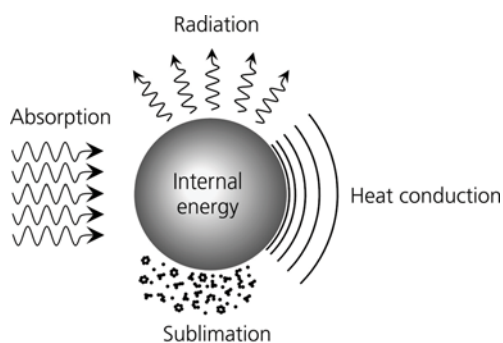
Figure 5.2 *The physical mechanisms illustrated here for a single primary soot particle when exposed to laser radiation.*

Part of the energy in the laser pulse is absorbed by the particle increasing its internal energy and hence temperature. A number of loss mechanisms will counteract this energy increase. The gas molecules surrounding the soot particle will remove energy at the particle surface by collisions and this is modelled as heat conduction. Emission of visible and infrared light will increase heavily with temperature thus contributing to the energy loss. This is the emission detected as the signal using the LII technique. As particle temperatures approach 4000 K, parts of the carbonaceous matter will sublime giving rise to both an energy and mass loss.

There are a number of simplifications in this representation of laser radiation and soot matter interaction. Firstly, it is assumed that the particles are spherical and consist of a homogeneous bulk material which does not change its optical and physical properties with temperature. Secondly, there may be important additional processes occurring not yet accounted for in the model. Some of these issues have been discussed by Michelsen [38], who proposed an improved model incorporating effects like thermal annealing, which accounts for a structural reorganisation of the carbon matter within the soot particle with increasing temperature, effectively

changing both the physical and optical properties of the particle. She also added new mechanisms like for instance oxidation and nonthermal photodesorption.

5.2.1 The physical sub-mechanisms

As described in the last section, the interaction between the laser pulse and the soot particle may be described using several physical mechanisms. These will be described in detail in this chapter, following directly after a description of the model for particle aggregation. A list of nomenclature is given in Appendix A, and a number of functions like for instance the temperature-dependent expression for the heat of sublimation of soot is given in Appendix B.

5.2.1.1 Aggregation

As discussed in Chapter 2, soot particles in real combustion systems tend to form aggregated structures of somewhat different morphology. A number of studies (See for instance [159] and references therein) have shown that flame-generated particles can be approximated using a statistical scaling law for the mass-fractal structure. This law can be written in terms of the number of primary particles per aggregate, N_p, according to [121,160]

$$N_p = k_f \left(\frac{R_g}{D/2} \right)^{D_f} ,$$

$$(5.1)$$

where k_f is the fractal prefactor, D_f the fractal dimension, D the primary particle size and R_g the radius of gyration of the soot aggregate defined according to

$$R_g^2 = \frac{1}{N_p} \sum_{i=1}^{N_p} (\mathbf{r}_i - \mathbf{r}_0)^2, \quad r_0 = \frac{1}{N_p} \sum_{i=1}^{N_p} \mathbf{r}_i ,$$

$$(5.2)$$

in which the vectors $\mathbf{r}_i$ define the centre of the ith sphere (primary soot particle) within the aggregate and $\mathbf{r}_0$ the aggregate centre [121,160]. This scaling law has been found to describe the real case accurately for many types of fuel [159] and is thus adopted for defining the influence of aggregation on the physical processes during LII. The influence of aggregation on the individual sub-mechanisms will be discussed in the respective chapter.

5.2.1.2 Absorption of laser radiation

The absorption term represents the only process in the HMT model that actively contributes to the internal energy storage of the particle. The term includes a model for the absorption cross section of a soot particle weighted with the intensity profile of the laser pulse according to

$$\dot{Q}_{abs} = C_{abs}F \cdot g(t), \qquad (5.3)$$

where F is the laser fluence and $g(t)$ is the normalised temporal distribution of the laser energy. The absorption cross section of a spherical particle can be significantly simplified if using the assumption that the particles are much smaller than the wavelength of the incoming radiation, the so called Rayleigh limit (See Eq. 3.1). Utilizing this assumption, the absorption cross section for one single spherical particle can be written as [37,38,118]

$$C_{s,abs} = \frac{\pi^2 D^3 E(m)}{\lambda}, \qquad (5.4)$$

where $E(m)$ is the absorption function which is related to the complex refractive index of the particle material, m, according to

$$E(m) = -\mathrm{Im}\left(\frac{m^2 - 1}{m^2 + 2}\right). \qquad (5.5)$$

The Rayleigh limit approximation will be violated as the ratio between the primary particle size and the wavelength becomes too large, and instead full Mie theory must be applied. This approach has sometimes been used for modelling the LII signal behaviour in the past [63,88] but in most studies, including those within this thesis, the Rayleigh approximation has been applied. Liu et al. [161] has recently compared the results obtained by using the Rayleigh approximation and the full Mie theory, and their results indicate that the influence on the model predictions becomes large enough to be considered at least for the largest soot particle sizes and when using 532 nm excitation.

When the primary particles form aggregates, the absorption cross section will deviate from the one obtained using the Rayleigh approximation. Studies have shown that the Rayleigh-Debye-Gans theory for poly-fractal aggregates (RDG-PFA) can be used to describe the process provided that the primary particle sizes and the number of particles per aggregate are not too large [64]. The error introduced by treating the radiation properties using the RDG-PFA approximation has been reported less than 10% for wavelengths above 500 nm and particle sizes below 60 nm for typical values of the refractive index and aggregate sizes as large as 300-500 primary particles [39,64]. The total absorption cross section for an aggregated particle will, within the limits of the RDG-PFA approximation, be related to the cross section of the primary particles given in Eq. 5.4 solely by multiplying with the number of aggregates, N_p [37]. The total absorption rate of an aggregated particle may thus be written as

$$\dot{Q}_{abs} = C_{s,abs}N_p F \cdot g(t) = \frac{\pi^2 D^3 E(m)N_p F}{\lambda} g(t). \qquad (5.6)$$

Accurate modelling of the absorption process is difficult for several reasons. One of the most critical is the uncertainty in the value to use for the refractive index of soot, *m*. This is one of the reasons why some LII models used for inferring particle size information from experiments rely on experimentally obtained maximum particle temperatures as initial conditions instead of modelling the absorption [31,111,114].

5.2.1.3 Heat conduction

The heat conduction mechanism represents the energy loss at the particle surface due to collisions with the surrounding gas molecules, and is the major contributor to the LII signal decay shape at longer delay times after the laser pulse. What complicates matters is that heat conduction typically encountered during the LII process, especially at elevated temperatures, occurs in the transition regime, for which no simple theory exist. This is discussed by Liu et al. in a recent review [125].

In conditions with low concentrations of gas molecules (i.e. low pressure conditions) heat conduction occurs in the free molecular regime. Few molecules will actually hit a soot particle, but if they do, they are likely to be able to carry energy far away from the particle without loosing it to other molecules on its way. Essentially every molecule-particle collision that does occur will thus fully conduct energy to the bulk gas. This means that heat conduction will be dependent on the molecule-particle collision rate (i.e. pressure-dependent) and the probability of energy exchange during such collisions. If, on the other hand, there is very high number density of molecules (i.e. high pressure conditions) the probability of particle-molecule collisions will be much higher effectively increasing heat transfer. However, the high number density will also give rise to high levels of molecule-molecule collisions effectively impeding energy transfer from the particle surface to the gas. It is now less likely that the energy removed from the particle by a specific molecule will ever reach the bulk gas. For molecule number densities high enough, heat conduction will be nearly pressure-independent. This regime is called the continuum regime. The heat conduction theories for these two extreme conditions are well developed and analytical expressions may be applied. It becomes much more complicated when considering what happens at intermediate pressures. This region is referred to as the transition regime.

A dimensionless number defining approximate limits between the regimes is the *Knudsen number* defined as

$$\mathrm{Kn} = \frac{\lambda_g}{L_c}, \qquad (5.7)$$

where λ_g is the mean free path of the gas and L_c is a characteristic length scale of the particle. Here the radius of the primary particles will be chosen as the

characteristic length following Liu et al. [125]. The mean free path can be defined a little different depending on the molecular model that is used to define the molecule-molecule collisions, as pointed out by Liu et al. [125]. The expression used in this thesis is the one given by McCoy and Cha [162] which can be written as

$$\lambda_g = \frac{k_g(T_g)}{f(T_g)p}\left(\gamma(T_g)-1\right)\sqrt{\frac{\pi m_g T_g}{2k_B}}\ .$$

(5.8)

An approximate limit for where the free molecular regime heat conduction can be used is for Kn>10. For atmospheric pressure flames where the mean free path is about 580 nm (0.1 MPa, 1800 K), this condition is satisfied. At higher pressures like those encountered in internal combustion engines, the Knudsen number will be close to unity and the continuum regime heat conduction will become important.

Aggregation is believed to influence the heat conduction process due to the so called shielding effect, which effectively reduces the heat conduction rate of an aggregated particle with respect to the total heat conduction rate if the primary particles were to be isolated from each other. One suitable property to derive from an aggregation model acting as a sub model within the LII model is the diameter of an equivalent sphere with the same effective area for the physical process as that of the aggregate. This has been derived for the heat conduction process by Liu et al. [121] where numerical simulations of soot aggregates were performed using direct simulation Monte Carlo (DSMC) with the characteristics described by Eq. 5.1 using k_f = 2.3 and D_f = 1.78 for aggregate sizes ranging 1-199 for N_p. The effective heat conduction diameter D_{HC} can be defined as [121]

$$\begin{cases} D_{HC} = D, & N_p = 1 \\ D_{HC} = \left(\dfrac{N_p}{k_h}\right)^{1/D_h} D, & N_p > 1 \end{cases},$$

(5.9)

where the scaling parameters k_h and D_h can be written as

$$\begin{cases} k_{h,FM} = 1.04476 + 0.22329\alpha + 7.14286\times10^{-3}\alpha^2 \\ D_{h,FM} = 1.99345 + 0.30224\alpha - 0.11276\alpha^2 \end{cases},$$

(5.10)

in which α is the thermal accommodation coefficient determining the probability of a molecule to undergo energy exchange with a soot particle during a collision. These simulations are made for the free molecular regime which puts restrictions on its applicability within the heat conduction model as will be further discussed later in this chapter. The approach of utilizing an equivalent sphere for the

complete aggregate is an approximation of the real case. For instance, the fractal aggregates are likely to be experiencing a varying heat conduction rate along the surface of the particle, meaning that the internal energy storage and hence the particle temperature will vary within an aggregate [121].

Two different heat conduction models have been used in this thesis. The first is the one proposed by McCoy and Cha [162], and this was used already by Melton [63] and later also by Hofeldt [158] and Snelling et al. [118]. The heat conduction rate can be written as

$$\dot{Q}_{\mathrm{cond,MC}} = \frac{2k_g(T - T_g)\pi D_{\mathrm{HC}}^2}{(D_{\mathrm{HC}} + G\lambda_g)} , \tag{5.11}$$

where G is given as

$$G = \frac{8f}{\alpha(\gamma + 1)} , \tag{5.12}$$

in which f is the Eucken correction to the thermal conductivity of polyatomic gases given as [38]

$$f = \frac{9\gamma - 5}{4} , \tag{5.13}$$

where the heat capacity ratio γ can be written as

$$\gamma = \frac{C_p}{C_p - R} . \tag{5.14}$$

The McCoy and Cha model is fairly straightforward to implement since it is written in closed form and thus may be used directly inside the energy balance equation. It is derived for the transition regime and is thereby capable of predicting heat conduction also in high-pressure situations. However, as discussed by Liu et al. [125], it has been derived using the assumption that the ratio between the particle temperature and gas temperature is relatively close to unity, and this is not the case for situations typically encountered during LII – especially for measurements in room temperature soot where this ratio can be ~12. Additionally, the McCoy and Cha model can not be used with the aggregation model outlined in this chapter, since this has been derived for the continuum regime [121]. The McCoy and Cha model was used to derive the results presented in Paper I and II.

A more sophisticated theory without these limitations is the so called Fuchs interpolation method, which was first presented by Fuchs (See for instance [163]), and later proposed for LII applications by Filippov and Rosner [123] and recently also Liu et al. [125]. It is based on the introduction of a limiting sphere a distance δ from the particle surface as depicted in Fig. 5.3. A temperature T_δ is defined
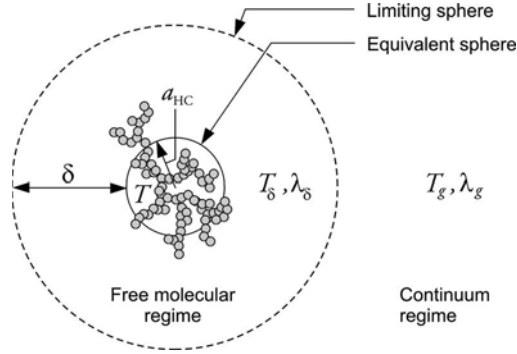
Figure 5.3 Schematic representation of the Fuchs heat conduction model applied for a soot aggregate.

inside of the sphere and outside, the temperature is held constant at the specified gas temperature T_g. Note that the radius of the equivalent heat conduction sphere, a_{HC}, is used when describing the Fuchs model. Inside this limiting sphere, heat conduction is modelled using the free molecular regime expression

$$\dot{Q}_{cond,FM} = \frac{1}{2}\alpha \pi a_{HC}^2 p \sqrt{\frac{8 k_B T_\delta}{\pi m_g}} \frac{\gamma^* + 1}{\gamma^* - 1}\left(\frac{T}{T_\delta} - 1\right),$$ (5.15)

where the mean heat capacity ratio γ^* is defined according to

$$\frac{1}{\gamma^* - 1} = \frac{1}{T - T_\delta}\int_{T_\delta}^{T}\frac{dT}{\gamma - 1}.$$ (5.16)

The heat conduction outside of the sphere is modelled using the continuum regime expression

$$\dot{Q}_{cond,C} = 4\pi\left(a_{HC} + \delta\right)\int_{T_g}^{T_\delta}k_g dT.$$ (5.17)

Since no heat sources exist outside of the particle, the heat conduction must necessarily take the same value at the boundary of the limiting sphere independent on which of the two theories that are used. An equation can therefore be set up where the two heat conduction expressions are set equal to each other at this boundary. The limiting sphere radius can be related to the particle radius following

$$\frac{\delta + a_{HC}}{a_{HC}} = \frac{a_{HC}^2}{\lambda_\delta^2}\left(\frac{1}{5}\Lambda_1^5 - \frac{1}{3}\Lambda_2\Lambda_1^3 + \frac{2}{15}\Lambda_2^{5/2}\right),$$ (5.18)

where the mean free path inside the sphere, λ_δ, relates to the mean free path outside of the sphere (See Eq. 5.8), according to

$$\lambda_\delta = \frac{k_g(T_\delta)}{k_g(T_g)} \sqrt{\frac{T_\delta}{T_g}} \left(\frac{\gamma(T_\delta)-1}{\gamma(T_g)-1} \right) \frac{f(T_g)}{f(T_\delta)} \lambda_g \,, \tag{5.19}$$

where it has been assumed that the pressure difference between the two regions divided by the limiting sphere is negligible [123]. The functions within the brackets in Eq. 5.18 can be expressed as

$$\begin{cases} \Lambda_1 = 1 + \lambda_\delta / a_{HC} \\ \Lambda_2 = 1 + (\lambda_\delta / a_{HC})^2 \end{cases} . \tag{5.20}$$

A system of nonlinear equations can now be set up where the first equation is the one originating from Eq. 5.15 and 5.17 when put equal, and the second one Eq. 5.18. The variables δ and T_δ can then be derived for a given particle temperature T, ambient gas temperature T_g and pressure p and equivalent heat conduction radius a_{HC} by solving this nonlinear equation system. Using the derived variables as input, the heat conduction rate can then be calculated using either the free molecular (5.15) or the continuum regime expression (5.17). Contrary to the McCoy and Cha model, the Fuchs model can not be used directly in the heat balance equation. The problem must be solved in advance using numerical methods, and is therefore a separate part of the complete LII model package described in this chapter. This is further discussed in Chapter 5.4.

Since free molecular regime conditions are predicted within the limiting sphere in the Fuchs model, the aggregation model and scaling parameters defined in Eq. 5.10 can be used [121]. This treatment has been used for the results presented in Paper IV. It may be noted that the Fuchs model was used also within the work presented in Paper III, but in this work, a simplified aggregation model was used for the equivalent sphere diameter based on the aggregate projected area as outlined by Snelling et al. [164].

5.2.1.4 Sublimation

As the soot particles approach temperatures around 4000 K, the energy loss by sublimation of parts of the matter into various gaseous species will become important. Apart from contributing to the energy loss, sublimation also induces mass loss from the particles. The sublimation process is one of the most difficult to model accurately, and this constitutes one of the reasons of working in the low-fluence regime when performing particle size measurements, as discussed in Chapter 3.2.2.

The sublimation model used within this thesis is based on the one given by Snelling et al. [118] and Smallwood et al. [124] and can be traced back to Hofeldt [158], Melton [63], Dasch [165] and Eckbreth [62]. Considering first only one single primary particle, the energy loss due to sublimation can be written as

$$\dot{Q}_{s,sub} = -\frac{\Delta H_v}{M_v} \frac{dM}{dt}, \tag{5.21}$$

where the heat of sublimation, ΔH_v, and the molecular weight of soot vapour, M_v, are temperature-dependent functions. The mass rate can be written as

$$\frac{dM}{dt} = -\pi D^2 N_v \frac{M_v}{N_A}, \tag{5.22}$$

where the molecular flux of sublimated carbon, N_v, can be expressed for the transition regime by using a harmonic mean formulation [118,158],

$$N_v = \left(\frac{1}{N_C} + \frac{1}{N_{FM}} \right)^{-1}. \tag{5.23}$$

The expression for the free molecular regime is given according to [124,166]

$$N_{FM} = \beta n_v \sqrt{\frac{RT}{2\pi M_v}}, \tag{5.24}$$

and the continuum regime expression [118,158]

$$N_C = 2n_v \frac{\Gamma_{diff}}{D}, \tag{5.25}$$

where Γ_{diff} is the diffusion coefficient defined as [38]

$$\Gamma_{diff} = \frac{f k_B T}{4\sigma p} \sqrt{\frac{RT}{\pi M_v}}. \tag{5.26}$$

Using the ideal gas equation the molecule number density of soot vapour can be written as

$$n_v = \frac{P_v N_A}{RT}. \tag{5.27}$$

This makes it possible to write the mass rate according to

$$\frac{dM}{dt} = -\pi D^2 P_v \sqrt{\frac{M_v}{2\pi RT}} \left[\frac{\sqrt{2} D\sigma p}{f k_B T} + \frac{1}{\beta} \right]^{-1} . \qquad (5.28)$$

For atmospheric pressure applications the first term within the brackets may be neglected resulting in the simplified free molecular expression

$$\frac{dM}{dt} = -\pi D^2 P_v \beta \sqrt{\frac{M_v}{2\pi RT}} , \qquad (5.29)$$

which is the one given by Smallwood et al. [124].

As the sublimation process is dependent on the surface area of the particle, it is reasonable to assume that aggregation will influence the process. However, to the author's knowledge no thorough study has been presented where the influence of aggregation on the sublimation mechanism has been investigated. In the work by Snelling et al. [20], who used the same sublimation model described in this chapter, an equivalent sphere diameter was used both within the heat conduction and the sublimation models, but only for the continuum regime, predicting essentially no influence of aggregation on LII applied in the free molecular regime. Later publications from the same group [120,121,164] account for aggregation in both the free molecular and continuum regimes, but presents work at low-fluence conditions and do not account for the sublimation process. As the current status of this issue seems unclear, the heat loss rate due to sublimation has in the current model been approximated by the sum of the heat loss rates from individual primary particles according to

$$\dot{Q}_{\text{sub}} = -N_p \frac{\Delta H_v}{M_v} \frac{dM}{dt} , \qquad (5.30)$$

where the mass loss rate is modelled using Eq. 5.28 as for isolated particles. This treatment will be expected to slightly overpredict the influence of the sublimation mechanism on the LII signal from aggregated particles.

5.2.1.5 Radiation

Radiation in the visible and infrared spectral region represents the last of the energy loss mechanisms. This process is responsible for producing the signal detected with the LII technique and hence plays a crucial role. The energy loss rate due to radiation is, however, not large compared to the previously described loss mechanisms, and the term can often be omitted when solving the equations. The RDG-PFA theory discussed in Chapter 5.2.1.2 enables the radiation from a soot aggregate to be modelled as the sum of the radiation from individual primary particles according to [119]

$$\dot{Q}_{\mathrm{rad}} = \pi D^2 N_p \int\limits_0^\infty \varepsilon(D,\lambda) M_\lambda^b(T,\lambda) d\lambda \, , \tag{5.31}$$

where the Planck radiation law is given as

$$M_\lambda^b(T,\lambda) = \frac{2\pi hc^2}{\lambda^5 (e^{hc/\lambda k_B T} - 1)} \, , \tag{5.32}$$

and the emissivity in the Rayleigh limit [38]

$$\varepsilon(D,\lambda) = \frac{4\pi D E(m)}{\lambda} \, . \tag{5.33}$$

The semi-infinite integration interval in Eq. 5.31 is complicated by the fact that no explicit analytical solution exist. The integral can, however, be expressed using the Gamma and Zeta functions, Γ and ζ, according to

$$\int\limits_0^\infty \frac{1}{\lambda^u (e^{hc/\lambda k_B T} - 1)} d\lambda = \left(\frac{k_B T}{hc} \right)^{u-1} \zeta(u-1)\Gamma(u-1) . \tag{5.34}$$

Using this relation for the present application where $u = 6$ yields

$$\dot{Q}_{\mathrm{rad}} = \pi D^2 N_p \int\limits_0^\infty \frac{4\pi D E(m)}{\lambda} \frac{2\pi hc^2}{\lambda^5 (e^{hc/\lambda k_B T} - 1)} d\lambda =$$

$$= 8\pi^3 D^3 N_p hc^2 E(m) \left(\frac{k_B T}{hc} \right)^5 \zeta(5)\Gamma(5) \approx \frac{199\pi^3 D^3 N_p (k_B T)^5 E(m)}{h(hc)^3} . \tag{5.35}$$

Here the fact that $\zeta(5) \approx 1.0369$ and $\Gamma(5) = 24$ has been used.

5.2.1.6 Internal energy storage

The last of the processes represents the rate of energy transfer to and from the soot material itself by the other processes in terms of internal energy storage. The total internal energy of one spherical soot particle can be written as

$$Q_{s,\mathrm{int}} = M c_s T = \frac{\pi}{6} D^3 \rho_s c_s T \, . \tag{5.36}$$

The energy rate has traditionally been expressed as [38,63,158]

$$\dot{Q}_{s,\mathrm{int}} = \frac{\pi}{6} D^3 \rho_s c_s \frac{dT}{dt} \, . \tag{5.37}$$

There is currently a discussion within the community of LII model research whether this term is correct to use with temperature-dependent functions for the density and specific heat [167], as indeed is done in this thesis. Mathematically there is reason to assume that the time derivative should be applied to all three temperature-dependent functions in Eq. 5.36 resulting in an expression of the energy rate with three terms. Awaiting convincing evidence of which treatment is the correct to use for LII, the current model utilizes Eq. 5.37.

Aggregation is assumed not to affect the rate of internal energy change, and the energy balance for an aggregate will be written as the sum of the individual primary particle contributions as

$$\dot{Q}_{\text{int}} = \frac{\pi}{6} D^3 N_p \rho_s c_s \frac{dT}{dt} \,. \qquad (5.38)$$

This assumption is expected to hold during the absorption phase, as the primary particles are assumed to be heated to essentially the same maximum temperature for aggregates within the RDG-PFA approximation. However, as discussed already in Chapter 5.2.1.3, the temperature may turn non-uniform as different parts of the aggregate cools with somewhat different rates, thus violating the simplified treatment in Eq. 5.38. Here it might be speculated that, for dense structures within the aggregate, such temperature inhomogeneities may give rise to internal energy transfer, which may have to be modelled in order to accurately predict the aggregate temperature distribution. Internal energy transfer is predicted to have negligible influence on the LII process when using nanosecond pulses on isolated primary particles in the Rayleigh limit [38,165], but may very well be important for aggregates.

5.2.2 The heat and mass balance equations

The physical processes described in the last section may now be used to set up balance equations for the energy and mass rates during the LII process. The energy balance can be written as

$$\dot{Q}_{\text{abs}} - \dot{Q}_{\text{cond}} - \dot{Q}_{\text{sub}} - \dot{Q}_{\text{rad}} - \dot{Q}_{\text{int}} = 0 \,. \qquad (5.39)$$

The mass of one spherical particle can be written as

$$M = \frac{\pi}{6} \rho_s D^3 \,. \qquad (5.40)$$

The mass rate will thus be [158]

$$\frac{dM}{dt} = \frac{\pi}{2} \rho_s D^2 \frac{dD}{dt} + \frac{\pi}{6} D^3 \frac{d\rho_s}{dT} \frac{dT}{dt} \,, \qquad (5.41)$$

which can be rewritten in terms of the particle diameter change according to

$$\frac{dD}{dt} = \frac{2}{\pi \rho_s D^2}\left[\frac{dM}{dt} - \frac{\pi}{6}D^3\frac{d\rho_s}{dT}\frac{dT}{dt}\right].$$ (5.42)

Finally, a system of equations can be set up as

$$\begin{cases} \dfrac{dT}{dt} = \dfrac{6}{\pi D^3 N_p \rho_s c_s}\left[\dot{Q}_{abs} - \dot{Q}_{cond} - \dot{Q}_{sub} - \dot{Q}_{rad}\right] \\[3mm] \dfrac{dD}{dt} = \dfrac{2}{\pi \rho_s D^2}\left[\dfrac{dM}{dt} - \dfrac{\pi}{6}D^3\dfrac{d\rho_s}{dT}\dfrac{dT}{dt}\right] \end{cases},$$ (5.43)

where the mass rate is given by Eq. 5.28. Solving this system of equations results in the temperature $T(t)$ and particle diameter $D(t)$ for the soot particle.

5.2.3 The LII signal

With knowledge of the particle temperature and diameter history, the LII signal may be calculated using the Planck radiation law adjusted with the emissivity of soot particles. The expression for the time-resolved LII signal from a soot aggregate within the RDG-PFA approximation can be written as [38]

$$S_{LII} \propto \pi D^2 N_p \int_0^\infty R(\lambda')\varepsilon(D,\lambda')\frac{2\pi hc^2}{\lambda'^5}\left(\frac{1}{e^{hc/\lambda'k_B T}-1} - \frac{1}{e^{hc/\lambda'k_B T_g}-1}\right)d\lambda',$$ (5.44)

in which the radiation level present when the soot particles are unperturbed by the laser and are at thermal equilibrium with the ambient gas has been subtracted. The emissivity $\varepsilon(D,\lambda)$ of the soot particles in the Rayleigh regime is given by Eq. 5.33.

5.3 Extension of the model for practical applications

The heat and mass transfer model presented in chapter 5.2 is only capable of predicting the signal from one single soot particle or soot aggregate of predefined size exposed to one predefined laser fluence value. In real combustion systems the soot in the measurement volume has a size distribution and different particles are exposed to different laser fluences due to a non-uniform spatial profile of the laser energy. An extension of the heat and mass transfer model that takes these factors into account will be described in this chapter.

5.3.1 The primary particle size distribution

One common description of primary soot particle sizes in flames is that they follow a log-normal distribution [168,169]. Such a distribution function can be written as [26]

$$P_{\text{PPS,LN}}(D) = \frac{1}{D\sqrt{2\pi}\ln\sigma_g} \exp\left(-\frac{(\ln D - \ln D_g)^2}{2(\ln\sigma_g)^2}\right), \qquad (5.45)$$

where D_g is the geometric mean diameter and σ_g the geometric standard deviation. Others have found that a plain Gaussian distribution function can describe their data [13,26]. The distribution function will then be given as

$$P_{\text{PPS,G}}(D) = \frac{1}{D_{\text{FWHM}}} \sqrt{\frac{4\ln 2}{\pi}} \exp\left(-4\ln 2\left(\frac{D - D_{\text{av}}}{D_{\text{FWHM}}}\right)^2\right), \qquad (5.46)$$

where D_{av} is the mean diameter and D_{FWFM} is the full with at half maximum of the distribution. These distribution functions were used for the results presented in Paper I. In addition to these analytical distribution functions, the extended model can also predict the response from an arbitrarily shaped distribution for instance from measurement data.

In the extension of the model, the heat and mass balance is solved for a discrete number of primary particle sizes covering the predefined distribution. The weighted sub signals are later summed to produce the total signal. This can be written as

$$S_{\text{LII,polydisperse}}(t) = \sum_{i=1}^{n} S_{\text{LII}}(D_i, t) P_{\text{PPS}}(D_i)\Delta D, \qquad (5.47)$$

where ΔD is the (equidistant) spacing between consecutive primary particle diameters D_i during summation and n denotes the total number of diameters for which the LII signal is calculated.

5.3.2 The spatial distribution of laser energy

The response from particles exposed to a non-uniform spatial profile of the laser is modelled using the same approach as outlined in section 5.3.1 for the particle sizes. However, here not only the distribution of fluence values occurring within the laser profile is needed, but also the relative occurrence of a certain fluence level. The extended model uses two alternative approaches for dealing with this: The direct mode that is applied for simple distributions, and the indirect mode that is applied to more complex ones.

Figure 5.4 shows the three types of theoretical profiles, the *top-hat*, the *Gaussian sheet* and the *Gaussian beam*. For these relatively simple distributions of laser energy, the extended model operates in *direct mode*.
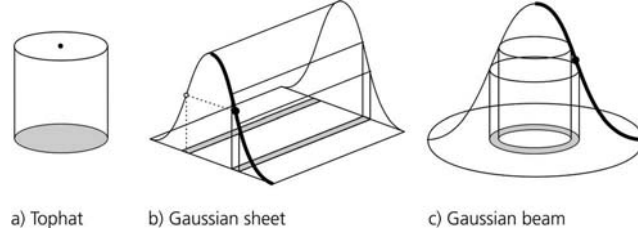

a) Tophat   b) Gaussian sheet   c) Gaussian beam

Figure 5.4 *The three standard spatial distributions of laser energy. The grey areas mark the relative occurrence of the laser fluence value centred over them.*

The LII signal obtained using an ideal top-hat profile is equal to solving the heat and mass balance using a single fluence value. For the Gaussian sheet and Gaussian beam, the heat and mass balance is solved for a discrete number of fluence values defined by the laser pulse energy multiplied with the one-dimensional Gaussian distribution functions

$$\begin{cases} P_{\text{F,GS}} = \dfrac{1}{wh_s}\sqrt{\dfrac{2}{\pi}}\exp\left(-2\left(\dfrac{r}{w}\right)^2\right) \\[2ex] P_{\text{F,GB}} = \dfrac{2}{\pi w^2}\exp\left(-2\left(\dfrac{r}{w}\right)^2\right) \end{cases}, \tag{5.48}$$

where w denotes the $1/e^2$ radius of the Gaussian function, r the distance from the centre of the Gaussian and h_s the height of the Gaussian sheet. The resulting LII sub signals are later added according to their relative occurrence in the measurement volume. The scheme may be written as

$$S_{\text{LII,nonuniform}}(t) = \sum_{j=1}^{n} S_{\text{LII}}(P_{\text{F}}(r_i)\cdot E,t)A_{\text{F}}(r_i), \tag{5.49}$$

where P_{F} is one of the Gaussian distribution functions given in Eq. 5.48, E the laser pulse energy, r the distance from the centre of the distribution function, A_{F} the relative weights of the respective LII sub signal and n the total number of fluence levels along the Gaussian distribution function for which the LII signal is calculated. The relative weights are determined as the ratio between the cross section area exposed to a particular fluence (grey areas in Fig. 5.4b and c) and the total cross section area. This approach was used in Paper I and IV.

In addition to the scheme outlined above, the extended model is capable of predicting the signal response from an arbitrarily defined distribution of laser

55

energy. This includes variation of the width and height of the spatial profile as function of the position along the laser beam propagation direction, which enables predictions of the LII signal behaviour is measurement volumes where the beam is focused or divergent. Contrary to the direct mode operation, the spatial profile (cross section) may here be directly given to the model as a fluence matrix. This makes it possible to input experimentally measured spatial profiles obtained using a beam profiler CCD camera. The use of such complex distributions of laser energy will result in a three-dimensional fluence distribution tensor $\mathbf{F}_{ijk}$ defining the local laser fluence in a mesh covering the whole measurement volume. Since most fluence values necessarily must occur on many positions within the measurement volume, the heat and mass balance must not be solved for every spatial position (direct mode operation). Instead the model operates in *indirect mode*, along the scheme visualized in Fig. 5.5.

The spatial distribution of laser energy, both perpendicular to (cross section) and parallel to (propagation) the laser beam, is given as input to the model. These distribution functions are used to create a mesh of local laser fluence values covering the measurement volume. The fluence values may be described as a tensor $\mathbf{F}_{ijk}$. During a first step, a fluence vector $\mathbf{F}$ with predefined number of elements
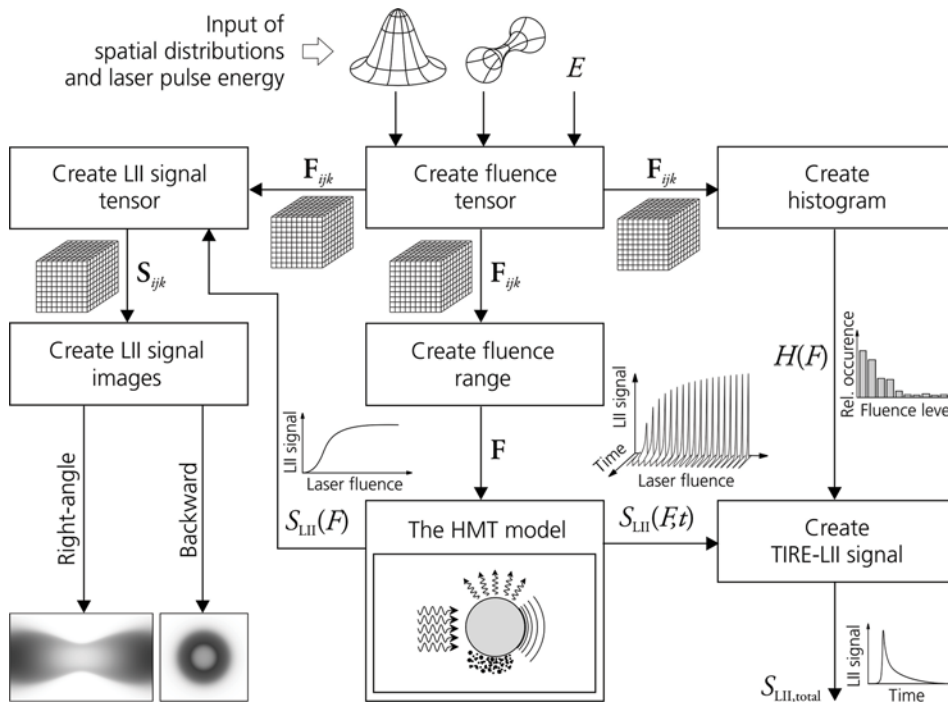

Figure 5.5 *The work flow of the extended model when creating an LII signal response from measurement volumes with arbitrarily defined spatial distributions of laser energy.*

56

determined by the requested resolution is created covering the whole range of fluence values that are to be found within the tensor $\mathbf{F}_{ijk}$, i.e.

$$\mathbf{F} = \{\min(\mathbf{F}_{ijk}),...,\max(\mathbf{F}_{ijk})\} . \tag{5.50}$$

The heat and mass transfer model is then used to calculate the LII signal response for all fluence values in $\mathbf{F}$. Here the program operates differently dependent on the choice of output from the model.

In the right part of Fig. 5.5 the scheme used when creating predictions of the total time-resolved signal from the measurement volume is shown. The heat and mass transfer model is used to create time-resolved LII signals for all fluence values in the fluence vector $\mathbf{F}$ resulting in the signal function $S_{\text{LII}}(F,t)$. A histogram, $H(F)$, defining the relative occurrence of individual fluence levels is created from the fluence tensor $\mathbf{F}_{ijk}$ and this histogram is used to weight the individual LII signals obtained at different fluence levels according to

$$S_{\text{LII,total}}(t) = \sum_{i=1}^{n} H(F_i)S_{\text{LII}}(F_i,t) , \tag{5.51}$$

where n denotes the total number of elements in $\mathbf{F}$.

For predictions of LII signal images, the scheme depicted in the left part of Fig. 5.5 is used. Following the same principle outlined for the time-resolved signal, the heat and mass transfer model is used to create LII signals for all fluence values in the fluence vector $\mathbf{F}$, but this time not time-resolved, but instead time-integrated over a predefined time interval corresponding to a detector gate window. This results in the signal function $S_{\text{LII}}(F)$, which experimentally corresponds to a fluence curve for an ideal top-hat profile. A signal intensity tensor $\mathbf{S}_{ijk}$ can then be calculated according to

$$\mathbf{S}_{ijk} = S_{\text{LII}}(\mathbf{F}_{ijk}) . \tag{5.52}$$

The elements in the LII signal tensor may later be summed along the detection path of choice to obtain the predicted LII signal image.

As initially stated, this approach enables predictions of LII signals from arbitrarily shaped measurement volumes. However, a number of assumptions underlie this approach. It is assumed that the spatial profile of the laser (cross section) does not change its relative shape along the beam propagation direction meaning that only its width and height changes. For the fluence tensor to be correctly representing a real situation it must be assumed that absorption of laser radiation along the beam propagation direction is negligible. Also absorption of the LII signal on its way to the detector (signal trapping) is neglected in the present model. Finally the creation of the LII signal images is carried out assuming a depth of field of the imaging system much larger than the measurement volume, making all parts of the volume sharply imaged. Additionally, the detection cone angle and

the length of the measurement volume are both assumed small enough for the incoming radiation to be treated as being parallel, enabling a straightforward summation of the signal intensities in the tensor along the optical axis of the imaging system. The scheme outlined here has been used in paper II.

5.4   Implementation of the model in MATLAB®

The complete model package described in this chapter is implemented in Mathworks' MATLAB® software (Version 6.5). The main structure of the model implementation is illustrated in Fig. 5.6. The main executable *TIRE_LII_model* calls upon a file *LII_parameters* in which the user defines the input data. This includes physical and experimental parameters as well as variables defining program settings. This file calls upon *LII_definitions*, which completes the input parameter definitions using the input data from *LII_parameters*. In this file all distribution functions are either defined or read from file. The last section of *LII_definitions* defines string variables containing all sub-models within the heat and mass transfer equations (See Eq. 5.43) and automatically generates the file *HMTequations*, which is a MATLAB® function containing the heat and mass balance equations. This scheme enables the user to choose different sub-models, for instance for heat conduction and aggregation, without having to use multiple files containing different versions of the equations. Another advantage with defining all possible subroutines in *LII_definitions* is that the individual sub-models are defined outside
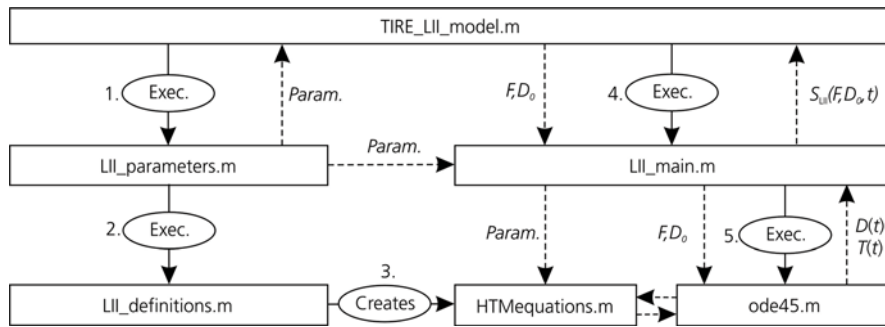
Figure 5.6 *The implementation scheme in MATLAB® for the LII model. The solid arrows indicate the order of file execution and creation, whereas the dotted lines indicate input and output of data. Some variables have been given explicitly to highlight the main task of each routine. These include the laser fluence F, the initial primary particle diameter D_0, the LII signal S_{LII} and the time-dependent particle temperature and diameter T and D. The rest of the parameters are implicitly marked as 'Param'. Some additional subroutines have here been omitted. Apart from a large set of built-in MATLAB® functions, these include implementations of temperature-dependent functions describing physical quantities like for instance the heat capacity $C_p(T)$.*

58

of the equation system. This makes it possible to calculate the individual terms as function of time after having solved the equation system, something that is performed within the main executable *TIRE_LII_model*. This has to be performed after the heat and mass balance has been solved since the individual terms are functions of both the particle temperature $T(t)$ and the particle diameter $D(t)$ and thus can not be calculated without these functions known.

After this initiation phase, the main executable *TIRE_LII_model* calls upon a subroutine called *LII_main*, which is responsible for (1) solving the heat and mass balance and (2) for calculating the LII signal using the predefined spectral detection characteristics. *LII_main* uses the MATLAB® built-in solvers *ode45*, which is based on an explicit formula using a combination of fourth and fifth order Runge-Kutta calculations, or for stiff problems (usually at high fluence) *ode15s*, which is a variable-order solver based on the numerical differentiation formulas. For more information on the solvers see [170-172]. This solves the equations defined in *HMTequations*. *LII_main* only outputs one calculated LII signal for one soot particle. The features of the extended model discussed in Chapter 5.3 are all implemented in *TIRE_LII_model*, which calls upon *LII_main* the number of times needed for the specified task and later creates the weighted signals by using the distribution functions.

As previously mentioned, the Fuchs heat conduction model is implemented as a separate part of the complete model and must be solved prior to using the model for LII. Also the Fuchs model has been implemented in MATLAB® and do in its present form utilize the built-in solver *fsolve*, which implements the trust-region dog-leg method (See [171] and references therein), to calculate the temperature and dimensions of the limiting sphere (See Chapter 5.2.1.3). Reaching convergence is difficult especially at high pressures, low gas temperatures and large heat conduction equivalent diameters. This tends to create problems for *fsolve*, which usually do not reach a solution no matter which initial values that are given. To circumvent this problem a minimization routine *devec3* based on so called differential evolution developed by Price and Storn [173] is used prior to calling *fsolve*. The results obtained from this routine are expected to be very close to the solution, and, when given as initial values for *fsolve*, a solution is readily found. For the LII model to be able to use the Fuchs model, calculations of the heat conduction rate must be carried out both for varying particle temperature and equivalent heat conduction radius. The heat conduction rates are calculated for a predefined range of values of these parameters and is later stored in a two-dimensional matrix, $\dot{Q}_{\text{Conduction}}(T, a_{HC})$, which is written to file. This file is later input to the LII model, which extracts the requested heat conduction rates from the matrix using an interpolation scheme. This may introduce errors in evaluated results if the resolution of especially the particle size vector, defining the range of values solved for, is not sufficiently high. When deriving the results presented in Paper IV concerning the relationship between LII signal and primary particle size, it was found that a resolution of 1 nm was sufficient to ensure accurate results.

Chapter 6

Results

This chapter will summarize the results obtained within the frame of the thesis. The outline will start with some theoretical results obtained using the model for LII, go on with describing a theoretical and experimental comparison of spatially resolved LII signals, and finally discuss in-cylinder engine measurements.

6.1 Theoretical predictions using the model for LII

A number of theoretical investigations have been carried out within the work presented in the thesis. In this chapter some of the major results from the papers will be discussed together with selected unpublished material.

6.1.1 Influence of the primary particle size distribution

As previously discussed in Chapter 3.2.2, the LII signal decay is dependent on the particle size. Measurements in real systems are complicated by the fact that particles of different sizes coexist in the measurement volume. The total LII signal from all these particles depend on the size distribution and recent work has focused on the methodology to extract size distribution data from single LII signal decays. However, this is not straightforward and also requires knowledge of the size distribution function. A simplified approach is to assume a monodisperse distribution within the measurement volume. In this case all particles have the same size making interpretation using the model relatively straight-forward. This approach suffers from one major drawback. Larger particles incandesce much stronger than the smaller ones due to the approximate volume-dependence on the signal. In any polydisperse system, the particles larger than the mean particle size will contribute much more strongly to the resulting LII signal decay shape than the smaller ones. This means that if the assumption of a monodisperse distribution is made for systems which in reality are polydisperse, the evaluated particle size obtained by a best fit between measurements and monodisperse model results, will
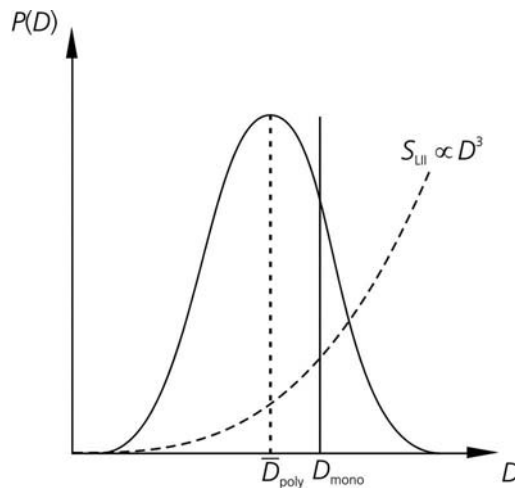
Figure 6.1 *Graphical representation showing the overestimation of the average particle size evaluated from LII signal decays that occurs when assuming a monodisperse distribution. The approximate volume-dependence of the LII signal, which is the main reason for this overprediction, is indicated by the dotted line.*

be larger than the average particle size within the distribution. This is graphically demonstrated in Fig. 6.1.

The relative error introduced to measurements due to this effect has been investigated in Paper I in which the heat and mass transfer model for LII was used to derive time-resolved LII signals for both monodisperse and polydisperse distribution functions. The settings for the calculations are given in Paper I and only a brief summary is given here. For the modelling, a Gaussian temporal profile and a top-hat spatial profile were used at a wavelength of 532 nm and a laser fluence low enough not to cause sublimation. Detection was at 400 nm and the signal was calculated for 600 ns starting just before the laser pulse. The comparison between signals was made using a least-square approach of the LII signal decay curves when normalised at a time after the prompt signal where heat conduction was the dominating mechanism. The particle size distribution was modelled as a Gaussian function with a full width at half maximum, D_{FWHM}, given as fractions of the average diameter, D_{av}. The result is shown in Fig. 6.2. Previous studies have shown that particle size distribution may be assumed Gaussian with a standard deviation 17-25% of the average size [26]. This would correspond to a full width at half maximum of 40-60% of D_{av} for a Gaussian. The shape of the distribution function is naturally influencing the errors. When using lognormal particle size distributions with the same standard deviation and average diameter as the Gaussian distribution, the errors were slightly increased (order of a few nanometres).
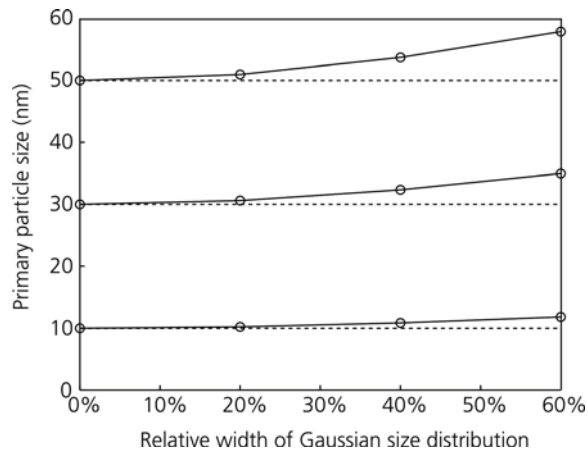
Figure 6.2 *Theoretical predictions of the evaluated particle size from a polydisperse system with constant average particle size and varying width of a Gaussian distribution function when assuming the system to be monodisperse during the particle size evaluation.*

It must be kept in mind that the error may be defined differently depending on the parameter it is related to. In the case of a Gaussian function, which is uniform, the most probable size of the particles (the distribution maximum) will occur at the average value. Therefore it will be natural to define the error with respect to this parameter. For a lognormal distribution, which is skewed, the most probable size will occur at smaller diameters than the average diameter. The statement given above regarding the errors for a lognormal distribution is valid for errors defined with respect to the average value, not the most probable size.

6.1.2 Influence of the spatial distribution of laser energy

The influence of the spatial distribution of the laser energy on the LII signal has been investigated in several independent studies within the frame of the thesis, and some of these studies will be discussed in this chapter. The influence of the spatial profile also appears in Chapter 6.2 where theoretical and experimental comparisons of spatially resolved LII signals are presented.

As discussed in Chapter 3.2.2 the spatial profile of the laser has a large impact on the fluence dependence of the gated (time-integrated) LII signal, the so called fluence curve. Previous theoretical investigations have been presented for the top-hat and Gaussian sheet profiles [94,118] and indeed also for a Gaussian beam profile [174], but to the author's knowledge no comparative study with all three profiles has previously been presented. This was the purpose of the results presented in Paper I, where the relative shape of the fluence curve has been compared as function of spatial profile, detection gate and delay, and primary particle size. Figure 6.3 shows modelled fluence curves for three different spatial distributions of the laser energy. The curves are plotted as function of the peak

fluence, which means that all curves, when compared at a specific fluence level, will have reached the same degree of sublimation at some location in the measurement volume. Apart from the top-hat profile the result is shown for two Gaussian distribution functions. The *Gaussian sheet* has a top-hat distribution function along one dimension and a Gaussian along the other and is an ideal representation of the spatial profile in the focus of a laser sheet used for imaging measurements. The *Gaussian beam* is a circular-symmetric Gaussian distribution and is the ideal representation of the spatial profile in either the unfocused or focused laser beam configuration used for point measurements.

The results shown in Fig. 6.3a clearly demonstrates the significance of the spatial profile for the fluence dependence. The particle size effect is relatively small, the highest influence being for the top-hat profile. In Fig. 6.3b the normalised fluence curves are shown for a top-hat profile and 10 nm particles with varying delay time. The shape of the curve drastically changes between 0 and 20 ns delay time, indicating that the fluence dependence of the prompt and delayed signals are quite different in nature. This behaviour has its origin in the sublimation process, which predicts a particle size reduction with increasing fluence. This reduction will occur during the pulse, essentially decreasing the soot matter available to radiate at late times.

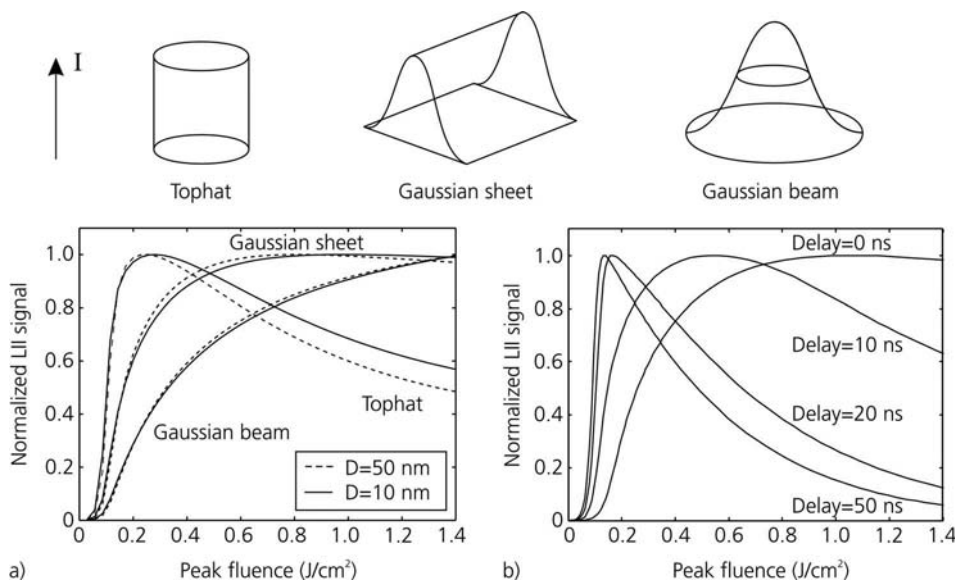**Figure 6.3** *Theoretical predictions of the fluence dependence of the laser-induced incandescence signal for 532 nm excitation and detection at 400 nm. In a) the result is shown for the three modelled spatial profiles of laser energy using a prompt 100 ns gate and in b) the result is shown for an 18 ns gate and a particle size of 10 nm with varying delay time using a top-hat profile. From Paper I.*

In the results described above, the spatial profile was considered constant as function of distance along the beam propagation direction. This assumption can not always be made. When performing measurements using a focused beam in the exhausts from a jet engine detecting the signal from the rear (backward configuration) [104], the line-of-sight configuration will inevitable lead to the signal collection being dependent also on the variation of the beam thickness as function of distance from the laser. As an example of the effects obtained, some unpublished results derived for laboratory flame conditions will be presented. In Fig. 6.4 the right-angle and backward LII signals obtained from the measurement volume of a 6 cm long soot field with uniform volume fraction and particle size is shown as function of laser fluence and gate timing.
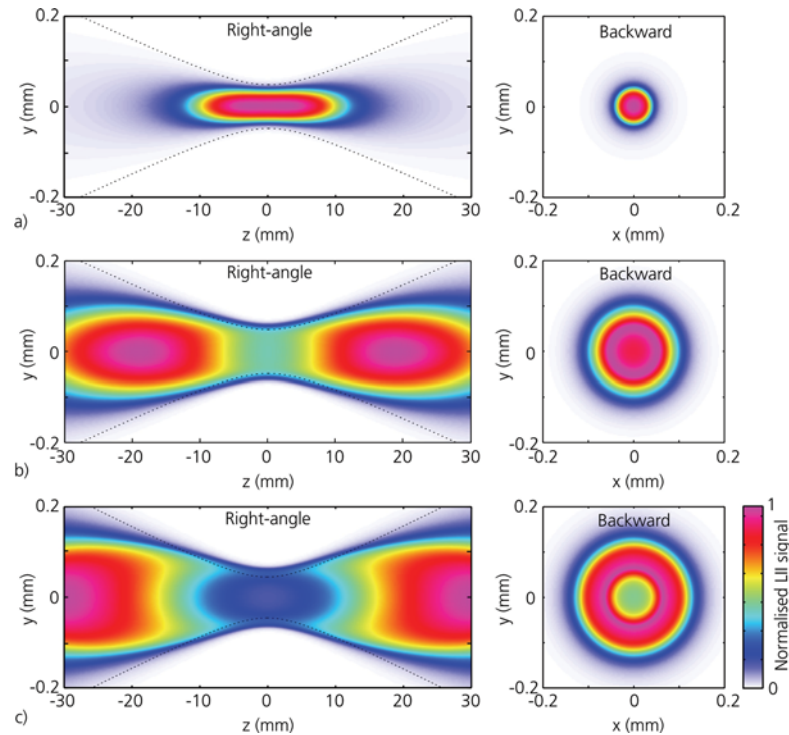
***Figure 6.4** Modelled LII signal images for a perfectly homogeneous soot distribution when using a laser with Gaussian spatial profile focused using a spherical lens. The ambient gas temperature is 1800 K and pressure 0.1 MPa. The temporal profile of the laser pulse is Gaussian with a FWHM at 9 ns and the laser wavelength is 1064 nm. The primary particle size is 20 nm and detection is at 700 nm. In a) the gate is 20 ns centred on the laser pulse, and the maximum local laser fluence is ~0.55 J/cm². The case shown in b) is derived using the same detection timing as in a) but at a higher fluence. The maximum fluence in the measurement volume is ~4 J/cm². In c) the high-fluence case from b) is shown for the 20 ns gate delayed 100 ns with respect to the position in b). All images have been individually normalised and no comparison of absolute levels between them are intended.*

65

The focused configuration is the result from an ideal Gaussian beam propagation using a parallel laser beam with 7 mm $1/e^2$ diameter focused by a 500 mm lens at 1064 nm. The results clearly show how important the nonlinear dependence on local laser fluence is for the LII signal. In Fig. 6.4a the result is shown for a pulse energy of 0.02 mJ. The maximum laser fluence occurring at the centre of the measurement volume will be ~0.55 J/cm². At this pulse energy, the strong divergence of the beam is enough to reduce the local laser fluence in the periphery to levels at which the LII signal is greatly reduced, effectively creating a measurement volume located in the vicinity of the beam waist. For the higher pulse energy used in Fig. 6.4b and c (0.15 mJ), the local fluence levels are high enough to create LII signal in the periphery but at the same time the signal decreases at the beam waist, predominately in the centre of the beam. This signal decrease results from the strong sublimation process in these regions, and the effect is most clearly seen in the case of delayed detection used in Fig. 6.4c.

6.1.3 Influence of the ambient gas temperature and pressure

As discussed in chapter 3.2.2, quantitative measurements of the soot volume fraction can be obtained by relating the signals measured in an unknown sooting environment to those obtained using the same experimental setup in a calibration source with known soot volume fraction. This methodology is based on complete knowledge of the exact relationship existing between the signals generated in the two systems, information which generally is not available. Assumptions are therefore made. First of all it must be assumed that the relationship between the LII signal and the soot volume fraction is known. This aspect of the technique will be discussed in Chapter 6.1.4. Secondly, the assumption is made that the soot produced in the two systems has similar characteristics including the optical properties. The attenuation of laser pulse energy and signal trapping must be known and corrected for. Finally, the assumption must be made that the signal response from the soot in the two systems does not differ due to differences in the ambient gas temperature and pressure between the systems.

In Paper III a theoretical investigation is presented for the characteristics of the experimental setup used for in-cylinder soot volume fraction measurements in a Diesel engine, measurements that will be further discussed in Chapter 6.3.1. Quantitative soot volume fraction images were obtained from the engine by relating the signal levels to those obtained in a rich ethylene-air flat flame. The flame temperature in the calibration point has been estimated to 1700 K based on measurements using rotational CARS in similar flames [175]. The mean temperature and pressure inside the combustion chamber of the Diesel engine varies with crank angle degree (CAD). Data typical for the measurement series are given in Fig. 6.5. The typical pressures are within the range 30-45 bar and the average temperatures are 800-1300 K.
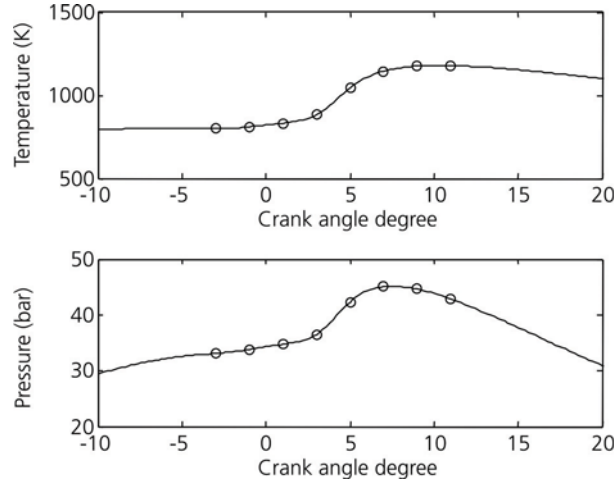
Figure 6.5 *Cycle-averaged in-cylinder pressure and temperature for one of the measurements series presented in Paper III. The markers denote the exact crank angle positions where LII measurements were carried out.*

In order to visualise the influence of these parameters on the LII signal, the model for LII was used to calculate time-resolved signal response for the specific experimental setup. The measurements were carried out using excitation at 1064 nm. Since imaging measurements were carried out, the spatial profile was modelled as a Gaussian sheet. Measured pulse energies and a rough estimation of the dimensions of the laser sheet provided a mean fluence around 0.5 J/cm^2. The spectral sensitivity of the detector system was modelled from the transmission curves for the optics. The results are shown in Fig. 6.6.
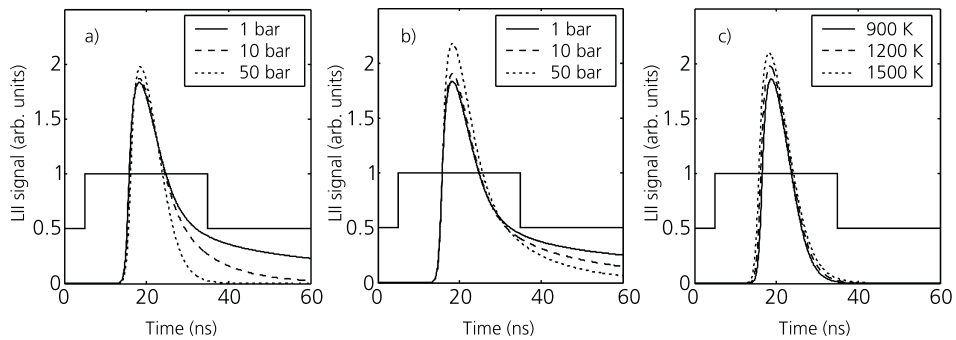
Figure 6.6 *Modelled time-resolved LII signals for different gas pressures and temperatures from Paper III. The primary particle size is set to 30 nm. In a) the pressure is varied for isolated soot particles while keeping the temperature at 1200 K. In b) the pressure is varied for soot particles modelled as aggregates with N_p=500 and T=1200 K. Finally in c) a case is shown for a pressure of 50 bar and isolated particles, where the temperature has been varied. The 30 ns detector gate is indicated.*

The results shown in Fig. 6.6a and b indicate that the ambient gas pressure is a crucial parameter for the LII signal decay, which has its origin in the increased rate of heat conduction with increasing pressure. The level of aggregation is predicted to reduce the heat conduction rate as it effectively reduces the area available for heat conduction due to the shielding effect (Chapter 5.2.1.3). Figure 6.6c indicates that the influence of ambient gas temperature is minor. The small discrepancies are related to the somewhat different maximum temperatures predicted for soot particles in the wings of the Gaussian spatial profile.

If relating the LII signals obtained at the temperature and pressure conditions of the engine with those obtained from the calibration flame without compensating for the aforementioned dependencies, an error will be introduced. In Fig. 6.7 the predicted relative error is shown as function of gate width and crank angle degree for the measurements series with the pressure and temperature given in Fig. 6.5. The absolute value of the time-integrated modelled LII signals at the temperature and pressure in the flame has been compared to the corresponding value obtained when using the temperature and pressure of the engine. It is clearly seen how the error increases with gate width – a result from the strong pressure influence of the delayed LII signal. A short prompt gate minimizes the effects.
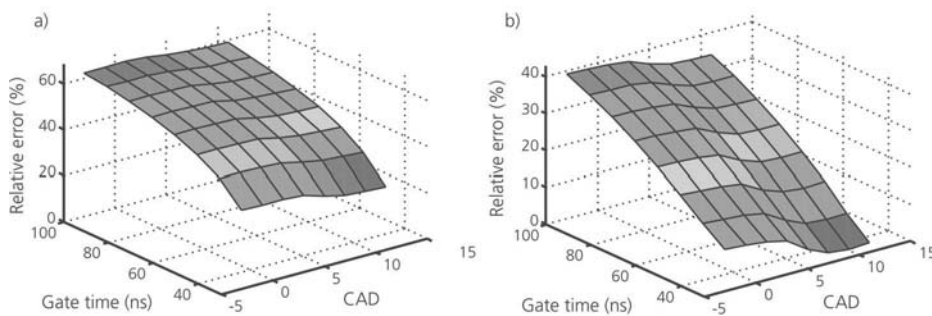
Figure 6.7 *Estimated relative errors for one of the measurements series in Paper III due to the difference in temperature and pressure between engine and calibration flame as function of crank angle degree and detector gate width. The primary particle size is set to 30 nm. a) No aggregation assumed, b) aggregation assumed with N_p=500. The relative error is defined as positive when the signal level in the engine is lower than the corresponding signal in the flame for the same soot volume fraction.*

6.1.4 The relationship between LII signal and soot volume fraction

Soot volume fraction measurements using the LII technique can be made since the signal strength from the heated soot particles are dependent on the particle size and number density of particles in the measurement volume. Since the primary particles are small enough to be considered as volume-absorbers and emitters within the Rayleigh limit assumption, a fact that holds also for aggregates within the RDG-PFA approximation, the prompt LII signal has often been assumed to be

volume-dependent. Neglecting effects of laser light attenuation and signal trapping, the signal is also assumed to be linearly dependent on the number density of soot particles, *N*, in the measurement volume. Since the soot volume fraction for spherical particles may be written according to

$$f_v = N \frac{\pi D^3}{6} \, , \tag{6.1}$$

the LII signal ought to be proportional to the volume fraction, an assumption most often used when evaluating soot volume fraction data using the LII technique. Already in the study by Melton [63] it was shown theoretically that this assumption of linearity is false. As previously discussed in Chapter 3.2.2, he derived a power law relationship between the LII signal and particle size for high-fluence conditions according to

$$S_{LII} \propto ND^x, \quad x = 3 + 0.154/\lambda_{\text{det}} \, , \tag{6.2}$$

where the detection wavelength λ_{det} is given in microns. Though the absorption and emission processes will be approximately volume-dependent, the heat conduction and sublimation processes are area-dependent, the mathematical expressions showing even less dependence than $\propto D^2$ with increasing influence of the continuum regime terms for elevated pressures (See Chapter 5.2.1.3 and 5.2.1.4). While soot-volume fraction measurements may be somewhat complicated by this size-dependence, the same feature has the positive effect of enabling particle-size information to be inferred from time-resolved LII data. However, the effect of the size-dependence on the uncertainties in evaluated soot volume fraction data has been regarded as a generally overlooked issue in LII research [64] since the original study by Melton. In Paper IV a theoretical study is presented in which the influence of the size-dependence on the LII signal is investigated for a large variety of test cases corresponding to different experimental conditions.

The representation of the relationship has been made following two methodologies. The first assumes a power law dependence as suggested by Melton's expression given in Eq. 6.2, and the LII signal is plotted as function of the primary particle size in a log-log representation. If results obtained from different experimental conditions are normalised to the LII signal obtained at the smallest particle size, power-law functions will display as straight lines with the elevation given by the exponent *x*. The result from such an investigation is shown in Fig. 6.8a for a prompt 20 ns gate for varying detection wavelength. Also shown is the exponent *x* derived both by numerically fitting a power law function to the modelled data points and by using the Melton expression. Values show good agreement. The drawback of the log-log representation is that it becomes difficult to compare cases, especially if the size-dependence deviates from a power law. Instead the approach by Seitzman et al. [88] will be used. They derived the relative error introduced to an experiment as function of particle size with respect to a

reference point when assuming a perfect linearity ($\propto D^3$) between the LII signal and soot volume fraction. The relative error can be defined as

$$\varepsilon_r = \frac{C_{\text{test}} - C_{\text{ref}}}{C_{\text{ref}}}, \quad C = \frac{\int_{t_1}^{t_2} S_{\text{LII}} dt}{\frac{\pi}{6} N_p D_0^3}, \tag{6.3}$$

in which D_0 is the initial primary particle diameter, C_{test} is a calibration constant for the test case and C_{ref} for the reference case and S_{LII} is the modelled LII signal for a certain case. As the error will be time-dependent the time-resolved error may also be derived according to

$$\varepsilon'_r(t) = \frac{C'_{\text{test}}(t) - C'_{\text{ref}}(t)}{C'_{\text{ref}}(t)}, \quad C'(t) = \frac{S_{\text{LII}}(t)}{\frac{\pi}{6} N_p D_0^3}. \tag{6.4}$$

In Fig. 6.8b the relative error is shown for the same case as shown in log-log representation in Fig. 6.8a. It is clearly shown how a long detection wavelength minimizes the relative errors and ensures less non-linearity in the relationship between LII signal and soot volume fraction.
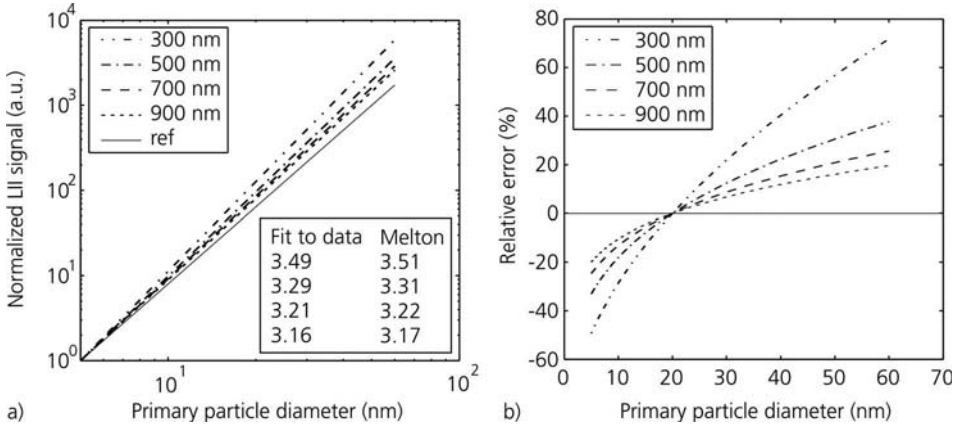
Figure 6.8 *Prompt LII signal vs. primary particle diameter for different detection wavelengths (single-wavelength detection) in a) a log-log representation and b) expressed using relative errors with regards to a reference diameter 20 nm. The laser pulse is modelled for 1064 nm excitation at high fluence (0.4 J/cm²) and using a top-hat spatial distribution of laser energy. The detection gate is 20 ns. The exponent x of a power law has been derived for a) using a power fit to the model data, and by using the Melton expression given in Eq. 6.2.*

In Fig. 6.9 the influence of laser fluence and ambient gas pressure on the relative error is shown. Even when using a prompt 20 ns gate at 0.4 J/cm², the relative errors increase with increasing pressure (Fig. 6.9a). The time-resolved errors shown in Fig. 6.9b indicate that the non-linear relationship between signal and volume fraction increases heavily with time, after the end of the laser pulse for elevated pressure. This can be explained by the increased importance of heat conduction with increasing pressure, effectively increasing the size-dependence on the evaluated particle temperatures. In Fig. 6.9c the relative error is shown for varying laser fluence for a prompt 20 ns gate. Obviously the relationship is closer to linear in the low-fluence regime, which can be explained by the absence of soot sublimation, an area-dependent term that like heat conduction contributes to the nonlinearity.

Figure 6.9 *The relative error as function of ambient gas pressure and laser fluence for 1064 nm excitation using a top-hat profile and detection at 500 nm. In a) and c) the relative error for gated detection (20 ns prompt) is shown and b) and d) show the time-resolved error obtained at 30 nm with respect to a reference point at 20 nm.*

71

The relationship between the LII signal and the soot volume fraction is obviously complex and dependent on a number of both experimental and physical parameters. The relative errors may be minimized by the correct choice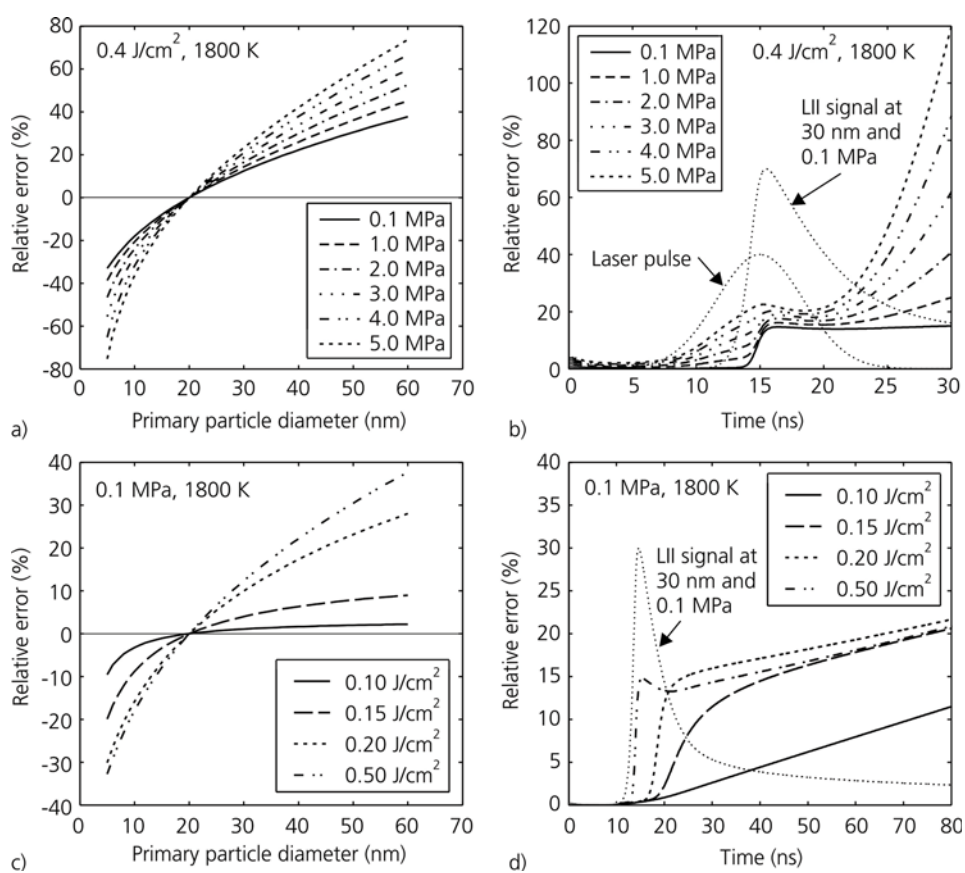 of experimental settings. The results presented in Paper IV show that longer detection wavelengths are beneficial. Delayed detection should be avoided especially at elevated pressures. LII measurements carried out using prompt detection in the low-fluence regime are predicted to show a nearly linear relationship to soot volume fraction, as long as the particles are small enough to be treated as volume absorbers. The spatial distribution of laser energy has little impact on the size-dependence at high fluences. Measurements performed at lower gas temperatures increase the non-linearity, but not when using prompt short detection in the moderate-to-high fluence regime. In addition to providing estimates of the uncertainty in evaluated soot volume fraction data, the results presented in Paper IV may be used to compensate LII signals obtained at different experimental conditions if the particle sizes can be estimated, thus decreasing the uncertainty in the data when interpreted as soot volume fraction.

6.2 Theoretical and experimental comparisons of LII signals

In collaboration with the group of Pascale Desgroux at CNRS in Lille, France, experiments were made using both the conventional right-angle detection and the backward detection of the LII signal. This work is presented in Paper II. Comparisons between experimental and theoretical LII signals are usually carried out using an approach where the experimental setup is adjusted in order to minimize the number of model parameters and subroutines that have to be known for accurately describing the experimental conditions. Typically top-hat profiles and single-wavelength detection are used. In this study the complete opposite approach was made: The characteristics of the experimental setup were either directly measured or estimated and could later be used as input for the model in an attempt of creating predictions comparable with experimentally obtained LII signals. One particular purpose of the experiment was to investigate the possibilities of predicting the LII signal response using a non-uniform, but well-known, spatial distribution of the laser energy.

The experimental setup is shown in Fig. 6.10a. A laser beam from a Nd:YAG laser operating at 1064 nm was directed through a diaphragm creating a thin non-uniform spatial profile. The resulting thin beam was aligned through a laminar methane diffusion flame created using the burner discussed in Chapter 4.3.2. Measurements were carried out 35 mm above the burner, in a region with nearly constant soot volume fraction as function of x and z in the narrow region of the laser beam (See Fig. 6.10b). The LII signal was imaged both using the backward configuration via a beam splitter, and by using the right-angle configuration. Figure 6.10b shows the measurement volume defined by the intersection between
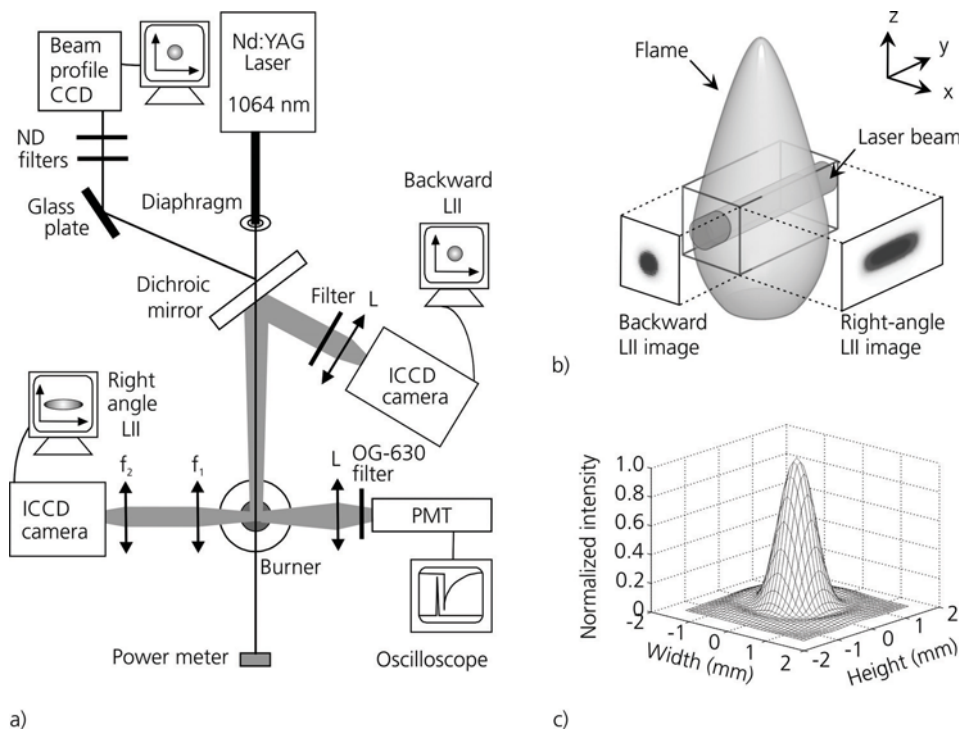
Figure 6.10 *The experimental setup used for LII signal imaging in a diffusion flame using both backward and right-angle detection. In a) the setup is schematically presented, whereas b) shows the measurement volume with respect to the flame and the beam. In c) the spatial distribution of the laser energy is shown. L = Lens, f_1 = 400 mm and f_2 = 200 mm. From Paper II.*

the sooting flame and the laser beam. The definitions of the spatial coordinates will be used throughout this chapter. Time-resolved signals were also obtained using a PMT. The spatial distribution of laser energy was monitored by a beam profiler CCD camera via a series of reflections on flat window surfaces as shown in Fig. 6.10a. The spatial distribution of the laser energy is shown in Fig. 6.10c.

The theoretical predictions of the LII signal were obtained using the model for LII described in Chapter 5. In an ideal situation where the particle size, soot volume fraction and the optical properties of soot are constant within the measurement volume, the LII signal would only be expected to depend on the local laser fluence within the laser beam. If attenuation of the laser beam and the LII signal can be neglected and the laser beam dimensions are constant along the *y*-dimension, the problem will be even further simplified. The laminar diffusion flame satisfies some of the criteria of this ideal case, but definitely not all. The soot volume fraction distribution as function of height, determined from the shape of the experimentally obtained LII signals, was found to be nearly uniform as

function of x and z, but non-uniform along the y-dimension. The radial profile along the y-dimension was measured using right-angle LII and was used as input to the model. The soot volume fraction levels in the flame were found to give absorption losses on the order of 1% and attenuation effects were therefore neglected. Particle size information was not available prior to the experiments, and therefore the time-resolved LII data obtained using the PMT was used to estimate the average size. The gas temperature was assumed to be constant at 1800 K. Using the previously discussed parameters as input, the model for LII delivered spatially high-resolved images of LII signals integrated along the optical axis of the detection systems. These high-resolved signals were, however, not directly comparable to the ones obtained experimentally, since the spatial resolution of the detection system was much lower than the model data, which had the same resolution as the data obtained using the beam profile CCD camera. To compensate for this difference, target grids were imaged using both detection systems establishing their depth-of-field and spatial resolution. The depth-of-field was found to be larger than the measurement volume for both systems, whereas especially the backward LII system had a drastically lower spatial resolution than the beam profiler. A routine was implemented in order to reduce the spatial resolution of the modelled images to those of the experimental systems. In Fig. 6.11 a comparison is shown between experimental and theoretical LII signal images for the two detection configurations obtained using a 100 ns prompt gate.
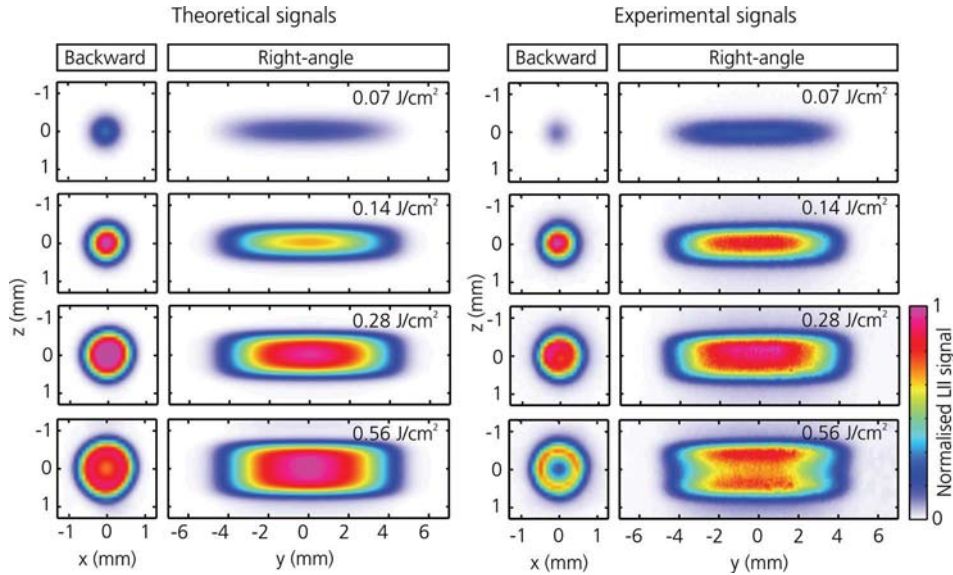
Figure 6.11 *LII signals obtained both experimentally and theoretically from backward and right-angle detection in the methane diffusion flame. Detection has been made for a 100 ns prompt gate for varying mean fluence. Note that the data has been individually normalised to the maximum value within each column making it possible to compare the signal levels between the images for a given configuration as function of mean fluence. From Paper II.*

74

At the lowest mean fluence of 0.07 J/cm^2 the signal is weak, a result from being in the low-fluence regime below the sublimation threshold. As the mean laser fluence is increased, the signal reaches an approximate maximum value, indicating a fluence-dependence corresponding to the plateau region discussed in Chapter 3.2.2. At the same time, the measurement volume is effectively increased in the wings of the laser beam, and the backward LII signal clearly shows the reduced signal at the beam centre resulting from strong sublimation at higher fluence. The theoretical results generally catch the behaviour of the experimental results, but discrepancies exist for high fluences were the hole-burning effect seems less pronounced in the theoretical results than in the experimental. This is further illustrated in Fig. 6.12 where the signal levels of the centre pixel in the backward LII images have been plotted as function of laser fluence both for the theoretically and experimentally obtained images. Obviously the shapes of the fluence curves obtained using the model and the experiment differ quite substantially. For the 20 ns prompt gate this is very pronounced, and as the theoretically obtained curve increases with fluence, the one obtained from experimental data actually decreases. For the long delayed gate, the curves show better agreement, but while the general shape tends to be similar at the low fluences, they deviate from another in the high-fluence regime. The experimental high-fluence data also show the tendency to flatten out at high fluences, something less well predicted by the theoretical results.

The reason for these discrepancies may be both due to deficiencies in the
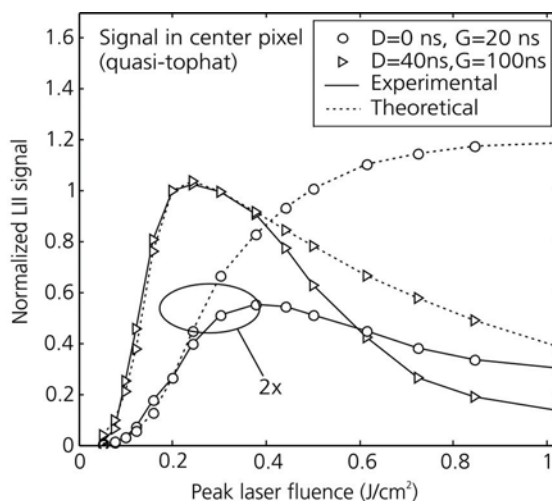
Figure 6.12 *Fluence curves derived from the centre pixel of the theoretical and experimental backward LII images. The theoretical curves have been normalised to the experimental at the peak fluence 0.2 J/cm^2 which corresponds to the mean fluence 0.11 J/cm^2 but the two experimental curves may be compared for absolute intensity. The curve for the 20 ns prompt gate has been multiplied by a factor of 2 making a comparison easier. From Paper II.*

theoretical model and due to uncertainties in the experimental parameters. The discussion in Paper II focus on the theoretical model and the fact that experimental results by Yoder et al. [176] suggest the mass loss to occur earlier during the pulse than predicted by the current sublimation model. An earlier and more pronounced mass-loss effect would be expected to increase the hole-burning at high fluences also at earlier times. Experimental uncertainties like the positioning of the detector gate with respect to the laser pulse may also influence the results, as would the temporal response of the MCP's in the detectors. The uncertainties related to the exact position of the gate with respect to the laser pulse were minimized by defining a time zero with respect to the start of the laser pulse determined using measurements of laser Rayleigh scattering in air when frequency-doubling the output beam of the laser.

6.3   Measurements in internal combustion engines

Two measurement series have been carried out using laser-based diagnostic techniques within the combustion chamber of internal combustion engines, resulting in two publications, Paper III and V, and selected results from these will be discussed in this chapter. In Paper III a theoretical investigation is also presented. This has been discussed in Chapter 6.1.3.

6.3.1   Quantitative soot volume fraction in a Diesel engine

The experimental investigation presented in Paper III was carried out in the combustion chamber of a passenger car Diesel engine. Imaging laser-induced incandescence measurements were performed using two different configurations, in order to visualise the soot volume fraction distribution both from the bottom and from the side. From an engine perspective, the aim was to study the influence on the in-cylinder soot levels of (1) the amount of exhaust gas recirculation (EGR) and (2) the characteristics of the pilot injection. The results with regards to the engine operation are discussed in Paper III and this chapter will solely focus on the diagnostics.

In Fig. 6.13 the two configurations used to image the soot volume fraction in the Diesel engine are shown. The beam from a Nd:YAG laser operating at 1064 nm was formed into a laser sheet using a combination of lenses and aligned through the combustion chamber via the fused silica ring. Two different configurations were used. Imaging of the bowl area was achieved by using a near-horizontal laser sheet, while detecting the signal through the piston bowl via the mirror, as shown in Fig. 6.13a. Vertical imaging through one of the fuel injection regions was achieved by using a vertical laser sheet and detecting the signal from the side via the fused silica ring. The shape of the fused silica piston crown introduced some difficulties for horizontally propagating laser radiation as some of
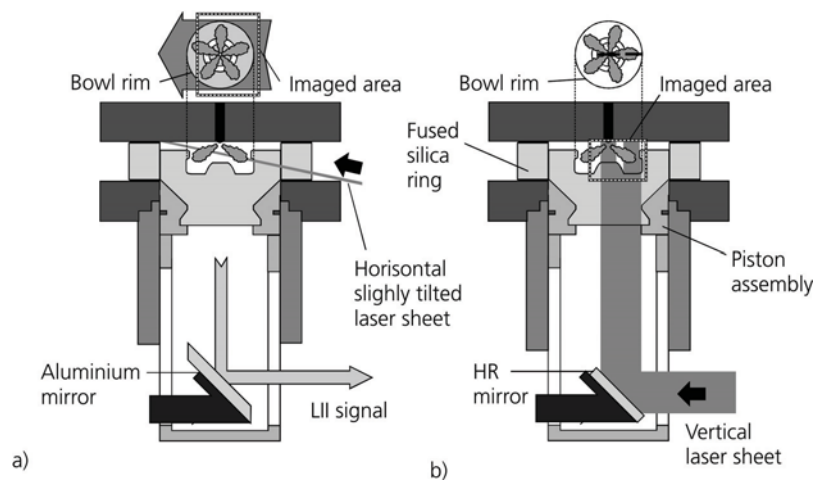
Figure 6.13 *The two configurations used for optical access in the Diesel engine in which measurements of soot volume fractions were carried out within the work presented in Paper III. The figure in a) shows how the signal is collected through the bowl of the piston and in b) how the signal is collected via the fused silica ring.*

the curved surfaces of the bowl created foci in regions within the material with risk of seriously damaging the optical parts. This was the reason for using the somewhat tilted laser sheet shown in Fig. 6.13a, and the somewhat unorthodox method of introducing the laser sheet through the bowl, as shown in Fig. 6.13b. No particular problems with interferences were encountered when dumping the laser sheet into the engine ceiling, an inevitable result from both configurations. This resulted from the fact that the laser operated in the infrared region where the ICCD camera had little or no sensitivity and LII signal was detected below 450 nm enabling efficient spectral filtering. The detector gate was 30 ns centred on the laser pulse and the mean laser fluence was estimated to 0.5 J/cm². Calibration was achieved by comparing the signal levels in the engine with those obtained in a flat ethylene-air flame for which soot volume fractions were determined by extinction. A number of uncertainties introduced by this approach are discussed in Paper III and indeed also in Chapter 6.1.3 and are not repeated here.

The shape of the piston bowl limited the optical access to the combustion chamber due to its curved surfaces. This is illustrated in Fig. 6.14a and b for the two detection configurations respectively. LII signal images were recorded at different crank angle degrees (CAD) and were corrected for detector noise and laser-induced interferences by subtracting each image with reference images recorded while motoring the engine (i.e. operating the engine without internal combustion). The LII images interpreted as soot volume fraction levels were calibrated using results obtained when measuring LII signals in the flat ethylene-air flame with ϕ=2.3 discussed in Chapter 4.3.1. This resulted in quantitative soot
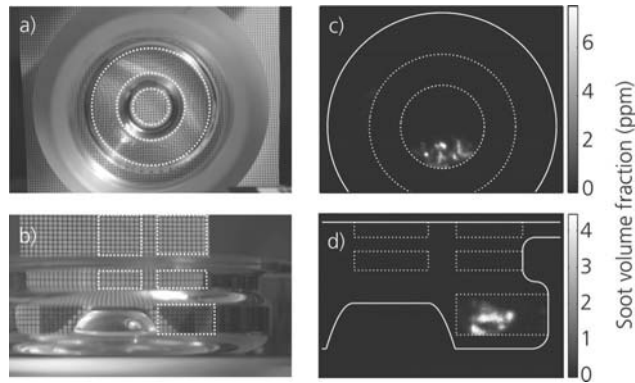
Figure 6.14 *The optical access through the fused silica piston is shown in a) for the bottom view and b) for the side view. The dotted lines mark the regions with optical access. Examples of single-shot soot volume fraction images are shown in c) for the bottom view and d) for the side view, respectively.*

volume fraction data, examples of which are given in 6.14c and d. LII signals obtained from the Diesel engine were highly stochastic in nature. Of 100 single-shots detected at the same crank angle degree (CAD) several images contained little or no signal while other showed very strong signals. With the aim of showing an average distribution of signal for each case, the spatial probability distributions were calculated and plotted. Two examples of these results are shown in Fig. 6.15.
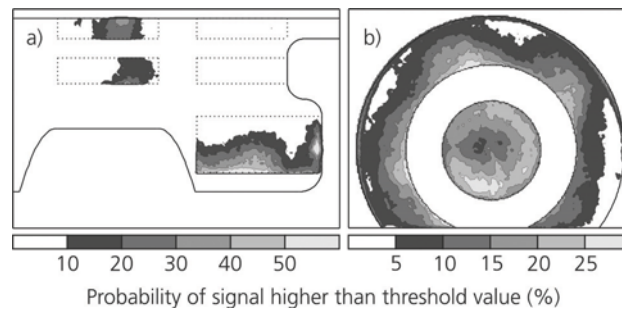
Figure 6.15 *Examples of spatial probability distributions for the soot volume fraction inside the Diesel engine. In a) an example is shown from 13 CAD after top dead centre and in b) at 8 CAD after top dead centre. The contours represent the probability of obtaining a soot volume fraction above a specified threshold level. In a) this was set to 0.1 ppm and in b) 0.02 ppm.*

6.3.2   Flame propagation visualisation in an SI engine

The propagation of the flame front within the cylinder of a spark-ignition engine has been studied by detecting the presence of cool-flame species in the unburnt gas mixture at two individual moments during single engine cycles. The intermediate
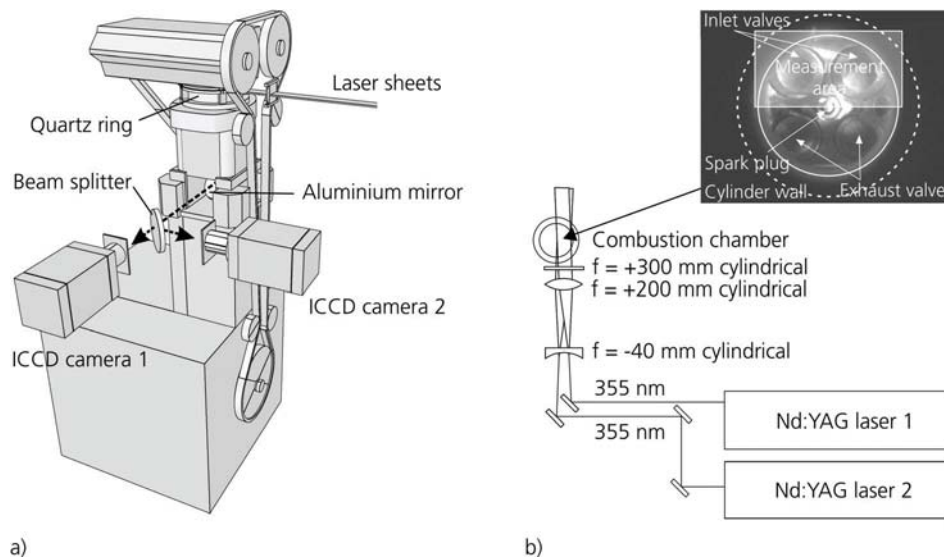
Figure 6.16 *Experimental setup for the measurements of flame propagation in the SI engine. In a) the single-cylinder AVL research engine is shown together with the two detector systems and the beam splitter and in b) a schematic view of the sheet-forming approach is given.*

species, from which the characteristic spectroscopic signature of formaldehyde was identified, can be present in large enough quantities to be detectable by the laser-induced fluorescence technique. This technique and cool-flame species as flame-front markers have been discussed in Chapter 3.3.

The experimental setup is shown in Fig. 6.16. Two Nd:YAG lasers operating at 355 nm were used to excite the cool flame intermediates, and the resulting fluorescence was detected using two ICCD cameras. The beams from the two Nd:YAG lasers were formed into sheets using a set of cylindrical lenses. As can be seen in Fig. 6.16, the two laser sheets were aligned through the lens system with slightly different directions crossing each other within the centre of the cylinder. This scheme was used to prevent the reduction of laser pulse energy introduced by using beam splitters to align the beams into one path. Detection was made via the hollow piston extension as discussed in Chapter 4.4.3 and the signal was aligned onto the two ICCD cameras using a beam splitter with ~50% transmittance. The laser and detector systems were triggered independently, making it possible to set the time separation between the pulses arbitrarily. A time separation of 1.5 CAD (corresponding to ~210 µs) was found to be optimal for evaluating the propagation of the flame front.

The use of individual laser and detector systems made certain considerations necessary during image evaluation and a scheme was developed as outlined in Fig. 6.17. First the images were corrected for background resulting from detector noise
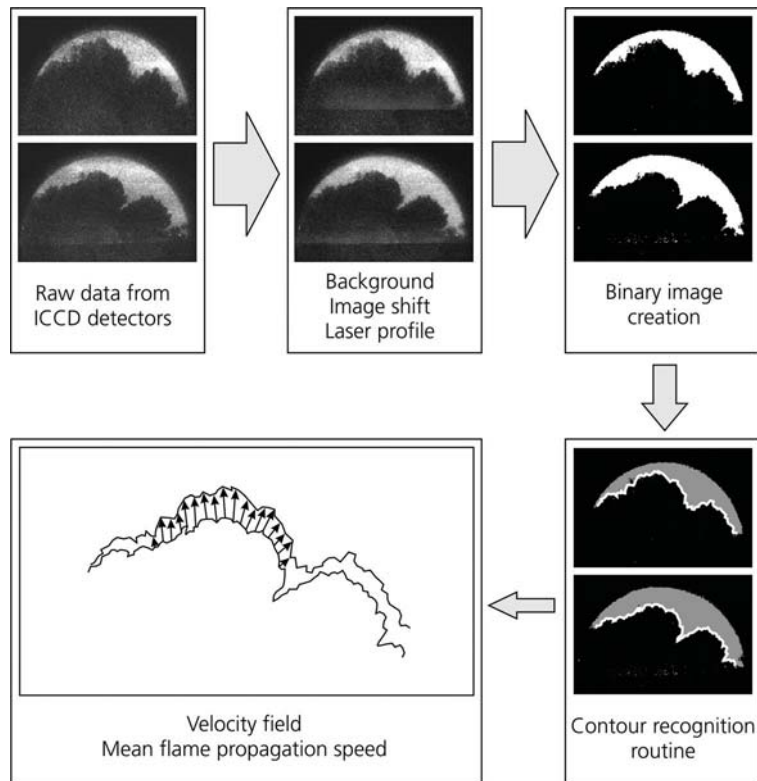
Figure 6.17 *The data evaluation scheme used for extracting flame propagation measurements in the SI engine presented in Paper V.*

and laser-induced interferences from particles and deposits. The images were also individually compensated for a non-uniform spatial profile along the laser sheet width. In a second step, binary images were created from the compensated raw data. The threshold value determining whether or not a pixel contained signal was calculated individually for each image using a routine based on the shape of the intensity histograms of the image. This approach ensured that differences between the two detector systems, as well as the presence of strong but spatially small interference signals did not affect the choice of threshold. A contour recognition algorithm was applied to the binary images and the velocity field could be estimated by establishing the distance between corresponding points along the two contours.

Just a fraction of the total available number of recorded image pairs could be used for evaluating contours and velocity fields. The first limiting factor was that sufficient signal-to-noise ratio was required in both images within a pair in order to achieve spatial information with high enough accuracy. In order to estimate the
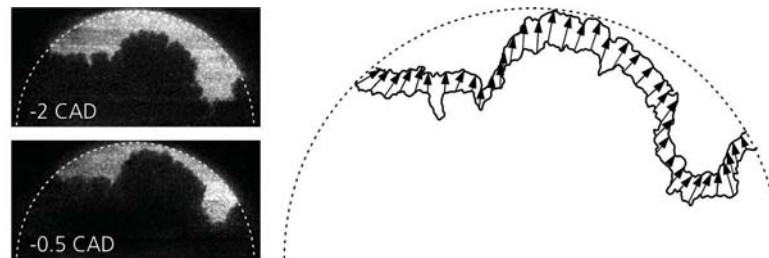
Figure 6.18 *A pair of laser-induced fluorescence images of cool-flame species obtained from the combustion chamber of the SI engine. The dotted lines indicate the view through the piston.*

flame front velocity using 2D data, the assumption must be made that the flame propagates parallel to the image plane, which is not necessarily true especially in the centre of the cylinder. Image pairs sometimes showed artefacts where some regions had holes, and for those cases three-dimensional movement of the flame front was a probable cause. An example of an image pair obtained from the SI engine is shown in Fig. 6.18. The mean flame speed evaluated from the mean velocity field was 15 m/s.

The approach of estimating the flame front propagation inside the combustion chamber of an SI engine using detection of cool flame species was found quite useful, but is limited to fuels that actually form cool-flame species in detectable concentrations, and even for those who do, the concentrations are only high enough to be detected when the temperature is sufficiently high, which limits measurements to piston positions close to top dead centre. However, the adding of additional fuel tracers are not needed, and the fluorescence signal from the cool flame species was found to be relatively strong when excited using the readily available 355 nm excitation of the Nd:YAG laser.

Chapter 7

Summary and outlook

The main aim of the work presented in this thesis has been to implement, improve and apply a theoretical model for the laser-induced incandescence (LII) technique yielding predictions on the LII signal behaviour in different systems. This has included an extension to account for arbitrarily shaped primary particle size distributions and spatial distributions of laser energy in the measurement volume. The model has been used to investigate the predicted errors introduced in various experimental situations when assuming a simplified system with respect to a certain parameter. This includes the assumption of a monodisperse primary particle size distribution (Paper I), linear relationship between signals obtained in a calibration burner and in an internal combustion engine (Paper III) and finally, when assuming a perfect linear relationship between LII signal and soot volume fraction (Paper IV). The model has also been used to characterise the spatially resolved LII signals from a methane diffusion flame detected both using the conventional right-angle detection and the backward detection (Paper II). The non-uniform spatial distribution of laser energy was measured and directly input to the model in order to predict the signal response. The experimental and theoretical results showed generally good agreement, but the theoretical results seemed to overpredict the signal at high laser fluence. Laser-diagnostic techniques were also applied for in-cylinder engine measurements. The laser-induced incandescence technique was applied in a high-speed direct-injection passenger car Diesel engine with realistic combustion chamber geometry and quantitative data were attained by calibrating the signal to that obtained in a calibration flame. Finally, the laser-induced fluorescence (LIF) technique was applied inside the combustion chamber of a spark-ignition engine in order to measure the flame propagation at individual engine cycles and image evaluation schemes were created in order to estimate flame fronts from fluorescence images of intermediate species in the end gas.

Before attempting a discussion of possible future work, it is beneficial to view the present work in its historic context. Indeed, every piece of work can be seen as a small link in a chain. Soot measurements using laser diagnostics has a relatively long history in Lund with publications dating as far back as 1988 [177]. The LII activities in Lund started in the mid 90's [84] and were during the late 90's

focusing on experimental investigations in flat flames pursuing simultaneous measurements of soot volume fraction and particle size [86,178]. The original Melton model was applied to infer particle size information but no detailed analysis of the theoretical descriptions and implementations were undertaken. The work presented in this thesis has been ongoing since the middle of 2001 and can be seen as the first step towards strengthening the theoretical knowledge of LII in Lund. The first new version of the model for LII was implemented following an, at that time, relatively new publication from Snelling et al. [118]. Apart from this work, the available literature on LII models were rather few, most noteworthy being the original paper by Melton [63], the relatively detailed SAE paper by Hofeldt [158] and the studies by Roth and Filippov [111] and Will et al. [119]. Initially the work focused on particle sizing, but later took a turn towards soot volume fraction measurements where our group in Lund collaborated with the group of Pascale Desgroux in Lille within the European project AEROTEST, where the purpose has been to improve the backward LII technique for quantitative soot volume fraction measurements in the exhausts from gas turbines.

During the time period covered by the work presented in the thesis, the LII community has undergone a quite radical change. The group at NRC in Canada led by Greg Smallwood initiated a large investment in fundamental research within the field and has contributed with a substantial part of the publications during the 2000's. In 2003 Hope Michelsen at Sandia National Laboratories in USA presented a new model totally redesigned in many of the sub models and equipped with a series of new ones not previously considered [38]. People were gradually realising the importance of an improved theoretical knowledge base and also that the conventional forums for discussions, such as the Combustion Symposium and the Gordon Conference on Laser Diagnostics in Combustion, were too large for these issues to be efficiently discussed. Clearly a new forum was required in which the LII community could discuss more openly and efficiently the different aspects of the technique. To the author's knowledge, an informal discussion at the Gordon Conference in Oxford in 2003 was the starting point of what was to become the newly established biannual LII Workshop series. The first workshop was held in Duisburg 2005 and resulted in a special issue in the journal Applied Physics B, within which Paper II is included. Model comparisons were also initiated and the research groups were encouraged to submit results obtained with their respective model on predefined test cases. The results from this first investigation have been reported in [64] and clearly show large discrepancies between the different models even for quite simplified test cases. An example is shown in Fig. 7.1 for 532 nm excitation at low fluence, a gas temperature of 1800 K and pressure 1 bar.

For the second LII workshop held in Bad-Herrenalb, Germany in 2006, a more extensive model comparison was undertaken in order to pinpoint which of the mechanisms and parameters that were giving rise to the large discrepancies for different model scenarios. The outcome of this comparison resulted in a paper accepted for publication in Applied Physics B [167], also included as related work
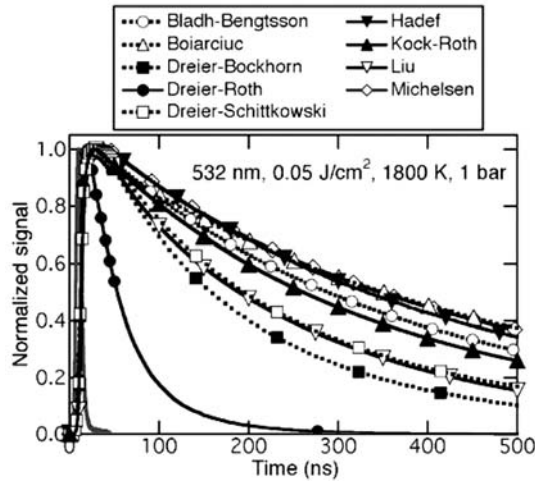
***Figure 7.1** Example from the model comparison from the first LII Workshop in Duisburg, Germany in 2005. Modelled LII signals are shown for an excitation wavelength of 532 nm using a laser fluence of 0.05 J/cm² having a top-hat spatial distribution of laser energy and a temporal distribution of laser energy given from file (FWHM 6.9 ns). The ambient gas temperature was 1800 K and the pressure 1 bar. Detection was square band-pass 610-650 nm and the particle size was 30 nm. Each modelled profile has been normalized to unity at the maximum signal intensity. Reproduced from [64].*

in this thesis (Paper D). An example from these comparisons is shown in Fig. 7.2. The example shows results obtained with individual models and unconstrained parameters, i.e. where optical and physical parameters were different depending on the model. Obviously the discrepancies are large both in evaluated particle temperature and diameter, and the corresponding LII signal behaviour will be quite different. The study showed, however, that these discrepancies are significantly reduced when constraining a number of parameters including the density and specific heat of soot, ρ_s and c_s, the absorption function, $E(m)$, the average molecular weight of air, m_g, and the thermal and mass accommodation coefficients, α and β. However, this is most discernable at low fluence, whereas the high-fluence results still appear sensitive to the approach used to predict the sublimation rates in the respective models.

The developments within the community of LII model research outlined here, to which the results presented in this thesis hopefully contribute, may form a base for discussing future work. The work on the theoretical model for LII presented in the thesis has mainly concerned secondary effects on the LII signal behaviour as a result from non-uniform spatial distributions of laser energy and primary particle size, and the influence of aggregation. Future development and improvements of the theoretical model must necessarily include new mechanisms, like for instance thermal annealing [38]. There is, however, always a risk when incorporating new
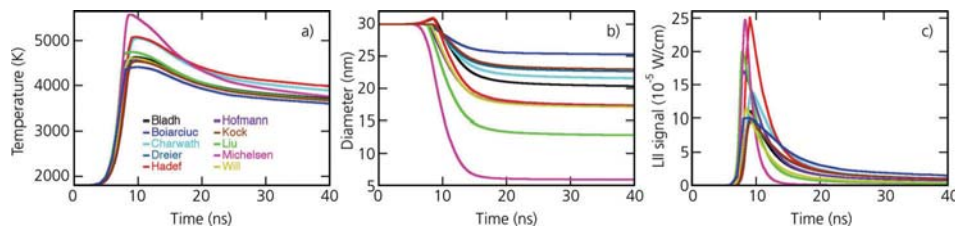
Figure 7.2 Example from the model comparison from the second LII Workshop in Bad Herrenalb, Germany 2006. The compared results are from the unconstrained, independent models. Calculated (a) temperatures, (b) diameters, and (c) LII signals are shown as function of time for ten models identified in the legend. Calculations were performed for a fluence of 0.70 J/cm² for 532 nm excitation using a top-hat spatial distribution of laser energy and the temporal distribution of laser energy given from file (FWHM 6.9 ns). The particle size was 30 nm, the ambient gas temperature 1800 K and pressure 1 bar. The detection wavelength was at 500 nm integrated over the whole area for a single primary particle.

mechanisms in a model where they all affect the same output variables, in this case the particle temperature and diameter, that being an increase in the levels of freedom of the solution. Therefore it is of utmost importance to pursue not only the theoretical work, but also to conduct experimental investigations attempting to measure properties linked to the different mechanisms thus attempting to study them individually. Examples of such investigations have been presented by Beyer and Greenhalgh [179] measuring the absorption function directly using low-pressure LII and Yoder et al. [176] measuring the reduction of particle size time-resolved during the laser pulse. In addition to incorporating new mechanisms, the treatment of the already utilized mechanisms must be reviewed. Heat conduction [125] and recently to some extent also radiation [161] has been investigated, but the sublimation model is still relatively uncertain, also with regards to the influence of aggregation on the process.

Experimentally, the LII technique has been developed quite a bit during recent years and the use of two-colour LII and absolute calibration has taken the technique to new levels of accuracy. There are, however, still a number of factors to consider. The influence of the temporal profile of the laser on the LII signal seems to be a generally overlooked aspect, at least for LII using nanosecond pulse excitation. The temporal response of the detector system may also be important to consider as recently investigated by Charwath et al. [135]. This will be especially important in high-pressure applications due to the short decay time of the LII signal, and Bougie et al. presented a deconvolution scheme for their engine measurements in [115]. The two-colour detection scheme may also be extended to three or multiple wavelengths or even spectrally resolved as performed by Schraml et al. [180]. One interesting application is to use a streak camera equipped with a spectrometer to resolve the LII signal both temporally and spectrally during and somewhat after the laser pulse. Further investigations of the thermal

86

accommodation coefficient in different gases will be highly important since this property affects the evaluated particle sizes using the time-resolved LII technique. The extraction of particle size distributions from LII signal decays has aroused a lot of interest recently, but more theoretical and experimental investigations are clearly needed to establish the limits of the technique applied in different environments. A very recent study by Daun et al. [181] reviews some of the schemes reported in the literature for extracting particle size distribution from time-resolved LII signal decays and it is evident from this study that the uncertainties introduced on the results due to model parameter uncertainties and detector noise may be quite substantial. Since the LII technique probes the primary particle size, combined measurements using for instance scattering techniques may also be fruitful not least for better knowledge on the influence of aggregation on the LII signal.

Last but not least the recent trend of focusing on particle sizing has the drawback of leaving the soot volume fraction measurements somewhat in the dark. However, the soot volume fraction is equally important to know in most systems, and decreasing the uncertainties introduced due to the size-dependence of the signal relationship and the calibration approach will be highly important for future research.

Appendix A

Nomenclature

Symbols

a_{HC}	Equivalent heat conduction radius, $a_{HC} = D_{HC}/2$ (m)
A_F	Fraction of the total cross-sectional area of the measurement volume exposed to the specific laser fluence $P_F \times E$
c	The speed of light (2.998×10^8 m/s)
c_s	Specific heat of soot, see Chapter B.1 (J/kg K)
C	Constant of proportionality defined in Eq. 6.3
C'	Time-resolved constant of proportionality defined in Eq. 6.4
C_{abs}	Total absorption cross section for an aggregated soot particle (m^2)
$C_{s,abs}$	Absorption cross section for single primary soot particles in the Rayleigh limit, see Eq. 5.4 (m^2)
C_p	Heat capacity for the ambient gas, see Chapter B.1 (J/mole K)
D	Primary particle diameter (m)
D_0	Initial value of the primary particle diameter prior to heat-up (m)
D_{av}	Mean diameter of a Gaussian particle size distribution, see Eq. 5.46 (m)
D_f	Fractal dimension, see Eq. 5.1
D_{FWHM}	Full width at half maximum of a Gaussian particle size distribution, see Eq. 5.46 (m)
D_g	The geometric mean diameter of a lognormal distribution, see Eq. 5.45 (m)
D_{HC}	Equivalent heat conduction diameter, i.e. diameter of a single sphere having the same heat conduction properties as that of the aggregate (m)
D_h	Scaling constant for aggregate model, see Eqs. 5.9 and 5.10
E	Laser pulse energy (J)

89

$E(m)$ The absorption function, see Eq. 3.2

f Eucken correction for the thermal conductivity of polyatomic gases, See Eq. 5.13

f_v Soot volume fraction

F Laser fluence (J/m^2)

$F(m)$ Function of the refractive index, see Eq. 3.2

$g(t)$ Normalised temporal distribution of laser energy (s^{-1})

G Geometry-dependent heat transfer factor given in Eq. 5.12 (~19.5 at 1800 K and $\alpha = 0.3$)

h The Planck constant (6.626 × 10^{-34} Js)

h_s Height of Gaussian sheet, see Eq. 5.48 (m)

ΔH_v Heat of sublimation of soot, see Chapter B.5 (J/mole)

$I(T,\lambda)$ Emission from hot soot particles (grey body emission, Eq. 3.3) (W/m^3)

k_B The Boltzmann constant (1.38×10^{-23} J/K)

k_f Fractal prefactor, see Eq. 5.1

k_g Heat conduction coefficient of the surrounding gas, see Chapter B.3 (W/m K)

k_h Scaling constant for aggregate model, see Eqs. 5.9 and 5.10

K_{abs} The absorption coefficient, see Eq. 3.5 (m^{-1})

K_{ext} The extinction coefficient, see Eq. 3.6 (m^{-1})

Kn   The Knudsen number, see Eq. 5.7

L Absorption path length, see Eq. 3.6 (m)

L_g Characteristic length scale in definition of the Knudsen number, see Eq. 5.7 (m)

m Refractive index of soot

m_g Average mass of gas molecules (4.78×10^{-26} kg)

M Mass of a primary soot particle (kg)

M_λ^b The Planck radiation law, see Eq. 5.32 (W/m^3)

M_v Molecular weight of soot vapour, see Chapter B.5 (kg/mole)

n_v Number density of soot vapour given using the ideal gas law in Eq. 5.27 (m^{-3})

N Number density of soot particles or aggregates (m^{-3})

N_A Avogadros constant (6.022×10^{-23} mole^{-1})

N_p Number of primary particles per aggregate

N_v Molecular flux of sublimed carbon clusters (s^{-1}m^{-2})

N_{FM} Free molecular regime expression for N_v given in Eq. 5.24 (s^{-1}m^{-2})

N_C Continuum regime expression for N_v given in Eq. 5.25 ($s^{-1}m^{-2}$)

p Ambient gas pressure (Pa)

$P_{F,i}$ Spatial distribution function for the laser energy, see Eq. 5.48 (m^{-2})

$P_{PPS,i}$ Distribution function for the primary particle size, see Eqs. 5.45 and 5.46 (m^{-1})

P_v Vapour pressure of soot, see Chapter B.5 (Pa)

$\dot{Q}_i$ Energy rate for the sub-mechanism i (J/s)

Q_{vv} Volumetric scattering cross section, see Eq. 3.4 (m^{-1})

R Molar gas constant (8.314 J/mole K)

R_g Radius of gyration of a soot aggregate, see Eq. 5.2 (m)

$R(\lambda)$ Spectral characteristics of the detection system (arb. units)

S_{LII} The LII signal (arb. units)

t Time (s)

T Particle temperature (K)

T_δ The temperature inside the limiting sphere in the Fuchs heat conduction model (Chapter 5.2.1.3) (K)

T_g Ambient gas temperature (K)

w Radius ($1/e^2$) of the spatial Gaussian distribution functions in Eq. 5.48 (m)

Greek symbols

α Thermal accommodation coefficient. The value 0.3 has been used for the results presented in Paper II, III and IV. The results presented in Paper I were derived using the McCoy and Cha model with $G = 22.064$.

β Mass accommodation coefficient, sometimes referred to as the evaporation coefficient. The value 0.8 is used following Snelling et al. [118]

δ The distance between the equivalent heat conduction radius and the limiting sphere in the Fuchs heat conduction model (Chapter 5.2.1.3) (m)

ε The emissivity of soot, given for the Rayleigh limit in Eq. 5.33

ε_r Relative error introduced to the evaluated soot volume fraction due to the size-dependence of the LII signal, see Eq. 6.3

ε_r' Time-resolved relative error introduced to the evaluated soot volume fraction due to the size-dependence of the LII signal, see Eq. 6.4

ϕ The equivalence ratio, see Eq. 2.2

γ The heat capacity ratio, $C_p/(C_p - R)$

γ^* The mean heat capacity ratio, see Eq. 5.16

Γ	The Gamma function
Γ_{diff}	Diffusion coefficient for soot vapour, see Eq. 5.26 (m²/s)
λ	Wavelength of electromagnetic radiation (m)
λ_{det}	Detection wavelength in the Melton expression, see Eq. 3.9 (μm)
λ_g	Mean free path of the ambient gas, see Eq. 5.8 (m)
λ_δ	Mean free path of the gas inside the limiting sphere in the Fuchs heat conduction model. Related to λ_g by Eq. 5.19 (m)
Λ_1	Function within the Fuchs heat conduction model (See Eq. 5.20)
Λ_2	Function within the Fuchs heat conduction model (See Eq. 5.20)
ρ_s	Density of soot, see Chapter B.2 (kg/m³)
σ	Molecular cross section for sublimed species (m²). The cross section for C_3 (4.5×10^{-19} m²) given by Michelsen [38] is used.
σ_g	The geometric standard deviation of a lognormal distribution, see Eq. 5.45
ζ	The Riemann Zeta function

Appendix B

Some functions describing physical quantities

Appendix B lists the temperature-dependent functions for soot and ambient gas properties used within the model for laser-induced incandescence (LII). A wavelength-dependent function describing the absorption function $E(m)$ is also given.

B.1 The heat capacity of the ambient gas, C_p, and specific heat of carbon, c_s

One expression is used for both these quantities but using different coefficients. Both expression and coefficients have been given by Michelsen [38]. The expression can be written as

$$C = \frac{R}{a_4} \left[\frac{a_1 \left(\frac{\theta_1}{T}\right)^2 e^{\theta_1/T}}{(e^{\theta_1/T}-1)^2} + \frac{a_2 \left(\frac{\theta_2}{T}\right)^2 e^{\theta_2/T}}{(e^{\theta_2/T}-1)^2} + a_3 T \right], \tag{B.1}$$

in which R is the molar gas constant and the coefficients are given in Table B.1.

Table B.1 *The coefficients used for C_p and c_s*

	C_p (J/mole K)	c_s (J/kg K)
a_1	3.498	1.115
a_2	0.98378	1.789
a_3	2.5766×10^{-5} K^{-1}	1.16×10^{-4} K^{-1}
a_4	1	12.01×10^{-3} kg/mole
θ_1	1 K	597 K
θ_2	3353.5 K	1739 K

The coefficients for C_p have been obtained by Michelsen [38] by fitting Eq. B.1 to data on N_2 from Chase et al. [182], and the coefficients for c_s by fitting the same expression to data on graphite from Fried and Howard [183]. The two functions are shown in Fig. B.1.
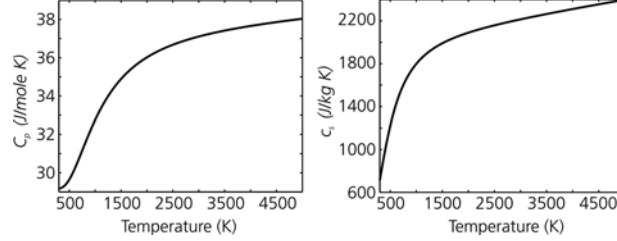
Figure B.1 *The functions used for the molar heat capacity of the ambient gas, C_p, and the specific heat of soot, c_s.*

B.2 The density of soot, ρ_s

The density of soot is modelled using the linear expression

$$\rho_s = 2303.1 - 7.3106 \times 10^{-2} T \tag{B.2}$$

derived by Michelsen [38] by fitting data for graphite obtained from Fried and Howard [183]. The resulting curve is shown in Fig. B.2.

B.3 The heat conduction coefficient, k_g

The heat conduction coefficient, also referred to as the thermal conductivity, is modelled using the linear expression

$$k_g = 1.0811 \times 10^{-2} + 5.1519 \times 10^{-5} T \tag{B.3}$$

derived by Michelsen [38] by fitting data for air obtained from [184]. The result is shown in Fig. B.2.

B.4 The absorption function, $E(m)$

The absorption function is dependent on the refractive index of soot according to Eq. 5.5. The function enters in both the formulation for absorption and emission of electromagnetic radiation by soot particles and thus appears at three locations in the system of equations making up the model: In the absorption and radiation terms of the heat balance (Eq. 5.6 and 5.31), and in the expression for the LII signal (5.44). In most of the work presented in this thesis the refractive index has been treated as wavelength-independent. However, in Paper IV a wavelength-dependent function has been used for the absorption function $E(m)$ according to

$$E(m) = 0.232 + 1.2546 \times 10^5 \lambda \tag{B.4}$$

derived by Snelling et al. [164] by fitting the data presented by Krishnan et al. [185]. For the radiation term, which has been derived using the assumption of a
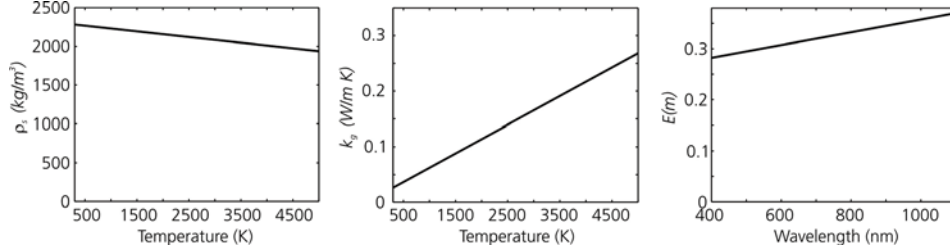
94

Figure B.2 *The density of soot, ρ_s, the heat conduction coefficient, k_g, and the wavelength-dependent expression for the absorption function E(m)*

wavelength-independent $E(m)$ as outlined in Chapter 5.2.1.5, the value obtained from Eq. B.4 using $\lambda = 600$ nm is used. The function is shown in Fig. B.2.

B.5 The vapour pressure of soot, P_v, the mean molecular weight of soot vapour, M_v, and the heat of sublimation of soot, ΔH_v

In the sublimation mechanism, the thermodynamic properties for an ensemble of vaporised species $C_1,...,C_7$ is used as described in Chapter 5.2.1.4. The data is implemented as polynomials given by Smallwood et al. [124] obtained by fitting the functions to the data on graphite from Leider et al. [186]. The expressions can be written as

$$P_v = \exp\left(\sum_{i=0}^{5} p_i T^i\right) \text{atm}, \quad M_v = \sum_{i=0}^{5} m_i T^i \text{ kg/mole}, \quad \Delta H_v = \sum_{i=0}^{5} h_i T^i \text{ J/mole}, \quad \text{(B.5)}$$

where the coefficients are given in Table B.2

Table B.2 *The coefficients used for the expressions in Eq. B.5*

i	p_i	m_i	h_i
0	-1.2296×10^2	1.7179×10^{-2}	2.05398×10^5
1	9.0558×10^{-2}	6.8654×10^{-7}	7.3660×10^2
2	-2.7637×10^{-5}	2.9962×10^{-9}	-4.0713×10^{-1}
3	4.1754×10^{-9}	-8.5954×10^{-13}	1.1992×10^{-4}
4	-2.4875×10^{-13}	1.0486×10^{-16}	-1.7946×10^{-8}
5	0	0	1.0717×10^{-12}

The functions are shown in Fig. B.3. P_v is implemented in SI units (Pa) in the model.
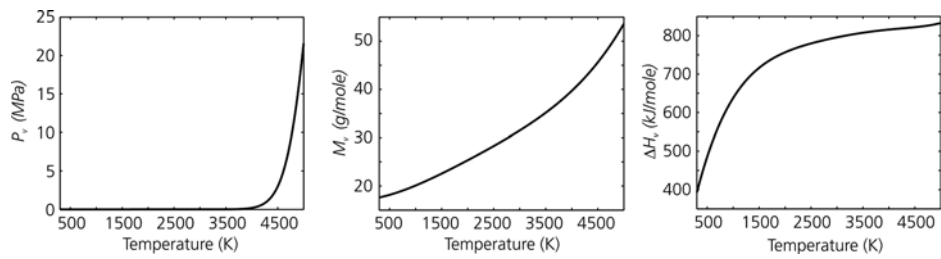
Figure B.3 The functions used for the vapour pressure, mean molecular weight of soot vapour and the heat of sublimation for soot.

Bibliography

1.   IEA, *Key World Energy Statistics 2006.* International Energy Agency, 2006

2.   IEA, *World Energy Outlook 2006, Summary and Conclusions.* International Energy Agency, 2006

3.   Guggenheim, D., *An Inconvenient Truth.* Paramount pictures, 2006

4.   IPCC, *Climate Change 2007: The Physical Science Basis, Summary for Policymakers.* Intergovernmental Panel on Climate Change, 2007

5.   Griffiths, J.F. and Barnard, J.A., *Flame and combustion.* 3rd ed., Blackie Academic & Professional: London, 1995

6.   Highwood, E.J. and Kinnersley, R.P., *When smoke gets in our eyes: The multiple impacts of atmospheric black carbon on climate, air quality and health.* Environment International, **32**:560-566, 2006

7.   Barfknecht, T.R., *Toxicology of Soot.* Progress in Energy and Combustion Science, **9**:199-237, 1983

8.   Glassman, I., *Combustion.* 3rd ed., Academic Press: San Diego, 1996

9.   Heywood, J.B., *Internal combustion engine fundamentals.* McGraw-Hill series in mechanical engineering, McGraw-Hill: New York, 1988

10.   Atkins, P.W., *Physical chemistry.* 6th ed., Oxford University Press: Oxford, 1998

11.   Palmer, H.B. and Cullis, H.F., *The chemistry and physics of carbon.* Vol. 1, Dekker: New York, 1965

12.   Bockhorn, H., ed. *Soot formation in Combustion.* Springer-Verlag: Berlin, 1994

13.   Tian, K., Liu, F.S., Thomson, K.A., Snelling, D.R., Smallwood, G.J., and Wang, D.S., *Distribution of the number of primary particles of soot aggregates in a nonpremixed laminar flame.* Combustion and Flame, **138**:195-198, 2004

14. Shaddix, C.R., Palotas, A.B., Megaridis, C.M., Choi, M.Y., and Yang, N.Y.C., *Soot graphitic order in laminar diffusion flames and a large-scale JP-8 pool fire.* International Journal of Heat and Mass Transfer, **48**:3604-3614, 2005

15. Heitor, M.V. and Moreira, A.L.N., *Thermocouples and Sample Probes for Combustion Studies.* Progress in Energy and Combustion Science, **19**:259-278, 1993

16. Eckbreth, A.C., *Laser diagnostics for combustion temperature and species.* 2nd ed. Combustion science and technology book series, 3, Gordon & Breach: Amsterdam, 1996

17. Gaydon, A.G., *The spectroscopy of flames.* 2nd ed., Chapman and Hall: London, 1974

18. McMurry, P.H., *Review of atmospheric aerosol measurements.* Atmospheric Environment, **34**:1959-1999, 2000

19. Vander Wal, R.L., Zhou, Z., and Choi, M.Y., *Laser-induced incandescence calibration via gravimetric sampling.* Combustion and Flame, **105**:462-470, 1996

20. Snelling, D.R., Smallwood, G.J., Sawchuk, R.A., Neill, W.S., Gareau, D., Chippior, W.L., Liu, F., Gülder, Ö.L., and Bachalo, W.D., *Particulate Matter Measurements in a Diesel Engine Exhaust by Laser-Induced Incandescence and the Standard Gravimetric Procedure.* SAE Technical paper 1999-01-3653, 1999

21. Choi, M.Y., Mulholland, G.W., Hamins, A., and Kashiwagi, T., *Comparisons of the Soot Volume Fraction Using Gravimetric and Light Extinction Techniques.* Combustion and Flame, **102**:161-169, 1995

22. Zhou, Z.Q., Ahmed, T.U., and Choi, M.Y., *Measurement of dimensionless soot extinction constant using a gravimetric sampling technique.* Experimental Thermal and Fluid Science, **18**:27-32, 1998

23. Smallwood, G.J., Clavel, D., Gareau, D., Sawchuk, R.A., Snelling, D.R., Witze, P.O., Axelsson, B., Bachalo, W.D., and Gülder, Ö.L., *Concurrent quantitative laser-induced incandescence and SMPS measurements of EGR effects on particulate emissions from a TDI Diesel engine.* SAE Technical Paper 2002-01-2715, 2002

24. Krüger, V., Wahl, C., Hadef, R., Geigle, K.P., Stricker, W., and Aigner, M., *Comparison of laser-induced incandescence method with scanning mobility particle sizer technique: The influence of probe sampling and laser heating on*

soot particle size distribution. Measurement Science & Technology, **16**:1477-1486, 2005

25. Vander Wal, R.L., *A TEM methodology for the study of soot particle structure.* Combustion Science and Technology, **126**:333-357, 1997

26. Köylü, Ü.Ö. and Faeth, G.M., *Structure of Overfire Soot in Buoyant Turbulent-Diffusion Flames at Long Residence Times.* Combustion and Flame, **89**:140-156, 1992

27. Köylü, Ü.Ö., McEnally, C.S., Rosner, D.E., and Pfefferle, L.D., *Simultaneous measurements of soot volume fraction and particle size/microstructure in flames using a thermophoretic sampling technique.* Combustion and Flame, **110**:494-507, 1997

28. Eisner, A.D. and Rosner, D.E., *Experimental Studies of Soot Particle Thermophoresis in Non-Isothermal Combustion Gases Using Thermocouple Response Techniques.* Combustion and Flame, **61**:153-166, 1985

29. Vander Wal, R.L., Ticich, T.M., and Stephens, A.B., *Can soot primary particle size be determined using laser-induced incandescence?* Combustion and Flame, **116**:291-296, 1999

30. Dankers, S., Schraml, S., Will, S., and Leipertz, A., *Application of laser-induced incandescence for the determination of primary particle sizes of nanoparticles demonstrated using carbon blacks.* Chemical Engineering & Technology, **25**:1160-1164, 2002

31. Kock, B.F., Tribalet, B., Schulz, C., and Roth, P., *Two-color time-resolved LII applied to soot particle sizing in the cylinder of a Diesel engine.* Combustion and Flame, **147**:79-92, 2006

32. Santoro, R.J., Semerjian, H.G., and Dobbins, R.A., *Soot particle measurements in diffusion flames.* Combustion and Flame, **51**:203-218, 1983

33. Santoro, R.J. and Shaddix, C.R., *Laser-Induced Incandescence*, in *Applied Combustion Diagnostics.* Taylor and Francis: New York. p. 252-286, 2002

34. Leipertz, A., Ossler, F., and Aldén, M., *Polycyclic Aromatic Hydrocarbons and Soot Diagnostics by Optical Techniques*, in *Applied Combustion Diagnostics.* Taylor and Francis: New York. p. 359-383, 2002

35. Zhao, H. and Ladommatos, N., *Optical diagnostics for soot and temperature measurement in diesel engines.* Progress in Energy and Combustion Science, **24**:221-255, 1998

36. Kerker, M., *The scattering of light and other electromagnetic radiation.* Physical chemistry, 16, Academic P: New York, 1969

37.   Bohren, C.F. and Huffman, D.R., *Absorption and scattering of light by small particles*, Wiley: New York, 1998

38.   Michelsen, H.A., *Understanding and predicting the temporal response of laser-induced incandescence from carbonaceous particles.* Journal of Chemical Physics, **118**:7012-7045, 2003

39.   Farias, T.L., Köylü, Ü.Ö., and Carvalho, M.G., *Range of validity of the Rayleigh-Debye-Gans theory for optics of fractal aggregates.* Applied Optics, **35**:6560-6567, 1996

40.   Köylü, Ü.Ö. and Faeth, G.M., *Radiative Properties of Flame-Generated Soot.* Journal of Heat Transfer, **115**:409-417, 1993

41.   Faeth, G.M. and Köylü, Ü.Ö. *Soot morphology and optical properties in nonpremixed turbulent flame environments.* Combustion Science and Technology, **108**:207-229, 1995

42.   Krishnan, S.S., Lin, K.C., and Faeth, G.M., *Optical properties in the visible of overfire soot in large buoyant turbulent diffusion flames.* Journal of Heat Transfer, **122**:517-524, 2000

43.   Dalzell, W.H. and Sarofim, A.F., *Optical constants of soot and their application to heat flux calculations.* Journal of Heat Transfer, **91**:100-104, 1969

44.   Stagg, B.J. and Charalampopoulos, T.T., *Refractive indices of pyrolytic graphite, amorphous carbon, and flame soot in the temperature range 25° to 600°C.* Combustion and Flame, **94**:381-396, 1993

45.   Köylü, Ü.Ö. and Faeth, G.M., *Spectral extinction coefficients of soot aggregates from turbulent diffusion flames.* Journal of Heat Transfer, **118**:415-421, 1996

46.   Hottel, H.C. and Broughton, F.P., *Determination of true temperature and total radiation from luminous gas flames.* Industrial and Engineering Chemistry, **4**:166-175, 1932

47.   Distasio, S. and Massoli, P., *Influence of the Soot Property Uncertainties in Temperature and Volume-Fraction Measurements by 2-Color Pyrometry.* Measurement Science & Technology, **5**:1453-1465, 1994

48.   Vattulainen, J., Nummela, V., Hernberg, R., and Kytola, J., *A system for quantitative imaging diagnostics and its application to pyrometric in-cylinder flame-temperature measurements in large diesel engines.* Measurement Science & Technology, **11**:103-119, 2000

49.   Quoc, H.X., Vignon, J.-M., and Brun, M., *A New Approach of the Two-Color Method for Determining Local Instantaneous Soot Concentration and*

Temperature in a D.I. Diesel Combustion Chamber. SAE Technical Paper 910736, 1991

50. Cignoli, F., De Iuliis, S., Manta, V., and Zizak, G., *Two-dimensional two-wavelength emission technique for soot diagnostics.* Applied Optics, **40**:5370-5378, 2001

51. Jenkins, T.P. and Hanson, R.K., *Soot pyrometry using modulated absorption/emission.* Combustion and Flame, **126**:1669-1679, 2001

52. D'Alessio, A., Di Lorenzo, A., Borghese, A., Beretta, F., and Masi, S., *Study of the soot nucleation zone of rich methane-oxygen flames.* Proceedings of the Combustion Institute, **16**:695-708, 1977

53. Bengtsson, P.-E. and Aldén, M., *Application of a Pulsed Laser for Soot Measurements in Premixed Flames.* Applied Physics B, **48**:155-164, 1989

54. Dobbins, R.A., Santoro, R.J., and Semerjian, H.G., *Interpretation of optical measurements of soot in flames.* Progress in Astronautics and Aeronautics, **92**:208-237, 1984

55. Sorensen, C.M., Cai, J., and Lu, N., *Light-Scattering Measurements of Monomer Size, Monomers Per Aggregate, and Fractal Dimension for Soot Aggregates in Flames.* Applied Optics, **31**:6547-6557, 1992

56. Köylü, Ü.Ö. *Quantitative Analysis of In Situ Optical Diagnostics for Inferring Particle/Aggregate Parameters in Flames: Implications for Soot Surface Growth and Total Emissivity.* Combustion and Flame, **109**:488-500, 1996

57. Shaddix, C.R. and Smyth, K.C., *Laser-induced incandescence measurements of soot production in steady and flickering methane, propane, and ethylene diffusion flames.* Combustion and Flame, **107**:418-452, 1996

58. Snelling, D.R., Thomson, K.A., Smallwood, G.J., and Gülder, Ö.L., *Two-dimensional imaging of soot volume fraction in laminar diffusion flames.* Applied Optics, **38**:2478-2485, 1999

59. Charalampopoulos, T.T., *Morphology and Dynamics of Agglomerated Particulates in Combustion Systems Using Light-Scattering Techniques.* Progress in Energy and Combustion Science, **18**:13-45, 1992

60. Lamprecht, A., Eimer, W., and Kohse-Höinghaus, K., *Dynamic light scattering in sooting premixed atmospheric-pressure methane-, propane-, ethene-, and propene-oxygen flames.* Combustion and Flame, **118**:140-150, 1999

61. Weeks, R.W. and Duley, W.W., *Aerosol-particle sizes from light emission during excitation by TEA CO.* Journal of Applied Physics, **45**:4661-4662, 1974

62. Eckbreth, A.C., *Effects of Laser-Modulated Particulate Incandescence on Raman Scattering Diagnostics.* Journal of Applied Physics, **48**:4473-4479, 1977

63. Melton, L.A., *Soot Diagnostics Based on Laser-Heating.* Applied Optics, **23**:2201-2208, 1984

64. Schulz, C., Kock, B.F., Hofmann, M., Michelsen, H., Will, S., Bougie, B., Suntz, R., and Smallwood, G., *Laser-induced incandescence: recent trends and current questions.* Applied Physics B, **83**:333-354, 2006

65. Bengtsson, P.-E. and Aldén, M., *C_2 Production and Excitation in Sooting Flames Using Visible Laser-Radiation - Implications for Diagnostics in Sooting Flames.* Combustion Science and Technology, 77:307-318, 1991

66. Moreau, C.S., Therssen, E., Mercier, X., Pauwels, J.F., and Desgroux, P., *Two-color laser-induced incandescence and cavity ring-down spectroscopy for sensitive and quantitative imaging of soot and PAHs in flames.* Applied Physics B, **78**:485-492, 2004

67. Dec, J.E., zur Loye, A.O., and Siebers, D.L., *Soot distribution in a D. I. diesel engine using 2-D laser-induced incandescence imaging.* SAE Technical Paper 910224, 1991

68. Dec, J.E., *Soot distribution in a D. I. diesel engine using 2-D imaging of laser-induced incandescence, elastic scattering, and flame luminosity.* SAE Technical Paper 920115, 1992

69. Espey, C. and Dec, J.E., *Diesel engine combustion studies in a newly designed optical-access engine using high speed visualization and 2-D laser imaging.* SAE Technical Paper 930971, 1993

70. Pinson, J.A., Mitchell, D.L., and Santoro, R.J., *Quantitative, planar soot measurements in a D. I. diesel engine using laser-induced incandescence and light scattering.* SAE Technical Paper 932650, 1993

71. Dec, J.E., *A conceptual model of DI Diesel combustion based on laser-sheet imaging.* SAE Technical Paper 970873, 1997

72. Inagaki, K., Takasu, S., and Nakakita, K., *In-cylinder quantitative soot concentration measurement by laser-induced incandescence.* SAE Technical Paper 1999-01-0508, 1999

73. Dec, J.E. and Tree, D.R., *Diffusion-flame/wall interactions in a heavy-duty DI Diesel engine.* SAE Technical Paper 2001-01-1295, 2001

74. Case, M.E. and Hofeldt, D.L., *Soot mass concentration measurements in diesel engine exhaust using laser-induced incandescence.* Aerosol Science and Technology, **25**:46-60, 1996

75. Snelling, D.R., Smallwood, G.J., Sawchuk, R.A., Neill, W.S., Gareau, D., Chippior, W.L., Liu, F., Gülder, Ö.L., and Bachalo, W.D., *In-Situ Real-Time Characterization of Particulate Emissions From a Diesel Engine Exhaust By Laser-Induced Incandescence.* SAE Technical Paper 2000-01-1994, 2000

76. Smallwood, G.J., Snelling, D.R., Gülder, Ö.L., Clavel, D., Gareau, D., Sawchuk, R.A., and Graham, L., *Transient Particulate Matter Measurements From the Exhaust of a Direct Injection Spark Ignition Automobile.* SAE Technical Paper 2001-01-3581, 2001

77. Schraml, S., Will, S., and Leipertz, A., *Simultaneous measurement of soot mass concentration and primary particle size in the exhaust of a DI diesel engine by time-resolved laser-induced incandescence.* SAE Technical Paper 1999-01-0146, 1999

78. Schraml, S., Will, S., Leipertz, A., and Zens, T., *Influence of injection parameters of D.I. Diesel engines on soot characteristics.* in *Eighth international conference on liquid atomization and spray systems*, Pasadena, CA, USA, 2000

79. Schraml, S., Heimgärtner, C., Fettes, C., and Leipertz, A., *Investigation of in-cylinder soot formation and oxidation by means of two-dimensional laser-induced incandescence (LII).* in *Proceedings of the 10th International Symposium on Applications of Laser Techniques to Fluid Mechanics*, Lisbon, Portugal, 2000

80. Schraml, S., Will, S., Leipertz, A., Zens, T., and d'Alfonzo, N., *Performance Characteristics of Tire-Lii Soot Diagnostics in Exhaust Gases of Diesel Engines.* SAE Technical Paper 2000-01-2002, 2000

81. Vander Wal, R.L. and Weiland, K.J., *Laser-Induced Incandescence - Development and Characterization Towards a Measurement of Soot-Volume Fraction.* Applied Physics B, **59**:445-452, 1994

82. Quay, B., Lee, T.W., Ni, T., and Santoro, R.J., *Spatially-Resolved Measurements of Soot Volume Fraction Using Laser-Induced Incandescence.* Combustion and Flame, **97**:384-392, 1994

83. Shaddix, C.R., Harrington, J.E., and Smyth, K.C., *Quantitative measurements of enhanced soot production in a flickering methane/air diffusion flame.* Combustion and Flame, **99**:723-732, 1994

84. Bengtsson, P.-E. and Aldén, M., *Soot-Visualization Strategies Using Laser Techniques - Laser-Induced Fluorescence in C$_2$ from Laser-Vaporized Soot and Laser-Induced Soot Incandescence.* Applied Physics B, **60**:51-59, 1995

85. Ni, T., Pinson, J.A., Gupta, S., and Santoro, R.J., *2-Dimensional Imaging of Soot Volume Fraction by the Use of Laser-Induced Incandescence.* Applied Optics, **34**:7083-7091, 1995

86. Axelsson, B., Collin, R., and Bengtsson, P.-E., *Laser-induced incandescence for soot particle size measurements in premixed flat flames.* Applied Optics, **39**:3683-3690, 2000

87. Mewes, B. and Seitzman, J.M., *Analysis of laser-induced incandescence and novel soot measurement approaches.* in *34th Aerospace Sciences Meeting*, Reno, NV: AIAA, 1996

88. Mewes, B. and Seitzman, J.M., *Soot volume fraction and particle size measurements with laser-induced incandescence.* Applied Optics, **36**:709-717, 1997

89. Bryce, D.J., Ladommatos, N., and Zhao, H., *Quantitative investigation of soot distribution by laser-induced incandescence.* Applied Optics, **39**:5012-5022, 2000

90. Vander Wal, R.L., *Calibration and comparison of laser-induced incandescence with cavity ring-down.* Proceedings of the Combustion Institute, **27**:59-67, 1998

91. Vander Wal, R.L. and Ticich, T.M., *Cavity ringdown and laser-induced incandescence measurements of soot.* Applied Optics, **38**:1444-1451, 1999

92. Snelling, D.R., Smallwood, G.J., Gülder, Ö.L., Liu, F., and Bachalo, W.D., *A Calibration-Independent Technique of Measuring Soot by Laser-Induced Incandescence Using Absolute Light Intensity.* in *The Second Joint Meeting of the US Sections of the Combustion Institute*, Oakland, California, 2001

93. Snelling, D.R., Smallwood, G.J., Liu, F., Golder, O.L., and Bachalo, W.D., *A calibration-independent laser-induced incandescence technique for soot measurement by detecting absolute light intensity.* Applied Optics, **44**:6773-6785, 2005

94. Tait, N.P. and Greenhalgh, D.A., *PLIF Imaging of Fuel Fraction in Practical Devices and LII Imaging of Soot.* Berichte der Bunsengesellschaft für Physikalische Chemie, **97**:1619-1625, 1993

95. Vander Wal, R.L., Ticich, T.M., and Stephens, A.B., *Optical and Microscopy Investigations of Soot Structure Alterations by Laser-Induced Incandescence.* Applied Physics B, **67**:115-123, 1998

96. Vander Wal, R.L. and Jensen, K.A., *Laser-induced incandescence: excitation intensity.* Applied Optics, **37**:1607-16, 1998

97. Greenhalgh, D.A., *Reclas - Resonant-Enhanced Cars from C₂ Produced by Laser Ablation of Soot Particles.* Applied Optics, **22**:1128-1130, 1983

98. Eckbreth, A.C., Anderson, T.J., and Dobbs, G.M., *Conditional sampling for fuel and soot in CARS thermometry.* Proceedings of the Combustion Institute, **21**:1747-1754, 1986

99. Hemmerling, B. and Stampanoni-Panariello, A., *Investigation of soot by two-colour four-wave mixing.* Chemosphere, **42**:647-653, 2001

100. Cole, T.C., Cole, W.A., Brown, T.M., and Pitz, R.W., *Measurement of smoke concentration using degenerate four-wave mixing.* Measurement Science & Technology, **13**:464-470, 2002

101. Walewski, J., Rupinski, M., Bladh, H., Li, Z.S., Bengtsson, P.-E., and Aldén, M., *Soot visualisation by use of laser-induced soot vapourisation in combination with polarisation spectroscopy.* Applied Physics B, 77:447-454, 2003

102. Leipertz, A. and Dankers, S., *Characterization of nano-particles using laser-induced incandescence.* Particle & Particle Systems Characterization, **20**:81-93, 2003

103. Johnson, M.P., Hilton, M., Waterman, D.R., and Black, J.D., *Development of techniques to characterize particulates emitted from gas turbine exhausts.* Measurement Science & Technology, **14**:1146-1150, 2003

104. Black, J.D., *Laser Induced Incandescence measurements of particles in aero-engine exhausts.* Proceedings of the 1999 Environmental Sensing and Applications, **3821**:209-215, 1999

105. Schäfer, K., Heland, J., Lister, D.H., Wilson, C.W., Howes, R.J., Falk, R.S., Lindermeir, E., Birk, M., Wagner, G., Haschberger, P., Bernard, M., Legras, O., Wiesen, P., Kurtenbach, R., Brockmann, K.J., Kriesche, V., Hilton, M., Bishop, G., Clarke, R., Workman, J., Caola, M., Geatches, R., Burrows, R., Black, J.D., Herve, P., and Vally, J., *Nonintrusive optical measurements of aircraft engine exhaust emissions and comparison with standard intrusive techniques.* Applied Optics, **39**:441-455, 2000

106. Delhay, J., Bouvier, Y., Therssen, E., Black, J.D., and Desgroux, P., *2D imaging of laser wing effects and of soot sublimation in laser-induced incandescence measurements.* Applied Physics B, **81**:181-186, 2005

107. Geitlinger, H., Streibel, T., Suntz, R., and Bockhorn, H., *Two-dimensional imaging of soot volume fractions, particle number densities and particle radii in*

laminar and turbulent diffusion flames. Proceedings of the Combustion Institute, **27**:1613-1621, 1998

108. Geitlinger, H., Streibel, T., Stuntz, R., and Bockhorn, H., *Statistical analysis of soot volume fractions, particle number densities and particle radii in a turbulent diffusion flame.* Combustion Science and Technology, **149**:115-134, 1999

109. Hentschel, J., Suntz, R., and Bockhorn, H., *Soot formation and oxidation in oscillating methane-air diffusion flames at elevated pressure.* Applied Optics, **44**:6673-6681, 2005

110. Will, S., Schraml, S., and Leipertz, A., *2-Dimensional Soot-Particle Sizing by Time-Resolved Laser-Induced Incandescence.* Optics Letters, **20**:2342-2344, 1995

111. Roth, P. and Filippov, A.V., *In situ ultrafine particle sizing by a combination of pulsed laser heatup and particle thermal emission.* Journal of Aerosol Science, **27**:95-104, 1996

112. Lehre, T., Bockhorn, H., Jungfleisch, B., and Suntz, R., *Development of a measuring technique for simultaneous in situ detection of nanoscaled particle size distributions and gas temperatures.* Chemosphere, **51**:1055-1061, 2003

113. Dankers, S. and Leipertz, A., *Determination of primary particle size distributions from time-resolved laser-induced incandescence measurements.* Applied Optics, **43**:3726-3731, 2004

114. Kock, B.F., Eckhardt, T., and Roth, P., *In-cylinder sizing of diesel particles by time-resolved laser-induced incandescence (TR-LII).* Proceedings of the Combustion Institute, **29**:2775-2782, 2002

115. Bougie, B., Ganippa, L.C., Van Vliet, A.P., Meerts, W.L., Dam, N.J., and Ter Meulen, J.J., *Laser-induced incandescence particle size measurements in a heavy-duty diesel engine.* Combustion and Flame, **145**:635-637, 2006

116. Bougie, B., Ganippa, L.C., Dam, N.J., and ter Meulen, J.J., *On particulate characterisation in a heavy-duty Diesel engine by time-resolved laser-induced incandescence.* Applied Physics B, **83**:477-485, 2006

117. Boiarciuc, A., Foucher, F., and Mounaïm-Rousselle, C., *Soot volume fractions and primary particle size estimate by means of the simultaneous two-color-time-resolved and 2D laser-induced incandescence.* Applied Physics B, **83**:413-421, 2006

118. Snelling, D.R., Liu, F., Smallwood, G.J., and Gülder, Ö.L., *Evaluation of the Nanoscale Heat and Mass Transfer Model of the Laser-Induced*

Incandescence: Prediction of the Excitation Intensity. in *Proc. 34th National Heat Transfer Conf.*, Pittsburg, PA, 2000

119. Will, S., Schraml, S., Bader, K., and Leipertz, A., *Performance Characteristics of Soot Primary Particle Size Measurements by Time-Resolved Laser-Induced Incandescence.* Applied Optics, **37**:5647-5658, 1998

120. Liu, F.S., Smallwood, G.J., and Snelling, D.R., *Effects of primary particle diameter and aggregate size distribution on the temperature of soot particles heated by pulsed lasers.* Journal of Quantitative Spectroscopy & Radiative Transfer, **93**:301-312, 2005

121. Liu, F., Yang, M., Hill, F.A., Snelling, D.R., and Smallwood, G.J., *Influence of polydisperse distributions of both primary particle and aggregate size on soot temperature in low-fluence LII.* Applied Physics B, **83**:383-395, 2006

122. Liu, F.S., Stagg, B.J., Snelling, D.R., and Smallwood, G.J., *Effects of primary soot particle size distribution on the temperature of soot particles heated by a nanosecond pulsed laser in an atmospheric laminar diffusion flame.* International Journal of Heat and Mass Transfer, **49**:777-788, 2006

123. Filippov, A.V. and Rosner, D.E., *Energy transfer between an aerosol particle and gas at high temperature ratios in the Knudsen transition regime.* International Journal of Heat and Mass Transfer, **43**:127-138, 2000

124. Smallwood, G.J., Snelling, D.R., Liu, F., and Gülder, Ö.L., *Clouds over soot evaporation: Errors in modeling laser-induced incandescence of soot.* Journal of Heat Transfer, **123**:814-818, 2001

125. Liu, F., Daun, K.J., Snelling, D.R., and Smallwood, G.J., *Heat conduction from a spherical nano-particle: status of modeling heat conduction in laser-induced incandescence.* Applied Physics B, **83**:355-382, 2006

126. Kuhlmann, S.-A., Reimann, J., and Will, S., *On heat conduction between laser-heated nanoparticles and a surrounding gas.* Journal of Aerosol Science, **37**:1696-1716, 2006

127. Michelsen, H.A., Witze, P.O., Kayes, D., and Hochgreb, S., *Time-resolved laser-induced incandescence of soot: the influence of experimental factors and microphysical mechanisms.* Applied Optics, **42**:5577-5590, 2003

128. De Iuliis, S., Migliorini, F., Cignoli, F., and Zizak, G., *Peak soot temperature in laser-induced incandescence measurements.* Applied Physics B, **83**:397-402, 2006

129. De Iuliis, S., Cignoli, F., and Zizak, G., *Two-color laser-induced incandescence (2C-LII) technique for absolute soot volume fraction measurements in flames.* Applied Optics, **44**:7414-7423, 2005

107

130. Michelsen, H.A., *Laser-induced incandescence of flame-generated soot on a picosecond time scale.* Applied Physics B, **83**:443-448, 2006

131. Lehre, T., Suntz, R., and Bockhorn, H., *Time-resolved two-color LII: size distributions of nano-particles from gas-to-particle synthesis.* Proceedings of the Combustion Institute, **30**:2585-2593, 2005

132. Migliorini, F., De Iuliis, S., Cignoli, F., and Zizak, G., *Absorption correction of two-color laser-induced incandescence signals for soot volume fraction measurements.* Applied Optics, **45**:7706-7711, 2006

133. Kock, B.F. and Roth, P., *Two-color TR-LII applied to in-cylinder Diesel particle sizing.* in *Proceedings of the European Combustion Meeting*, Orléans, 2003

134. Smallwood, G., Snelling, D.R., Sawchuk, R.A., Clavel, D., and Gareau, D., *Design optimization for high-sensitivity two-color LII (Poster).* in *2nd International Workshop on laser-induced incandescence*, Bad-Herrenalb, Germany, 2006

135. Charwath, M., Suntz, R., and Bockhorn, H., *Influence of Temporal Resolution on Time-Resolved Laser-Induced Incandescence Signal Evolutions.* Applied Physics B, **83**:435-442, 2006

136. Kohse-Höinghaus, K., *Laser techniques for the quantitative detection of reactive intermediates in combustion systems.* Progress in Energy and Combustion Science, **20**:203-279, 1994

137. Daily, J.W., *Laser induced fluorescence spectroscopy in flames.* Progress in Energy and Combustion Science, **23**:133-199, 1997

138. Zhao, H. and Ladommatos, N., *Optical diagnostics for in-cylinder mixture formation measurements in IC engines.* Progress in Energy and Combustion Science, **24**:297-336, 1998

139. Andersson, Ö., Collin, R., Aldén, M., and Egnell, R., *Laser-Rayleigh imaging of DME sprays in an optically accessible DI Diesel truck engine.* SAE Technical paper 2001-01-0915, 2001

140. Watson, K.A., Lyons, K.M., Donbar, J.M., and Carter, C.D., *Scalar and velocity field measurements in a lifted CH_4-air diffusion flame.* Combustion and Flame, **117**:257-271, 1999

141. Najm, H.N., Paul, P.H., Mueller, C.J., and Wyckoff, P.S., *On the adequacy of certain experimental observables as measurements of flame burning rate.* Combustion and Flame, **113**:312-332, 1998

142. Schulz, C. and Sick, V., *Tracer-LIF diagnostics: quantitative measurement of fuel concentration, temperature and fuel/air ratio in practical combustion systems.* Progress in Energy and Combustion Science, **31**:75-121, 2005

143. Warnatz, J., Maas, U., and Dibble, R.W., *Combustion: Physical and chemical fundamentals, modelling and simulation, experiments, pollutant formation*, Springer: Berlin, 1996

144. Bäuerle, B., Warnatz, J., and Behrendt, F., *Time-resolved investigation of hot spots in the end gas of an S. I. engine by means of 2-D double-pulse LIF on formaldehyde.* Proceedings of the Combustion Institute, **26**:2619-2626, 1996

145. Brackmann, C., Nygren, J., Bai, X., Li, Z.S., Bladh, H., Axelsson, B., Denbratt, I., Koopmans, L., Bengtsson, P.-E., and Aldén, M., *Laser-induced fluorescence of formaldehyde in combustion using third harmonic Nd:YAG laser excitation.* Spectrochimica Acta Part A, **59**:3347-3356, 2003

146. Bäuerle, B., Hoffmann, F., Behrendt, F., and Warnatz, J., *Detection of hot spots in the end gas of an internal combustion engine using two-dimensional LIF of formaldehyde.* Proceedings of the Combustion Institute, **25**:135-141, 1994

147. Schiessl, R., Dreizler, A., Maas, U., Grant, A.J., and Ewart, P., *Double-pulse PLIF imaging of self-ignition centers in an SI engine.* SAE Technical paper 2001-01-1925, 2001

148. Graf, N., Gronki, J., Schulz, C., Baritaud, T., Cherel, J., Duret, P., and Lavy, J., *In-cylinder combustion visualization in an auto-igniting gasoline engine using fuel tracer- and formaldehyde-LIF imaging.* SAE Technical paper 2001-01-1924, 2001

149. Olofsson, J., Seyfried, H., Richter, M., Aldén, M., Vressner, A., Hultqvist, A., Johansson, B., and Lombaert, K., *High-speed LIF imaging for cycle-resolved formaldehyde visualization in HCCI combustion.* SAE Technical paper 2005-01-0641, 2005

150. Hildingsson, L., Persson, H., Johansson, B., Collin, R., Nygren, J., Richter, M., Aldén, M., Hasegawa, R., and Yanagihara, H., *Optical diagnostics of HCCI and UNIBUS using 2-D PLIF of OH and formaldehyde.* SAE Technical paper 2005-01-0175, 2005

151. Collin, R., Nygren, J., Richter, M., Aldén, M., Hildingsson, L., and Johansson, B., *Simultaneous OH- and formaldehyde-LIF measurements in an HCCI engine.* SAE Technical paper 2003-01-3218, 2003

109

152. Svelto, O. and Hanna, D.C., *Principles of lasers.* 4th ed., Plenum Press: New York, 1998

153. Siegman, A.E., *Lasers*, University Science Books: Mill Valley, CA, 1986

154. Svanberg, S., *Atomic and molecular spectroscopy: Basic aspects and practical applications*, Springer-Verlag: Berlin, 1992

155. Dataray Incorporated, 605 Stapp Road, Boulder Creek, CA 95006, U.S.A.

156. Holthuis & Associates, P.O. Box 1531, Sebastopol, CA 95473, U.S.A.

157. Bowditch, F.W., *A new tool for combustion research - A quartz piston engine.* SAE Transaction, **69**:17-23, 1961

158. Hofeldt, D.L., *Real-time soot concentration measurement technique for engine exhaust streams.* SAE Technical Paper 930079, 1993

159. Köylü, Ü.Ö., Faeth, G.M., Farias, T.L., and Carvalho, M.G., *Fractal and projected structure properties of soot aggregates.* Combustion and Flame, **100**:621-633, 1995

160. Filippov, A.V., Zurita, M., and Rosner, D.E., *Fractal-like aggregates: Relation between morphology and physical properties.* Journal of Colloid and Interface Science, **229**:261-273, 2000

161. Liu, F., Daun, K.J., Beyer, V., Smallwood, G.J., and Greenhalgh, D.A., *Some theoretical considerations in modelling laser-induced incandescence at low-pressures.* Applied Physics B, **87**:179-191, 2007

162. McCoy, B.J. and Cha, C.Y., *Transport Phenomena in Rarefied-Gas Transition Regime.* Chemical Engineering Science, **29**:381-388, 1974

163. Fuchs, N.A., *On the stationary charge distribution on aerosol particles in a bipolar ionic atmosphere.* Pure and Applied Geophysics, **56**:185-193, 1963

164. Snelling, D.R., Liu, F.S., Smallwood, G.J., and Gülder, Ö.L., *Determination of the soot absorption function and thermal accommodation coefficient using low-fluence LII in a laminar coflow ethylene diffusion flame.* Combustion and Flame, **136**:180-190, 2004

165. Dasch, C.J., *Continuous-wave probe laser investigation of laser vaporization of small soot particles in a flame.* Applied Optics, **23**:2209-2215, 1984

166. Kennard, E.H., *Kinetic theory of gases.* 1st ed. International series in physics, McGraw-Hill: New York, 1938

167. Michelsen, H.A., Liu, F., Kock, B.F., Bladh, H., Boiarciuc, A., Charwath, M., Dreier, T., Hadef, R., Hofmann, M., Reimann, J., Will, S., Bengtsson, P.-E., Bockhorn, H., Foucher, F., Geigle, K.P., Mounaïm-Rousselle, C.,

Schulz, C., Stirn, R., Tribalet, B., and Suntz, R., *Modeling Laser-Induced Incandescence of Soot: A summary and comparison of LII models.* Accepted for publication in Applied Physics B, 2007

168. Bockhorn, H., Fetting, F., and Heddrich, A., *Investigation of particle inception in sooting premixed hydrocarbon oxygen low pressure flames.* Proceedings of the Combustion Institute, **21**:1001-1012, 1986

169. Heidermann, T., Jander, H., and Wagner, H.G., *Soot particles in premixed C_2H_4-air-flames at high pressures (P=30-70 bar).* Physical Chemistry Chemical Physics, **1**:3497-3502, 1999

170. Dormand, J.R. and Prince, P.J., *Family of embedded Runge-Kutta formulae.* Journal of Computational and Applied Mathematics, **6**:19-26, 1980

171. Mathworks, *Matlab documentation.* Available at: http://www.mathworks.com, 2006

172. Shampine, L.F. and Reichelt, M.W., *The MATLAB ODE suite.* Siam Journal on Scientific Computing, **18**:1-22, 1997

173. Price, K. and Storn, R., *Differential Evolution (DE) for Continuous Function Optimization for MATLAB (devec3.m).* Available under the GNU general public licence, http://http.icsi.berkeley.edu/~storn, 1996

174. Pinson, J.A., Tuqiang, N., and Litzinger, T.A., *Quantitative imaging study of the effects of intake air temperature on soot evolution in an optically-accessible D.I. Diesel engine.* SAE Technical Paper 942044, 1994

175. Vestin, F., Afzelius, M., Brackmann, C., and Bengtsson, P.-E., *Dual-broadband rotational CARS thermometry in the product gas of hydrocarbon flames.* Proceedings of the Combustion Institute, **30**:1673-1680, 2005

176. Yoder, G.D., Diwakar, P.K., and Hahn, D.W., *Assessment of soot particle vaporization effects during laser-induced incandescence with time-resolved light scattering.* Applied Optics, **44**:4211-4219, 2005

177. Bengtsson, P.-E. and Aldén, M., *Soot Particle Measurements in Premixed Ethylene Flames Using a Pulsed Laser Method.* Journal of Aerosol Science, **19**:959-962, 1988

178. Axelsson, B., Collin, R., and Bengtsson, P.-E., *Laser-induced incandescence for soot particle size and volume fraction measurements using on-line extinction calibration.* Applied Physics B, **72**:367-372, 2001

179. Beyer, V. and Greenhalgh, D.A., *Laser Induced Incandescence under High Vacuum Conditions.* Applied Physics B, **83**:455-467, 2006

180. Schraml, S., Dankers, S., Bader, K., Will, S., and Leipertz, A., *Soot temperature measurements and implications for time-resolved laser-induced incandescence (TIRE-LII).* Combustion and Flame, **120**:439-450, 2000

181. Daun, K.J., Stagg, B.J., Liu, F., Smallwood, G.J., and Snelling, D.R., *Determining aerosol particle size distributions using time-resolved laser-induced incandescence.* Applied Physics B, Available online, DOI:10.1007/s00340-007-2585-y, 2007

182. Chase, M.W., Davies, C.A., Downey, J.R., Frurip, D.J., Mcdonald, R.A., and Syverud, A.N., *Janaf Thermochemical Tables - 3rd Edition.* Journal of Physical and Chemical Reference Data, **14**:927-1856, 1985

183. Fried, L.E. and Howard, W.M., *Explicit Gibbs free energy equation of state applied to the carbon phase diagram.* Physical Review B, **61**:8734-8743, 2000

184. Weast, R.C., ed. *CRC Handbook of chemistry and physics.* Chemical Rubber Company: West Palm Beach, FL, 1978

185. Krishnan, S.S., Lin, K.C., and Faeth, G.M., *Extinction and scattering properties of soot emitted from buoyant turbulent diffusion flames.* Journal of Heat Transfer, **123**:331-339, 2001

186. Leider, H.R., Krikorian, O.H., and Young, D.A., *Thermodynamic properties of carbon up to the critical point.* Carbon, **11**:555-563, 1973

Acknowledgements

I wish to thank the director, the crew and the staff,
and I wish particularly to thank Harry,
and the fine musicians from the London Philharmonic',
without whom…,
it would have been much easier!
I wish to thank my parents for having made this possible,
and I wish to thank my children for having made it necessary.
I wish to thank you for having made it so pleasant,
and I wish to remind you that the smile is the shortest distance between people.
The more we smile the less we fight,
because, to my knowledge, no one ever fought smilingly…,
and won!
So, not good bye then, never good bye!
Just so long!

Victor Borge[1]

This work has been carried out at the Division of Combustion Physics at Lund University, during the years 2001-2007. During such a long period of time numerous and yet numerous people have contributed in different ways to make this work possible and more fun to do.

First of all I would like to thank my supervisor Professor Per-Erik Bengtsson. Per-Erik, you possess great knowledge within several fields, and are able to see good ideas were I predominately see bad ones. You have taught me the fundamentals of science and writing papers. You are also one of the key players responsible for creating a most enjoyable atmosphere at the division. However, with risk of insulting you, I dare say that your greatest ability is to put up with me, my strange ideas and everlasting need to see a Monthy-Python sketch in any moment of everyday life. Totally disregarding the theory of combustion processes outlined in Chapter 2, and indeed also the theory of light interaction with matter outlined in Chapter 3, I truly believe that this ability has *tuned us to the same wavelength* and have contributed with part of the *fuel* needed for this thesis to be realised. Thank you very much for these years!

---

[1] From "*Clockwise Borge*", London Weekend Television, 1972

I also want to thank my co-supervisor, head of division Professor Marcus Aldén. Thank you, Marcus, for your support during this time. I also would like to take this opportunity to acknowledge your great efforts during the years as one of the key players (not football but anyway…) in creating the platform of connections and financing from which we all benefit at the division.

When conducting the flame-front propagation work presented in this thesis, I cooperated with Christian Brackmann. We shared an apartment together in Gothenburg and carried out the measurements at Chalmers University of Technology. Christian, you have taught me many of the things I know about laboratory work. You always took time to explain how things worked and you made sure that I understood. I also admired your ability to keep track of facts. You knew precisely were to search for specific filters and camera lenses at the division, and seemed to be the only one, except maybe Per-Erik and Marcus, that knew the origin of the vast number of old things[2] stored in our basement. Our good cooperation in the lab gradually grew to much more, and today I am proud to call you my friend. You were responsible for taking the photographs at my and Ulrica's wedding in 2005, for which we are both extremely grateful.

I would also like to thank Boman Axelsson and Robert Collin for their support during the early days of my time at the division. You worked with the laser-induced incandescence technique before me, and told me much of the secrets.

Sometimes you need information on something new. Much more efficient than Google™ is to go and ask someone in the next office. I want to thank all of you that have been so helpful discussing various matters with me during the years, especially Joakim Bood, Zhongshan Li, Mattias Richter and Frederik Ossler.

Special thanks goes to my very dear friend and colleague Jimmy Olofsson, who I met the first time as we both started our undergraduate studies in engineering physics in 1995 (or was it 1895…). Our love for music, singing and playing the piano and electric organ[3], actually led to a full concert recital held in one of the lecture halls at the Mathematics department back in 1998. This probably formed the first and last time ever during which the theme from the TV-series "Dallas" was performed live in that hall… Jimmy, I regard you as one of my best friends, and you have been there for me during all these years, not least during the sometimes seemingly endless work carried out when writing this thesis. You have also been one of the most important key players (I seem to keep using these sports terms…) at the division, something everyone may not be aware of. You have been the longest sitting member of "Trivselkommittén" and during this time you have (apart from being *seated*, apparently…) been the silent force behind much of our

---

[2] I fear some would read: "junk"…

[3] There seems to be some confusion with regards to the musical instrument that Jimmy actually plays, and therefore a brief description is given here: He plays Yamaha Electone®, which is an electric organ on which for instance full symphonic music may be played live without pre-recorded parts. The instrument is played pretty much like a church organ with multiple keyboards and foot pedals, while the sounds are generated using advanced synthesizing.

social activities from the day the committee was initiated. Finally, I must say I have enjoyed sharing office with you during my time at the division.

Three great guys I would like to direct a special thanks to are Martin Linvin, Johan Zetterberg and Hans Seyfried. Together with Jimmy and me you are the old school among the current PhD students. I especially remember the great fun we had when attending the course in Combustion Devices some years ago.[4] Martin, you have (admittedly under somewhat different names) been a part of my life as long as Jimmy has, from the time when we all three started our undergraduate studies. You and I cooperated some years ago on measurements in a sooting acetylene diffusion flame, and I realised that you were truly amazing in getting things done. I am also very grateful for all your help when I moved into my previous apartment in 2002. Johan, you are also among those people getting thing done. Additionally, you (as indeed I) have a tendency to overdo things sometimes. I still remember the time when you only had one evening to prepare a PowerPoint presentation for a course, and still managed to give a truly excellent talk using an equally excellent presentation the next day. Afterwards it turned out that all the high-resolved perfectly aligned pictures in you presentation were digitized from a book using a digital camera (as you did not have access to a scanner) meaning hours of extra work with image post processing in order to present the nearly flawless results. Hans, as a true sports fanatic, you are one of the nicest, and you seem to possess endless amounts of positive energy. I did not explicitly write about you in Chapter 1, but I truly believe that if we could find a way of mastering your internal energy we could change the appearance of Fig. 1.1!

One person that actually has been very important to me during the years is Sven-Inge Möller. Sven-Inge, you were very helpful when Jimmy and I started our master's thesis work in 2000, and were totally new to the concept of turbulence. We spent a lot of time in your office trying to understand the underlying mechanisms. As kind as you were, maybe you provided us with a hint when you finally *gave us* your only visiting chair![5] During my PhD years I have deliberately avoided the turbulence subject (a sound decision, as our office could not accommodate yet another chair…) and instead our mutual interest in comics (especially Tin Tin) has dominated, not forgetting our endless discussions regarding "all those small things so important in life".

I would like to direct a special thanks to the administrative and technical staff, Elna Brodin, Marie Persson, Anneli Nilsson, Cecilia Bille and Thomas Wendel. Elna, you are indeed one of the key persons that formed my opinion of the friendly atmosphere at Combustion Physics, an opinion that greatly influenced my choice to apply for a position back in 2001. Marie, I am sorry! I never intended to bring

---

[4] … and on some particular occasions not so much fun at all, like the occasion occurring in a taxi is Stockholm where the driver did not seem to know anything about how to drive in… Stockholm!

[5] For those not familiar with the history of the "retro-style visiting chair with the strange squeaking sound" that has been residing in our office during the last six years, it is worth pointing out that it is that same chair…

you so much work on my travelling expenses. Anneli, in addition to being really good at your work, you are sometimes completely "wacko" and I love it. Keep up that spirit! Cecilia, I have a confession: I have never ever understood anything you tell me about your work when we small-talk. I have, however, tried to compensate this by delivering totally incomprehensible talks on laser-induced incandescence theory on my Tuesday's presentations, during one of which, I recall, you actually burst into laughter! It formed one of these moments were you relax with a smile at your face and think: Indeed, my work here is done! Thomas, you have been a great support for me during the major part of my time at the division with regards to computer problems, electronic problems, discussing problems, problems and yet some… problems! By the way, I am sorry for all these problems. Did I say *problems*? In addition, I have so much enjoyed our ukulele-related discussions, and I encourage you and your "lillbrylling" to release that website![6]

I would like to take the opportunity to once more thank my supervisor Professor Per-Erik Bengtsson, this time for letting me write such a long acknowledgement without charging me for extra pages, and also Jonathan Johnsson, who will continue the work on developing the LII technique in Lund. Finally, I would like to thank all other current and old members of the Combustion Physics division in Lund, both within the laser diagnostic and chemical kinetics group, who all in different ways have contributed to this work and to the enjoyable atmosphere at the division.[7]

The time has come for some outdoor thanks. I would like to start with the nice people at the Department for Applied Mechanics at Chalmers Technical University in Gothenburg, at which Christian Brackmann and I carried out laser-diagnostic measurements in a spark-ignition engine. I would like to thank Professor Ingemar Denbratt and Petter Dahlander for good cooperation both during measurements and paper writing. I also would like to direct a special thanks to Allan Sognell who operated the engine.

The Diesel engine measurements were carried out in cooperation with the Department of Energy Sciences at Lund University. I would like to thank Professor Bengt Johansson, Anders Hultqvist and Leif Hildingsson for good cooperation and of course a special thanks goes to the remarkable Jan-Erik Nilsson who takes care of engine laboratories like no one else. Last but not least I want to thank Volker Gross from University of Karlsruhe, who participated in the laser-diagnostic measurements.

The collaboration with the research group in Lille has been strong during the years of our participation in the European project AEROTEST. I would like to thank Pascale Desgroux, Jérôme Delhay, Yoann Bouvier and Eric Therssen for this time, and especially for making a visiting Swede feel so welcome in France during

---

[6] I deliberately omit describing the underlying concept with risk of Martin beating you to it…

[7] Of course I could name a lot more people but I probably would end up having to mention Andreas Ehn's huge undertaking attempting to consume one half of a "smörgåstårta" and that would not be so nice, would it?

the campaign in November 2004. Pascale, you are truly an extraordinary person performing extraordinary things at your lab, not least within the Aerotest project. I also thank you for the very nice evening we had some time ago in your garden eating from numerous delicious French cheeses, bread and drinking wine. Jérôme and Yoann, thank you for the nice cooperation and also the nice trip to Calais and Cap Gris Nez!

Finally, I would like to acknowledge some people in my personal sphere, people that may not have contributed to the work in itself, but have acted as important catalysts in the process. One of my most dear friends having nothing at all to do with hi-tech gadgets and physics (at least not deliberately, and if forced to, not without a struggle…) is Anna Smedjeback. Anna, you have been a very important person in my life since we were children and have contributed in making my life so much nicer in many ways, not least during the years I have worked on this thesis. I am truly lucky to have such a friend.

Thesis-writing is not a job. It may start out as one, but it slowly yet steadily transforms into a life-style. Indeed, the last three months it fights to become your entire life. I would therefore like to express great gratitude to my beloved wife Ulrica for having endured this time, and encouraged me when I had bad days. Ulrica, thank you for being the most wonderful wife a man can ever have! I would also like to thank my parents Åsa and Stephan and my brother Markus for their great support during the years. Mum and dad, you encouraged me already as a child and let me explore the world in my own way. You have patiently put up with my strange habits during my teenage years, especially when piano playing accounted for a substantial fraction of my daily activities. Markus, we are very different and yet so very much alike. I am very proud to have you as my brother!

Every thesis comes to an end and, amazingly enough, this is it…

Henrik Bladh
Lund 2007

Summary of papers

I.   In the work presented in this paper an extended heat and mass transfer model predicting the signal response of the laser-induced incandescence (LII) technique is used to test and predict the influence of the primary particle size distribution and the spatial distribution of the laser energy on the LII signal. Different polydisperse primary particle size distributions were tested to estimate the bias introduced on evaluated particle sizes from LII measurement data when assuming the distribution to be monodisperse during data evaluation. Also, the signal response from three different spatial profiles of the laser, the top-hat, Gaussian sheet and Gaussian beam were used to determine its influence on the fluence dependence of the LII signal.

I implemented the model, carried out the simulations and wrote the paper together with my co-author.

II.   This paper describes a comparison between experimentally obtained laser-induced incandescence signals from a thin methane diffusion flame and predictions from the same system obtained using the model for LII. Detection was made both spatially resolved using ICCD cameras and temporally resolved using a PMT. The imaging was made using both the conventional 90-degree angle detection and the backward detection. The spatial distribution of laser energy as well as the total power was monitored online. The experimental part of this work was carried out in Lille, France in the group of Pascale Desgroux.

I participated during parts of the measurement series and later made a small part of the data processing. I made the theoretical predictions using the model for LII and was the main responsible for the model and experiment comparisons as well as the manuscript preparation.

III.   In this paper quantitative laser-induced incandescence measurements of soot volume fractions in a high-speed direct-injection passenger car Diesel engine are presented. The measurements were performed using 1064 nm excitation from a Nd:YAG laser and a gated ICCD camera. Quantitative soot volume fractions were attained by comparing the signal levels obtained in the engine with those obtained in a calibration flame with soot volume fractions determined using the extinction technique. In the first

part of the paper the results are used to draw conclusions from an engine perspective mainly from the relative behaviour of the soot levels. In the latter part of the paper the laser-induced incandescence technique together with the calibration scheme are discussed and an investigation of systematic errors introduced due to the difference in gas temperature and pressure in the reference flame and the engine cylinder are estimated using the heat and mass transfer model for laser-induced incandescence.

This work was carried out together with the Combustion Engines Division at Lund Institute of Technology. The laser diagnostic experiments were carried out by me and Volker Gross, whereas the engine was run and monitored by Leif Hildingsson and Anders Hultqvist. I made the major part of the data evaluation, all model results and was the main responsible for writing the paper.

IV.   Most often it is assumed that the LII signal is proportional to the soot volume fraction, an assumption that generally is not true. This paper discusses the relationship between the soot volume fraction and the laser-induced incandescence signal for variations in particle size. The treatment by Melton in 1984 is discussed and tested using a modern heat and mass transfer model for LII. The influence of several parameters like ambient gas temperature and pressure, aggregation, spatial and temporal distribution of laser energy, gate and delay timing etc. is investigated in a parameters study. Based on the results it is possible to choose the experimental conditions in order to minimize the errors introduced due to the particle size effect, and also to compensate for them in cases where the particle sizes are known.

I made the model results, the comparisons and was the main responsible for preparing the manuscript together with the co-authors.

V.   This paper presents an approach of determining the speed of the flame propagation inside the combustion chamber of a spark-ignition engine. The scheme was based on imaging of cool flame species concentration using laser-induced fluorescence (LIF) generated using a set of two Nd:YAG lasers operating at 355 nm and two ICCD cameras. The data processing procedure as well as advantages and limitations of the technique are discussed.

The experimental part of this work was carried out at Chalmers University of Technology. The laser-diagnostic experiments were carried out by me and Christian Brackmann. We also made the data processing and were the main responsible for the manuscript preparation.